PREPARATION OF MONOCRYSTALLINE $CuInSe_2$ AND STUDIES OF Al-Y_2O_3-Si AND Al-Y_2O_3-$CuInSe_2$ STRUCTURES

by

© L. S. Yip

(B. Eng., 1986, McGill University)

A thesis submitted to the Faculty of Graduate Studies
and Research in partial fulfillment of the requirements
for the degree of Master of Engineering

Department of Electrical Engineering
McGill University
Montreal, Canada

June, 1989

ABSTRACT

Preparation of monocrystalline $CuInSe_2$ has been carried out using the vertical Bridgman method in a conventional rf-heated Czochralski crystal-pulling system. Efforts have been made to obtain void- and crack-free crystals large enough for device fabrication and property analysis. X-ray powder diffraction indicated the samples grown in the present were crystals of $CuInSe_2$ with the stable chalcopyrite structure. All as-grown samples were p-type as indicated by hot-point probe. Hall-effect measurements have also been carried out to obtain the mobility, resistivity and carrier concentration of the samples. Mobility values as high as 73 cm^2/V-s were obtained. Electron probe microanalysis has been performed on the samples to examine the chemical composition of the samples. Most of the growth experiments were done with stoichiometric starting compositions. However, bulk $CuInSe_2$ grown from nonstoichiometric starting proportions have also been obtained in order to investigate the properties of $CuInSe_2$ with controlled deviations from stoichiometry. In one case, antimony was also added to a stoichiometric starting composition as a dopant. Experiments on Hall-effect measurements, hot-point probe and electron probe microanalysis were carried out to examine the properties of the nonstoichiometric samples.

Films of Y_2O_3 have also been deposited using rf planar magnetron sputtering on Si and $CuInSe_2$ substrates to form the $Al\text{-}Y_2O_3\text{-}Si$ and $Al\text{-}Y_2O_3\text{-}CuInSe_2$ structures. The dielectric constant of the Y_2O_3 films prepared in the present work was about

12 and the resistivity was about 10^{13} Ω-cm. A small dc leakage was observed for the Al-Y_2O_3-Si capacitors but the Al-Y_2O_3-$CuInSe_2$ capacitors generally exhibited a large dc leakage. The C-V characteristics of these capacitors were measured and the doping profiles of the substrates near the surface were determined. The results obtained for the Al-Y_2O_3-Si capacitors were quite promising, indicating the feasibility of using such an Al-Y_2O_3-semiconductor structure to determine the doping profile of the semiconductor. However, the large dc leakage of the Al-Y_2O_3-$CuInSe_2$ capacitors restricted the accuracy of the C-V measurements and, therefore, the accuracy of the doping profile determinations. Further improvements of the surface preparation of $CuInSe_2$ are then needed to reduce the large dc leakage of the Al-Y_2O_3-$CuInSe_2$ capacitors.

RÉSUMÉ

La préparation du mono-crystal $CuInSe_2$ est réalisée en utilisant la méthode du Bridgman vertical dans un système conventionnel de rf-chauffage Czochralski. Les crystaux sans trous et craques sont obtenus pour la fabrication des exédients et l'analyse. Les échantillous en poudre diffractés du rayon X indiquent la présence des crystaux de $CuInSe_2$ en structure stable de chalcopyrite. Les sondes à point chaud démontrent que tous les échantillons utilisés sont de type p. Les résultats des effets de Hall ont été mesurés pour obtenir la mobilité, la résistivité et la concentration porteuse de tous les échantillons utilisés. Les résultats obtenus pour la mobilité sont aussi élévés que 73 $cm^2/V\text{-}s$. Micro-analyses des sondes électroniques sont utilisées sur les échantillons afin de déterminer leur composition chimique. La plupart des expériences a été effectué avec la composition stoichiométrique. Cependant, les charges $CuInSe_2$ venant des proportions non-stoichiométrique ont été obtenues afin d'étudier les propriétés de $CuInSe_2$ et les déviations controllées par la stoichiométrie. Dans un des cas, l'antimonie a été ajoutée à la composition stoichiométrique comme dopage. Les expériences sur les résultats des effets de Hall, les sondes à point chaud et les micro-analyses des sondes électroniques ont été réalisées afin d'examiner les propriétés des échantillons non-stoichiométriques.

Les pellicules de Y_2O_3 ont été déposées sur les substrats Si et $CuInSe_2$ en utilisant la méthode de "rf magnetron sputtering" pour former les sturctures de $Al\text{-}Y_2O_3\text{-}Si$ et de $Al\text{-}Y_2O_3\text{-}CuInSe_2$.

Le constant diélectrique des couches de Y_2O_3 de cette expérience est environ 12 et la résistivité est de 10^{13} Ω-cm. Une petite fuite du courant direct a été observée durant cette expérience pour les condensateurs Al-Y_2O_3-Si, mais d'autre part, les condensateurs Al-Y_2O_3-Si démontrent une grande fuite du courant direct. Les caractéristiques de ces condensateurs sont mesurés et les profiles de ces substrats prés de la surface sont déterminées. Les résultats assez prometteux obtenus pour Al-Y_2O_3-Si démontrent une possibilité d'utiliser une structure du semiconducteur tel que Al-Y_2O_3 pour déterminer les profiles du dopage du semiconducteur. Cependant, une large fuite dc des condensateurs Al-Y_2O_3-$CuInSe_2$ restreint la précision des mesures de C-V et par conséquent la détermination de la précision des profiles des dopages. Autres améliorations de la surface préparée en $CuInSe_2$ sont aussi nécessaires pour réduire les fuites du courant direct condensateurs des Al-Y_2O_3-$CuInSe_2$.

ACKNOWLEDGEMENTS

The author wishes to express his sincere gratitude to his supervisor, Dr. I. Shih, for his guidance and assistance throughout this study. Thanks also extended to Dr. C. H. Champness for his supervision on the crystal growth of $CuInSe_2$.

Thanks are also due to Mr. W. S. Weng for his collaboration in the work on the crystal growth of $CuInSe_2$. The author is also indebted to Miss C.X. Qiu for her help in experiments on the deposition of Y_2O_3 films, Mr. G. Rhodrigue for his help in setting up the equipments and keeping them in perfect conditions, Mr. Y. F. Go for his advice on the use of the computer softwares for the preparation of this thesis, Mr. A. Chung for translating the abstract into French.

Acknowledgements are also due to The Natural Sciences and Engineering Research Council of Canada for the financial support.

It is hard for the author to adequately express his gratitude to his parents, brothers and sisters for their love, encouragement and support throughout his life.

TABLE OF CONTENTS

CHAPTER ONE

INTRODUCTION

The Cu-III-VI_2 family has attracted considerable attention since the first investigation of the compounds by Hahn et al. [1.1]. The members of this family, especially $CuInSe_2$, have evolved to be the leading candidates in a variety of opto-electronic applications. Solar cells with a conversion efficiency exceeding 10% have already been reported using thin film [1.2] and monocrystalline [1.3, 1.4] $CuInSe_2$ as the absorbing materials. Recently, Mitchell [1.5] has even achieved a conversion efficiency of 14.1 % with a $CuInSe_2$-based cell. At the present, although the $CuInSe_2$-based cells appear to have lower efficiencies than the well-developed solar cells, e.g. monocrystalline silicon solar cells, the potential of $CuInSe_2$ in photovoltaic applications, particularly in terrestrial applications, is very promising because of its exceptional properties. First of all, $CuInSe_2$ has a direct energy gap of about 1 eV, which is in the range of special interest for solar cell applications. Another outstanding property of $CuInSe_2$ is the remarkably high optical absorption coefficient (about $4x10^5$ /cm [1.6, 1.7]), which is the highest among semiconductors and makes $CuInSe_2$ an excellent absorbing material in solar cells. It has also been reported that $CuInSe_2$ can readily be prepared in thin-film form using variety techniques such as the two-source deposition method [1.8], three-source deposition method [1.9] and electro-deposition method [1.10]. The extraordinary high optical absorption coefficient and the ease of the preparation of $CuInSe_2$ in thin-film form enable the use of thin film $CuInSe_2$ with minimal thickness as the absorbing layer in solar cells. (A layer of $CuInSe_2$ film with a thickness of 0.1 μm can absorb as much sunlight as monocrystalline Si can absorb in 50 μm [11].) This would greatly reduce the material cost, which is the major obstacle for terrestrial application of monocrystalline Si solar cells, and enhance the potential of $CuInSe_2$ for terrestrial photovoltaic applications. Another important factor that makes $CuInSe_2$ attractive for terrestrial solar cell application is the lifetime stability of the $CuInSe_2$-based devices. Furthermore, $CuInSe_2$ was also reported to be radiation-hard; solar cells made of $CuInSe_2$ were demonstrated to exhibit stable performance under intense radiation environment without appreciable degradation [1.12]. This property enables $CuInSe_2$ to be used even in extraterrestrial environments.

To further explore the potentials and limitations of $CuInSe_2$ in photovoltaic applications, monocrystals of the compound are required. Furthermore, some properties of $CuInSe_2$ are yet to be well understood. It is, therefore, clear that single crystals of $CuInSe_2$ are needed for these purposes. However, work on preparation of monocrystalline has not been extensively done, mainly due to the difficulty in obtaining large and high quality single crystals of $CuInSe_2$ [1.13]. One of the objectives of the present studies is to prepare large and good quality monocrystals of $CuInSe_2$ for device fabrication and property analyses in our labo ratory. Experiments on the preparation of nonstoichiometric bulk

$CuInSe_2$ have also been carried out in order to investigate the properties of $CuInSe_2$ with controlled deviations from stoichiometry, which have been little studied. It is hoped that the results from these experiments would provide an insight of how the properties of $CuInSe_2$ can be further improved.

The MOS structure has been the heart of the present day computer and VLSI technologies since the development of the sili con planar process. Besides the success in a variety of electronic applications, the MOS structure is also a widely-used analytical tool for the studies of the surface properties of Si, the SiO_2-Si interfacial properties and the oxide properties. Various techniques [1.14] have been developed for these studies. Theoretically, these techniques are equally applicable to the studies of other semiconductors in the metal-insulator-semiconductor (MIS) structure. However, little work has been reported on the studies of the MIS structure on semiconductors other than silicon. The main reason for this is the difficulty in forming a high quality insulating film on the semiconductors, while the thermally-grown SiO_2 on Si has been considered as a gift of the nature. In the present work Y_2O_3 films, which were reported to have good dielectric properties [1.15, 1.16], have also been deposited by rf planar magnetron sputtering. The purposes of this work were to study the properties of the sputtered Y_2O_3 films and investigate the feasibility of the studies of the metal-Y_2O_3(insulator)-semiconductor structure using Si and $CuInSe_2$ substrates.

One of the most important analytical tools in studying MIS system is the C-V technique [1.17]. It can provide information such as doping profile, interface states density, oxide charge and oxide thickness. Therefore, the C-V technique has long been used to monitor the fabrication process of MOS integrated circuits. In the present studies, the C-V characteristics of the metal-Y_2O_3-Si and the metal-Y_2O_3-$CuInSe_2$ structures were measured and the doping profiles of the semiconductors near the insulator-semiconductor interface were determined. If the doping profile can be determined accurately, studies on the thermal stability or the annealing effect can then be made on $CuInSe_2$ according to the redistribution of the doping centers.

The outline of the thesis is the following. Chapter two will describe the preparation of bulk $CuInSe_2$ using the Bridgman method and the characterization of the $CuInSe_2$ crystals. The deposition by rf planar magnetron sputtering and characterization of Y_2O_3 films will be given in chapter three. Using rf sputtered Y_2O_3 films, MIS structures on Si and $CuInSe_2$ substrates have been fabricated; the C-V characteristics were measured and the doping profiles were determined. The work on the C-V measurements will be presented in chapter 4. Finally, conclusions of the present studies will be given in chapter 5.

CHAPTER 2

CRYSTAL GROWTH OF COPPER INDIUM DISELENIDE USING THE VERTICAL BRIDGMAN METHOD

2.1 INTRODUCTION

Copper indium diselenide ($CuInSe_2$) is a ternary compound semiconductor with a chalcopyrite structure. As mentioned in chapter one, the compound is a leading candidate in thin-film solar cell applications. Large and good quality single crystals of $CuInSe_2$ are then needed to explore further its properties and applications.

Most of the work reported on the preparation of $CuInSe_2$ monocrystals employed the Bridgman method [2.1-2.3], directional-freezing method [2.4-2.6] or zone-melting method [2.7,2.8]. Growth experiments using the iodine transport method [2.9], hydrothermal method [2.10] and open-crucible liquid-encapsulated Czochralski method [2.11] have also been reported. Crystal grains from millimeter to centimeter dimensions could be selected from these ingots and microcracks were frequently found on these crystal grains. In the present work, growth experiments of $CuInSe_2$ have been carried out using an rf-heated system in order to obtain large and good quality single crystals of $CuInSe_2$ for property analysis and device fabrication.

Although bulk single crystals of $CuInSe_2$ have been prepared from stoichiometric starting compositions by several workers, it is noted that preparation and studies of bulk $CuInSe_2$ with nonstoichiometric starting compositions has been little reported. In order to explore the properties of $CuInSe_2$ with deviation from stoichiometry, a series of experiments was carried out with nonstoichiometric starting compositions. Furthermore, extrinsic doping of $CuInSe_2$ was not studied extensively. While bismuth appears to act as a donor in $CuInSe_2$ [2.12], Shing et al. [2.13] reported the acceptor extrinsic doping of $CuInSe_2$ with phosphorous, by diffusion. Extrinsic doping by ion implantation with Br, Cl and Zn into p-type $CuInSe_2$ to form pn junctions has also been investigated by Yu et al. [2.14]. In the present studies, bulk $CuInSe_2$ was also prepared with a stoichiometric composition plus Sb as a dopant.

The growth experiments were carried out in a conventional rf-heated Czochralski crystal pulling system, which was adapted for the growth of $CuInSe_2$ using the vertical Bridgman method. The system provided a good driving mechanism and a stable temperature control for the growth experiments. The heating was provided by rf induction through a graphite susceptor. With minor modifications, the system was conveniently employed for the present work.

In this chapter, the Bridgman method will be briefly described in section 2.2. The experimental set-up and the experimental procedure will be described in section 2.3 and 2.4 respectively. Section 2.5 will present the results of the growth experiments with stoichiometric starting proportions. Crystal growth with nonstoichiometric starting proportions will be reported in section 2.6.

2.2 THE GROWTH METHOD

The vertical Bridgman method has been employed for the preparation of $CuInSe_2$ crystals in the present work. In the Bridgman method, the material to be grown is usually contained in an ampoule or a crucible. The ampoule is passed through a stable temperature gradient, which varies from temperature above to temperature below the melting point of the material. The ampoule is usually kept at the high temperature zone long enough to melt all the material and to allow the mixing of the melt by rotating the ampoule before being passed through the temperature gradient. Nucleations takes place at the solid-liquid interface while the melt is being lowered through the temperature gradient. In some cases closed ampoule are required, especially for the growth of material which is volatile or contains a volatile component. Since Se has a very high vapour pressure, it is apparent that closed ampoules should be used for the growth of $CuInSe_2$.

In order to grow large and good quality single crystals, a stable and appropriate temperature gradient is required to maintain a stable solid-liquid interface. A large temperature gradient is usually required in crystal growth; otherwise, constitutional supercooling [2.15] will cause polycrystallinity in the crystals. Besides a large temperature gradient, a slow growth rate is also necessary to avoid this effect [2.16]. As reported by Vahid Shahidi [2.17], a temperature gradient of about 40 ^{o}C/cm is considered to be large enough for the growth of $CuInSe_2$ at a rate of about 1 cm/hr. In the present work, the temperature gradient is about 30-40 $^{o}C/cm$ and the growth rate is a few mm per hour. With these conditions, constitutional supercooling would be avoided.

2.3 THE GROWTH SYSTEM

Since stable and appropriate growing conditions are essential for the growth of good quality crystals, a reliable growth system is needed to provide such conditions. In the present work, a conventional rf-heated Czochralski crystal-pulling system has been adapted for this purpose. A photograph and a schematic of this system are shown in Fig. 2.1 and Fig. 2.2 respectively. The system contained several components. One of them was a Lepel 5 kW 450 kHz induction unit model T-5-3-KC-SW, which was used to generate and supply rf power to a water-cooled work coil.

Another component was a Lepel HCP-C crystal puller, which consisted of a growth chamber and a crystal-pulling mechanism. Fig. 2.3 shows a photograph of the growth chamber and its schematic is illustrated in Fig. 2.4. The arrangement of the growth chamber was modified to suit the Bridgman method. A quartz tube with an outer diameter of 95 mm, a thickness of 2.5 mm and a length of 560 mm defined the volume of the chamber. A graphite susceptor (32 mm i.d., 40 mm o.d. and 180 mm long) inside the growth chamber was heated by rf induction through the water-cooled work coil. The graphite susceptor was supported by a stainless steel support, which in turn was fixed in position by an aluminum block. The graphite susceptor was enclosed by another quartz tube, which was also seated on the aluminum block. Powdered alumina was put between this quartz tube and the graphite susceptor to minimize heat loss through the outer surface of the graphite susceptor. The aluminum block was rested on a stainless steel crucible plate, which was fixed at the top of the crucible support. A type-K thermocouple was passed through the bottom plate and the stainless steel supports to the inside of the graphite susceptor to measure the temperature. Since the temperature would be raised beyond 1000 ^{o}C (the melting point of $CuInSe_2$ is 986 ^{o}C) during the growth, the growth chamber was evacuated and refilled with nitrogen gas to prevent oxidation of the graphite susceptor. Furthermore, water was also passed through the top plate for cooling. The pulling mechanism was equipped with a pull rod and two motors, which provided the vertical motion and rotation. The pull rod, 105 cm long, was passed through the top plate via a special O-ring seal. The ampoule was suspended by a chuck, which was attached to the end of the pull rod. The pull rod was driven by the two motors, one provided vertical motion between 0.8 and 34 mm/hr and the other one rotation between 2 to 40 rpm.

The output power of the rf generator was controlled by a C.A.T. (current adjusted type) temperature controller and a A.Z.A.R. (Adjustable-Zero-Adjustable-Range) unit. The C.A.T. unit controlled the current output to the rf generator and it could be operated in either manual or automatic mode. In automatic mode the output of the C.A.T. unit was controlled by the voltage different between the thermocouple and a set point in the A.Z.A.R. unit. In this case the temperature could be maintained at the set point of the A.Z.A.R. unit within ±0.5 ^{o}C. An external programmable circuit was also employed for the automatic increase and decrease of the temperature, by varying the current output to the rf generator, at the beginning and the end of the growth experiments. This external circuit was capable of raising and lowering the temperature at a rate between 4 and 100 ^{o}C/hr. After a desirable temperature was reached, the rf power was then controlled by the temperature controller to maintain the temperature at the set point.

It was pointed out in section 2.2 that an appropriate temperature gradient is a very important factor in successful crystal growth. The temperature profile in the present system is shown in Fig. 2.5. In this figure, the temperature is plotted against the distance from the top of the graphite susceptor. It was measured by a type-K thermocouple, which was placed inside the graphite susceptor at different heights during the measurement.

2.4 THE EXPERIMENTAL PROCEDURE

2.4.1 Ampoule Preparation

Quartz tubes with an i.d. of 10 mm and an o.d. of 13 mm were used to prepare ampoules for the growth. The procedure of making an ampoule was the following. A clean quartz tube was first sealed at one end by a H_2/O_2 torch. The end was formed into a conical shape to facilitate the nucleation of the material at this end at the beginning of the growth experiment. The quartz tube was then narrowed at about 8-10 cm from the sealed end. This narrowing process was very important because it helped to seal off the ampoule at this narrowed region more quickly and easily. After the narrowing process the ampoule was flame-polished first in air for about ten minutes and then for another ten minutes while the ampoule was being evacuated through the open end. During the flame polishing, most of the impurities would be burnt and pumped away at such a high temperature (>1000 °C). After the flame polishing, the quartz tube continued to be evacuated until it cooled down. The starting materials were then quickly introduced into the quartz tube. High-purity Cu, In, and Se (all 99.999% pure) were used as the starting materials in a weighed stoichiometric ratio for $CuInSe_2$ (i.e., Cu:In:Se: = 1:1:2), with a total weight of 12 grams. In experiments on nonstoichiometric growth of $CuInSe_2$ different ratios, however, were used. Indium was introduced into the quartz tube first and then selenium followed by copper. Since In has the lowest melting point and Se the next, this arrangement avoids the excess heat during sealing off the quartz to melt the In and Se. Then, the charged ampoule was evacuated until the pressure reached $5x10^{-5}$ torr. After this, the quartz tube was sealed off at the narrowed neck. The materials were now sealed under a very low pressure inside the ampoule. This newly sealed end was then joined to a quartz rod for suspension.

2.4.2 Crystal Growth

A growth experiment was divided into two stages. The first stage was the reaction stage, in which the elements were allowed to react to form $CuInSe_2$. The second stage was the actual growth of the $CuInSe_2$ formed in the reaction stage. A typical growth run is described in the following paragraphs.

(i) The Reaction Stage

A growth experiment started by bring the ampoule inside the graphite susceptor to a position where the starting materials were in the zone with the highest temperature. The stoichiometric mixture was heated quickly to 200 ^{o}C and kept at this temperature for at least 4 hours to allow the elements to react slowly. The reaction of the elements started at about the melting point of In (156 ^{o}C). The temperature was then increased slowly at a rate of 20 $^{o}C/hr$ until 450 ^{o}C was reached to avoid excessive reaction to take place. At this stage, the materials were believed to have reacted almost completely.

(ii) The Growth Stage

After the reaction stage, the heating rate was then increased to 60-80 $^{o}C/hr$ until the highest temperature zone reached about 1100 ^{o}C, which exceeds the melting point of $CuInSe_2$ (986 ^{o}C). The ampoule was maintained at this temperature for at least two hours, and at the same time, the ampoule was rotated using a method called the accelerated crucible rotation technique (ACRT) [2.18]. This rotation technique is usually employed for crystal pulling and has been proven to be very useful for mixing of the melt. The idea of the ACRT is that the crucible or ampoule is rotated with acceleration and deceleration alternately and, as a result, a stirring effect is created inside the melt. The maximum rotation speed used in the present work was 40 rpm, and the minimum speed was 20 rpm. The acceleration and deceleration times were both 4 s, which gave an acceleration and deceleration rate of 5 rpm/s. A plot of the rotation speed against time for the ACRT is depicted in Fig. 2.6. After two hours of mixing, the ampoule was then lowered at a speed of 1-2 mm/hr for a distance of about 50 mm. The ampoule was also rotated with the ACRT during the growth. After the descent of the ampoule, the temperature of the graphite susceptor was decreased very slowly, at about 4-30 $^{\circ}$C/hr initially. After the temperature of the $CuInSe_2$ had reached the low phase-transition temperature (665 $^{\circ}$C) [2.19], the cooling rate was increased to 60-80 $^{\circ}$C/hr until the $CuInSe_2$ reached room temperature. Fig. 2.7 shows a photograph of an ingot inside an ampoule after a growth experiment.

2.5 EXPERIMENTAL RESULTS

Using the experimental procedure (with minor variations occasionally) described in the last section, bulk monocrystalline $CuInSe_2$ with stoichiometric starting compositions has been prepared. Several problems emerged at the early stage of the growth experiments and they will be discussed in this section. Some experimental results on the characterization of the $CuInSe_2$ single crystals will also be presented.

2.5.1 Difficulties Encountered and Their Solutions

(i) Condensation of Se

In the present work, the system used was a Czochralski crystal-pulling system which was modified to adapt the Bridgman method as described in section 4.3. The furnace was a graphite susceptor which was heated by rf induction. Limited by the length of the growth chamber, the graphite susceptor could not be too long and the ampoule should be short enough to fit inside the susceptor; otherwise, the top part of the ampoule would project outside the graphite susceptor and Se vapour would condense in this cool region. This condensation problem was observed for the first few runs of the crystal growth experiments. The condensation problem was eliminated by making shorter ampoules (less than 90 mm), but another problem was then encountered. Explosion and cracking of the ampoules occurred occasionally after shorter ampoules had been used. The reduction in volume increased the pressure inside the ampoule and the excessive pressure probably caused the explosion and cracking. However, this breakage problem could be avoided as described in the next section.

(ii) Breakage of Ampoules

Breakage of ampoules or even explosions were observed occasionally in the early stage of the present work especially when shorter ampoules were used. The breakage of an ampoule was due to the excessive heat produced by the reaction of the elements during the reaction stage of the growth experiments. The excessive heat produced would in turn vaporize the volatile Se or greatly increase the Se vapour pressure. The chemical reaction of the elements starts at about the melting point of In (156 ^{o}C) and becomes vigorous after Se melts (217 ^{o}C). Therefore, it is important to allow most of the reaction to take place before raising the temperature beyond the melting point of Se. One way to avoid excessive reaction to take place was to allow the elements to react at a temperature below the melting point of Se for a long period of time. Another way was to employ a slow heating rate to raise the temperature beyond the melting point of Se. The breakage problem could also be avoided by using ampoules with thicker wall, which can withstand higher pressure. Care should also be taken during the ampoule preparation to avoid any "weak points", such as area with particular thin wall which might appear at the sealed ends, on the ampoule. After employing these precautions, ampoule breakage was essentially prevented.

(iii) Adhesion of the Material to the Ampoule

Adhesion of the ingots to the ampoule wall was frequently observed. Although the adhesion has been reduced by the flame polishing described in section 2.4.1, this problem was not practically eliminated. For the sample in which the adhesion problem was particularly severe, cracks were apparent. Fortunately, for most of the samples the adhesion problem was not serious. Usually only a small part of the ingot adhered to the ampoule and the consequence of the adhesion was not drastic.

(iv) Voids and Cracks

In the early part of the growth experiments, the ACRT was not used and only uniform rotation was employed for mixing of the melt. Bulk and surface voids were observed in most of the ingots grown in these experiments. A photograph of polycrystalline samples with voids is shown in Fig. 2.8. Because narrow ampoules have usually been employed for the Bridgman method, mixing has long been a problem, especially for materials that contain high vapour-pressure constituents such as Se. The nucleation of bubbles of these high vapour-pressure constituents can give rise to voids in the ingots.

After the ACRT had been introduced into the growth procedure, ingots without voids were grown. Owing to the periodic accelerated and decelerated rotation of the ACRT, a stirring effect was present in the melt. This stirring effect promised a better mixing of the melt with a homogeneous distribution of the composition. This increase of homogeneity should reduce the number of nucleation centers and large single crystals could then be grown. The nucleation of bubbles , which could give rise to voids, could also be avoided in this case. Crystal grains with an area up to 50 mm^2 and a thickness of more than 5 mm were obtained. Photographs of three single crystal samples cut from ingots grown using the ACRT are shown in Fig. 2.9. By visual inspection, no voids or cracks can be seen on these samples except one small crack on the sample shown in Fig. 2.9 (a).

The conditions used in four typical growth experiments are shown in Table 2.1. From the table, it can be seen that the sample CIS8224, obtained without employing the ACRT, had voids and cracks. It can also be seen from sample CIS8412 that the cooling rate after the growth cannot be too high; otherwise, cracks are induced owing to the fast contraction of the material. The lowering rate of the ampoule does not seem to be very critical as long as the rate is not too fast. Therefore, by employing the ACRT and a slow cooling rate, one can obtain void- and crack-free crystal grains. The good quality crystals were then polished mechanically by 0.3-0.5 μm alumina powder for property analysis and device fabrication.

2.5.2 X-ray Diffraction

Two samples were selected arbitrarily and ground to very fine powder for examination by X-ray powder method. The experiments were carried out in a Siemens model D500 diffractometer system. The powder diffraction patterns of the two samples were almost identical and one of them is shown in Fig. 2.10. Fig. 2.11 depicts the position (2θ) and relative intensity of the peaks calculated from the ASTM data for $CuInSe_2$ with the chalcopyrite structure. It can be clearly seen that the two patterns match closely indicating the samples prepared in the present work were crystals of $CuInSe_2$ with the stable chalcopyrite phase.

2.5.3 Chemical Etching

Chemical etching experiments were carried out using a mixture of H_2SO_4 and $K_2Cr_2O_7$ (9:1 by weight) as the etchant. The samples were etched in the solution for ten minutes at 25 ^oC. Any "weak" points on the crystals would be revealed after the chemical etching; therefore, it helped to examine the quality of the crystals. A photograph of a sample revealing microcracks after being chemically etched is shown in Fig. 2.12. In selecting samples for electrical-property measurements, samples with microcracks were avoided. Grain boundaries were also observed in some samples after etching, a grain boundary can be clearly seen in the sample shown in Fig. 2.13. Etch pits were also observed in a samples as illustrated in Fig. 2.14. The triangular etch pits indicated crystal orientation of three-fold symmetry and this is usually the (111) direction in cubic lattices. However, in the chalcopyrite structure, which is tetragonal in nature, of $CuInSe_2$ this is probably the (112) direction. Since this sample was cut perpendicularly to growth direction, this might be an indication of the orientation of the growth plane. Although Vahid Shahidi [2.17] indicated that no preferred growth orientation was found, Parkes et al. [2.7] demonstrated that the growth plane of their ingots was indeed the (112) plane. Further work has to be done to confirm the orientation of the growth plane.

2.5.4 Hot-point Probe

The conductivity type of the samples was examined by hot-point probe and the results are shown in Table 2.2 for four samples. A very fine probe was used in order to detect any localized regions with different conductivity type from the bulk. All as-grown crystals were uniformly p-type as measured by hot-point probe, this result was in agreement with the result obtained in earlier work in our laboratory [2.12]. However, the as-grown crystals prepared by several workers [2.20, 2.21] were reported to be n-type. This contradiction may be due to the loss of a significant amount of the volatile Se during the crystal growth in their experiments. $CuInSe_2$ crystals with a deficiency of Se were reported to be n-type [2.12].

2.5.5 Hall-effect Measurements

Room temperature Hall effect measurements were also carried out to obtain the mobility, resistivity, and carrier concentration in the crystals. The van der Pauw method was employed for the Hall effect measurements to facilitate the measurements of samples with irregular shape. Results from the Hall effect measurements also confirmed that the crystals grown from stoichiometric starting compositions were p-type. The mobility, the hole concentration and resistivity are also shown in Table 2.2 for four typical samples. It is noted that the mobility values of these samples are larger than the values obtained by other workers [2.4, 2.22].

2.5.6 Electron Probe Microanalysis

Electron probe microanalysis was carried out in order to measure the actual chemical compositions of the ingots. The measured compositions of four samples are shown in Table 2.3. As can be seen from the table, the samples showed higher concentrations of In and Cu than the stoichiometric starting compositions; however, a deficiency of Se was observed. The In/Cu ratio was calculated for each sample and it is found that an In/Cu ratio close to 1 was generally obtained. Compositional uniformity was checked across the growth plane and the result is plotted in Fig. 2.15 for a sample. It can be seen that the compositions are uniform across the sample indicating no segregation of a particular element in the growth plane.

2.6 CRYSTAL GROWTH WITH DEVIATIONS FROM STOICHIOMETRY

Crystal growth of $CuInSe_2$ with nonstoichiometric starting proportions were also performed. The objective of this series of experiments was to study the crystal properties with controlled deviation from the stoichiometry. By considering $CuInSe_2$ as a pseudo-binary alloy of Cu_2Se and In_2Se_3, growth experiments with five different starting compositions were carried out. The five compositions were $(Cu_2Se)_{0.48}(In_2Se_3)_{0.52}$, $(Cu_2Se)_{0.46}(In_2Se_3)_{0.54}$, $(Cu_2Se)_{0.44}(In_2Se_3)_{0.56}$, $(Cu_2Se)_{0.42}(In_2Se_3)_{0.58}$, and $CuInSe_2$ + 1 wt.% Sb. In the last case, antimony was added to the stoichiometric sample as an dopant.

2.6.1 Hot-point Probe

The conductivity type measured by hot-point probe of several samples are shown in Table 2.4. The samples with 48% and 44% of Cu_2Se showed n-type conduction. On the other hand, the samples with 42% and 46 % of Cu_2Se were p-type. The Sb-doped sample was n-type indicating the extrinsic doping of $CuInSe_2$ with Sb changed the conduction type of $CuInSe_2$ from p to n. It was found that localized regions with different conduction type were not found in these nonstoichiometric samples.

2.6.2 Hall-effect Measurements

Hall effect measurements were also carried out on these nonstoichiometric samples. The conductivity type of the samples was also confirmed by the Hall effect measurements. The Hall mobility, resistivity and carrier concentration are also shown in Table 2.4. The mobility values of the n-type samples were relatively small when compared to earlier work in our laboratory [2.17]. The small mobility might be due to some defects in the crystals. Preliminary results of annealing the samples in evacuated ampoules at 500 °C showed little improvement in the mobility of the samples.

2.6.3 Electron Probe Microanalysis

The chemical compositions of the four samples with 42% to 48% of Cu_2Se were determined by electron probe microanalysis and the results are shown in Table 2.5. The determined compositions of the four samples are plotted in the phase diagram in Fig. 2.16. The area enclosed by the dotted line is the compositional range in which highly efficient thin-film solar cells have been reported [2.23]. This implies that films with compositions inside this area are p-type. On the other hand, two bulk samples prepared in the present work with compositions within this range, as can be seen in Fig. 2.16, showed n-type conduction. This difference in conductivity type may be due to the high density of defects, which act as acceptor centers, in thin film $CuInSe_2$. It can be easily seen that the four samples were apparently richer in copper and poorer in Se than the starting compositions, which implies that regions with a deficiency of copper and/or an excess of Se should exist in the ingots. In order to confirm this, the compositions were measured along and across the growth direction. It was found that compositions were uniform across the cross-section of the ingots as shown in Fig. 2.17 for one of the samples (CIS9104). In Fig. 2.18 a plot of the compositions against the distance from the top (the last zone to crystallize) along the sample CIS81219 is shown. It can be seen that the compositions were uniform along the growth direction except the last freeze-out region, in which a deficiency of copper and an excess of Se were found. The top regions of two other samples also showed a deficiency of copper and an excess of Se as shown in Table 2.5. Since higher concentration of copper and lower concentration of Se were incorporated into the crystal during crystallization, the melt then contained less copper and more Se in progress of the growth. Therefore, it is not surprising to find that the end regions of the samples were deficient in copper and in excess of Se.

It was found that the antimony-doped sample contained some small regions with a very high Sb concentration; however, a low Sb concentration was found in the rest of the samples. Table 2.6 shows the measured compositions of three regions with different concentrations of Sb. From this result, it is clear that some of the Sb segregated into certain regions instead of incorporation into the ingot. Nevertheless, only a few of these regions were found. It is thus clear that care should be taken when dopants are added to the starting materials for the growth of $CuInSe_2$ crystals, especially for Sb.

2.7 CONCLUSIONS

Experiments on the growth of $CuInSe_2$ crystals by the vertical Bridgman method have been carried out in the present studies. A conventional rf-heated Czochralski crystal-pulling system was modified for this purpose. Elements of Cu, In and Se were weighed to stoichiometric ratio as the starting materials for the growth experiments. The elements were sealed under a pressure of $5x10^{-5}$ torr inside a quartz ampoule. A slow heating rate during the reaction stage were found to be essential in preventing breakage of ampoules. Furthermore, employing thicker ampoules would further increase the safety against breakage of ampoules. In the early part of the work, voids were frequently found in the ingots because of poor mixing. After the ACRT had been employed, ingots without bulk voids were grown. A slow cooling rate was also observed to be necessary to avoid cracks in the ingots. Large single-crystal grains could usually be selected from the ingots. Several properties of the $CuInSe_2$ have been investigated. X-ray diffraction results suggested that the $CuInSe_2$ crystals obtained had a stable chalcopyrite structure. All as-grown $CuInSe_2$ crystals were found to be p-type. The largest room temperature Hall mobility value obtained was 73 $cm^2/V\text{-}s$. Electron probe microanalysis was also carried out and the results showed that the crystals had an In/Cu ratio very close to 1 but a deficiency of Se was apparent.

Studies were also made on the preparation of nonstoichiometric bulk $CuInSe_2$. A series of experiments was carried out by taking $CuInSe_2$ as a pseudo-binary alloy of Cu_2Se and In_2Se_3 with the formula $(Cu_2Se)_x(In_2Se_3)_{1-x}$. The following compositions have been prepared, x=0.42, 0.44, 0.46 and 0.48. Electron microprobe analysis indicated that the crystals grown in this series of experiments were richer in copper and poorer in Se than the starting compositions; however, a deficiency of copper and an excess of Se was detected in the top regions of the samples. On the other hand, compositional uniformity was observed across the cross-section of the ingots. The conductivity type of the samples was dependent on the deviation from stoichiometry. The samples with 42% and 46% of Cu_2Se were p-type, while the samples with 44% and 48% of Cu_2Se were n-type. An Sb-doped sample revealed a few regions with high Sb concentration indicating the segregation of Sb. However, the Sb concentration in the rest of the sample was low.

Table 2.1 Growth Conditions for Four Samples

Sample no.	Rotation speed (rpm)		Growth rate (mm/hr)	Cooling rate ($^{\circ}C/hr$)	Remarks
	for mixing	during growth			
CIS8224	10	none	2.45	16	Voids and cracks in ingot
CIS8412	20-40*	20-40*	2	20	Few cracks in void-free grains
CIS8428	20-40*	20-40*	2.1	10	Void- and crack-free grains
CIS8503	20-40*	20-40*	2	4.5	Void- and crack-free grains

* ACRT

Table 2.2 Room-Temperature Hall Effect Results

Sample no.	Conduction Type	Mobility (cm^2/V-s)	Carrier Conc. (cm^{-3})	Resistivity (Ω-cm)
CIS8412	p	44.3	1.2×10^{17}	1.1
CIS8428	p	73.0	4.5×10^{16}	1.9
CIS8503	p	49.6	1.0×10^{17}	1.2
CIS8826	p	54.2	6.2×10^{16}	1.9

Table 2.3 Measured compositions of four samples grown from stoichiometric starting proportions

Sample no.	Measured composition (at.%)			In/Cu ratio
	Cu	In	Se	
CIS8328	25.7	26.2	48.1	1.02
CIS8503	26.2	25.6	48.2	0.98
CIS8412	25.9	25.9	48.2	1.00
CIS8617	24.8	26.3	48.9	1.06

Table 2.4 Results of hot-point probe and Hall effect measurements for nonstoichiometric samples

Sample No.	Starting Composition	Conduction Type	Mobility ($cm^2/V\text{-}s$)	Resistivity (ohm-cm)	Carrier Conc. (cm^{-3})
CIS9104	$(Cu_2Se)_{0.42}(In_2Se_3)_{0.58}$	p	23	5.9	4.6×10^{16}
CIS9114	$(Cu_2Se)_{0.46}(In_2Se_3)_{0.54}$	p	47.2	0.3	4.4×10^{17}
CIS81231	$(Cu_2Se)_{0.44}(In_2Se_3)_{0.56}$	n	65.1	2.3	4.1×10^{16}
CIS81219	$(Cu_2Se)_{0.48}(In_2Se_3)_{0.52}$	n	263	1.5	1.5×10^{16}
CIS9109	$CuInSe_2$ + 1 wt% Sb	n	123.5	1.6	3.2×10^{16}

Table 2.5 Compositions of nonstoichiometric samples determined by electron probe microanalysis

Sample no.	Starting composition (at.%)			Measured composition (at.%)			Remarks
	Cu	In	Se	Cu	In	Se	
CIS9104	20.2	27.9	51.9	22.3	27.6	50.1	42% Cu_2Se, 58% In_2Se_3
				15.3	31.9	52.8	Top region of CIS90104
CIS81231	21.3	27.0	51.7	23.1	27.5	49.4	44% Cu_2Se, 56% In_2Se_3
				20.2	29.3	50.5	Top region of CIS81231
CIS9114	22.5	26.5	51.0	24.1	27.2	48.7	46% Cu_2Se, 54% In_2Se_3
CIS81219	23.8	25.7	50.5	25.7	26.0	48.3	48% Cu_2Se, 52% In_2Se_3

Table 2.6 Measured compositions of three different regions in the Sb-doped sample

Region	Measured Composition (at.%)				Remarks
	Cu	In	Se	Sb	
1	25.9	25.1	48.9	0.1	Typical compositions in the bulk
2	20.7	1.4	20.4	57.5	Region with high Sb conc.
3	0.9	0.0	0.2	98.9	Region with very high Sb conc.

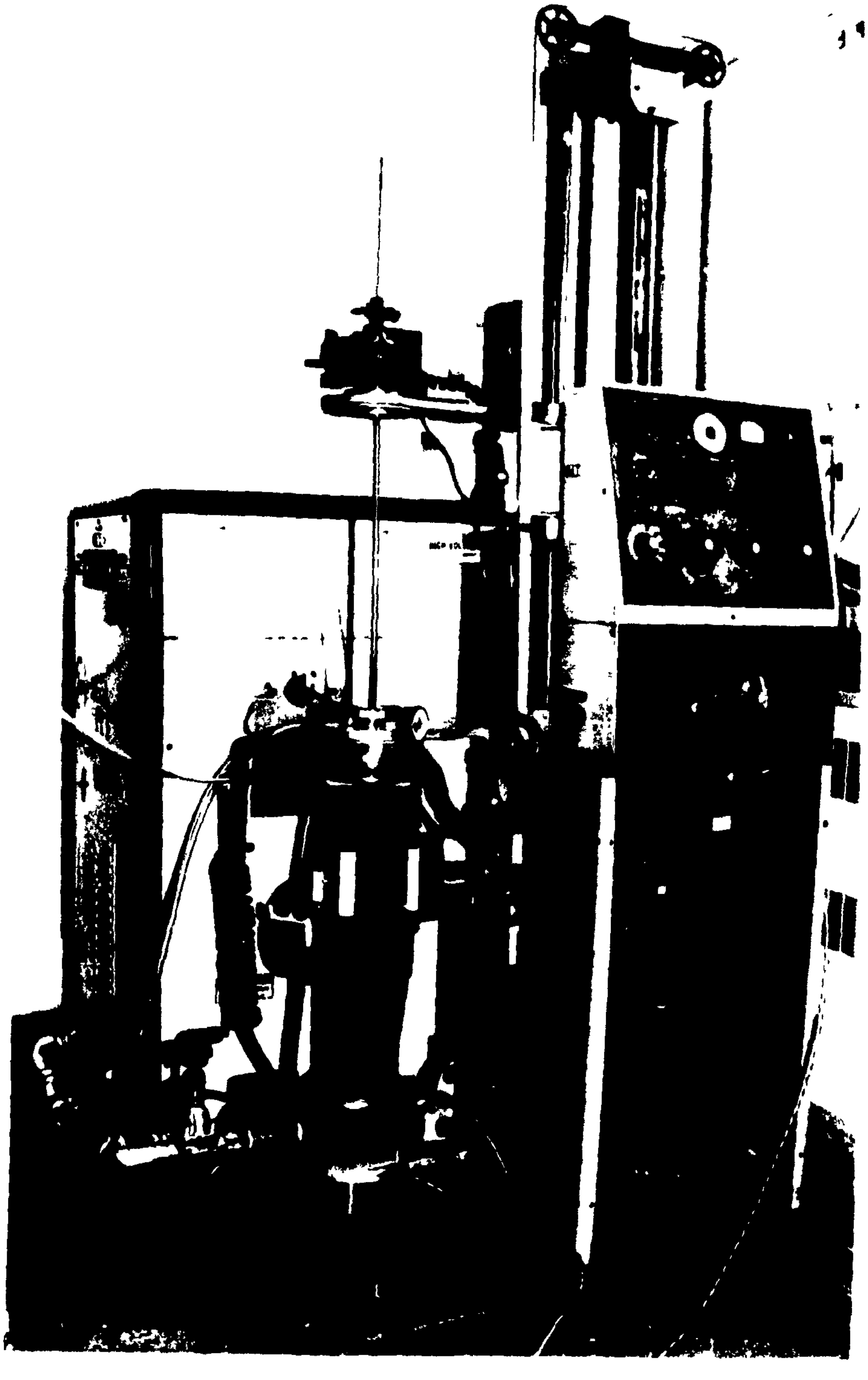

Fig. 2.1 A photograph of the crystal growth system.

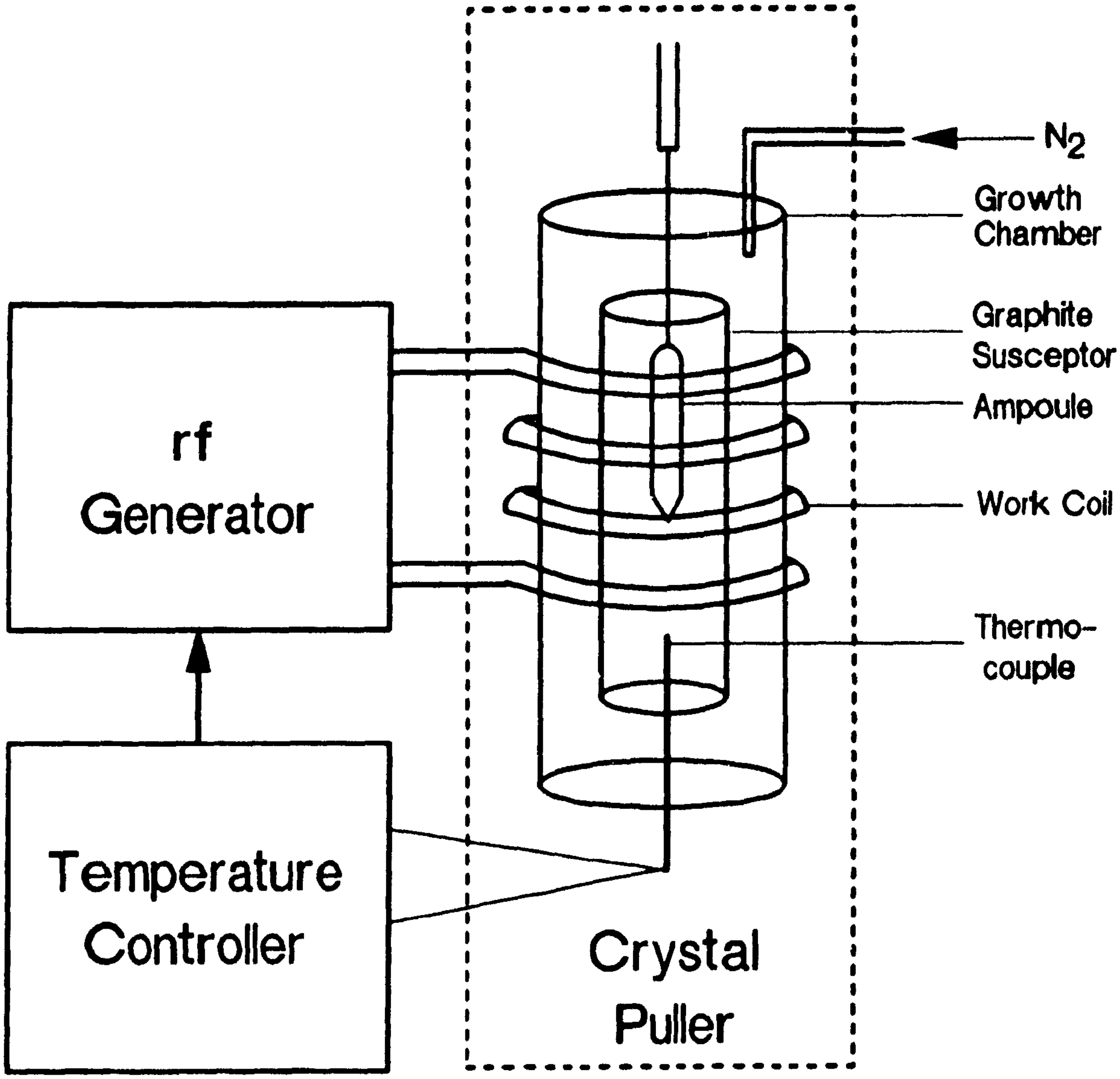

Fig. 2.2 A schematic of the crystal growth system.

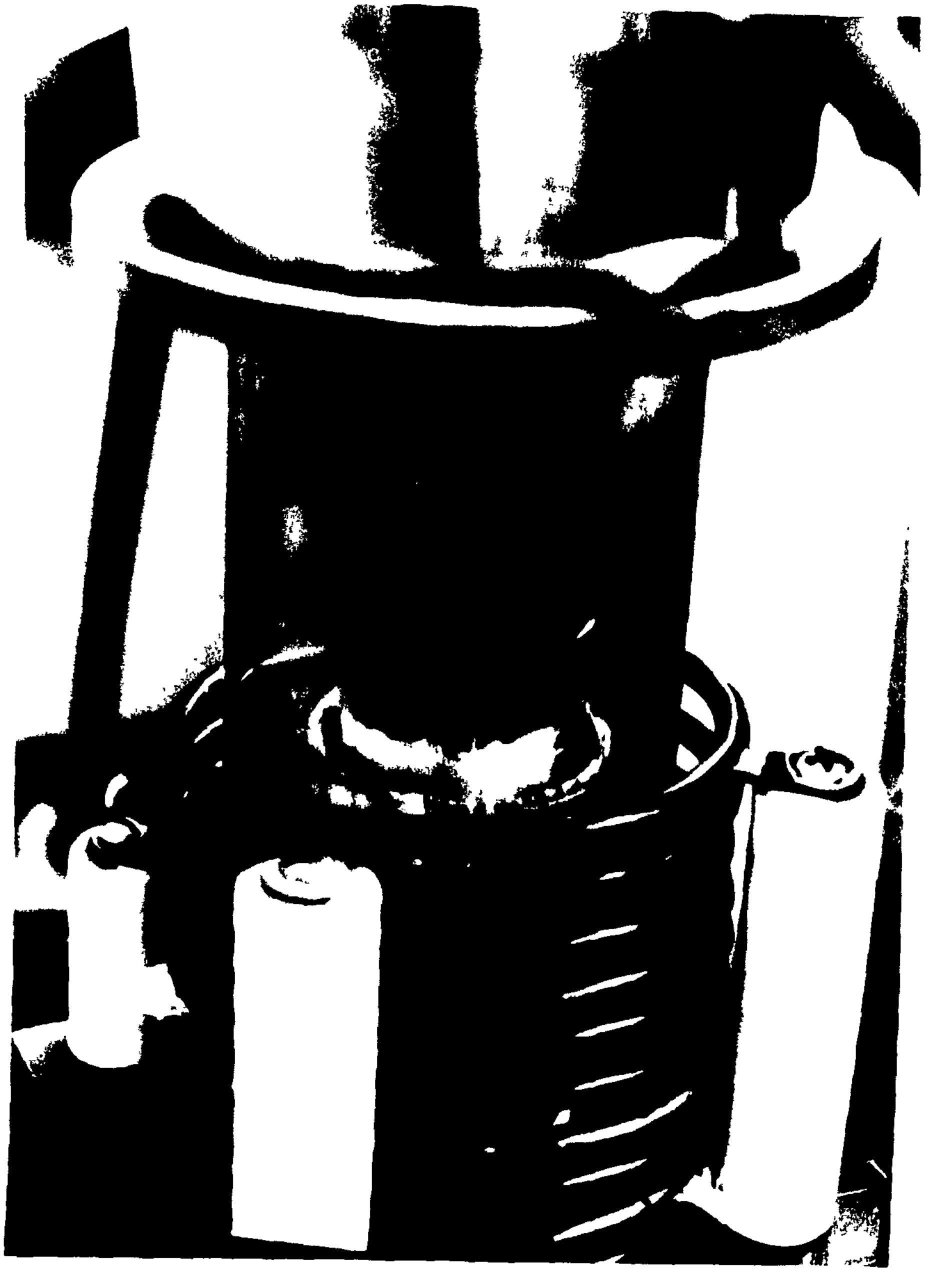

Fig. 2.3 A photograph of the growth chamber.

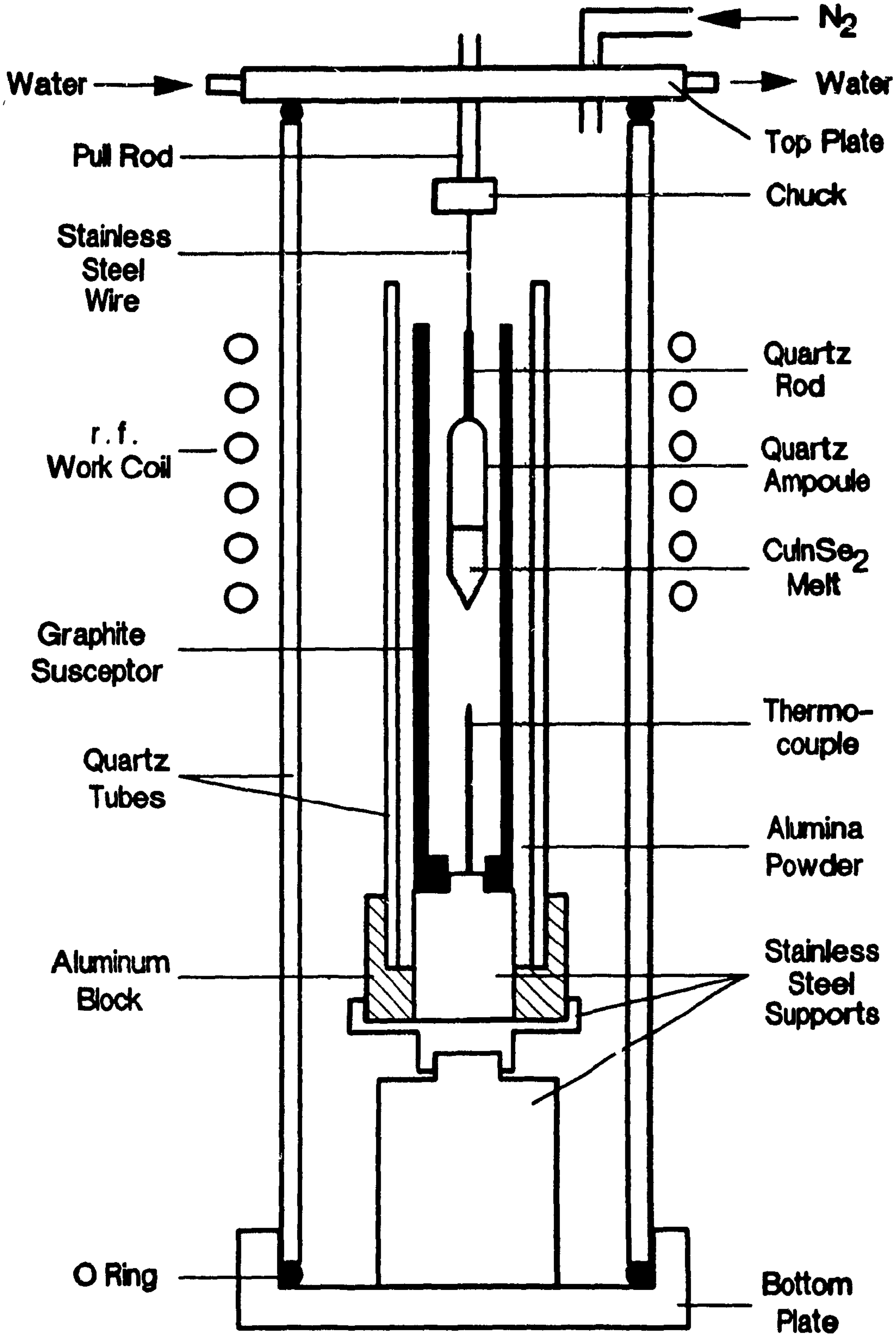

Fig. 2.4 A schematic of the growth chamber.

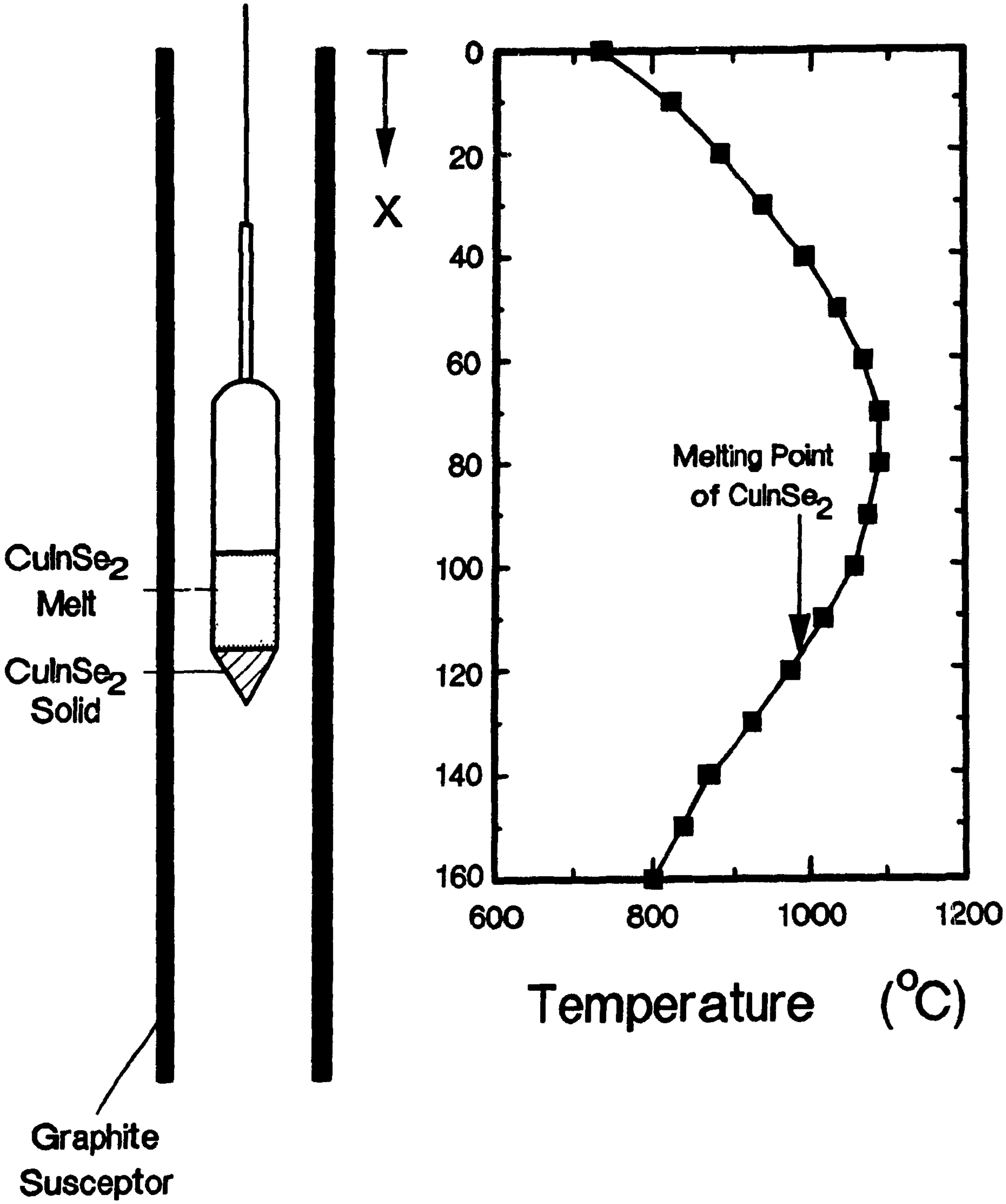

Fig. 2.5 The temperature profile along the graphite susceptor in the growth system. X is the distance from the top of the graphite susceptor.

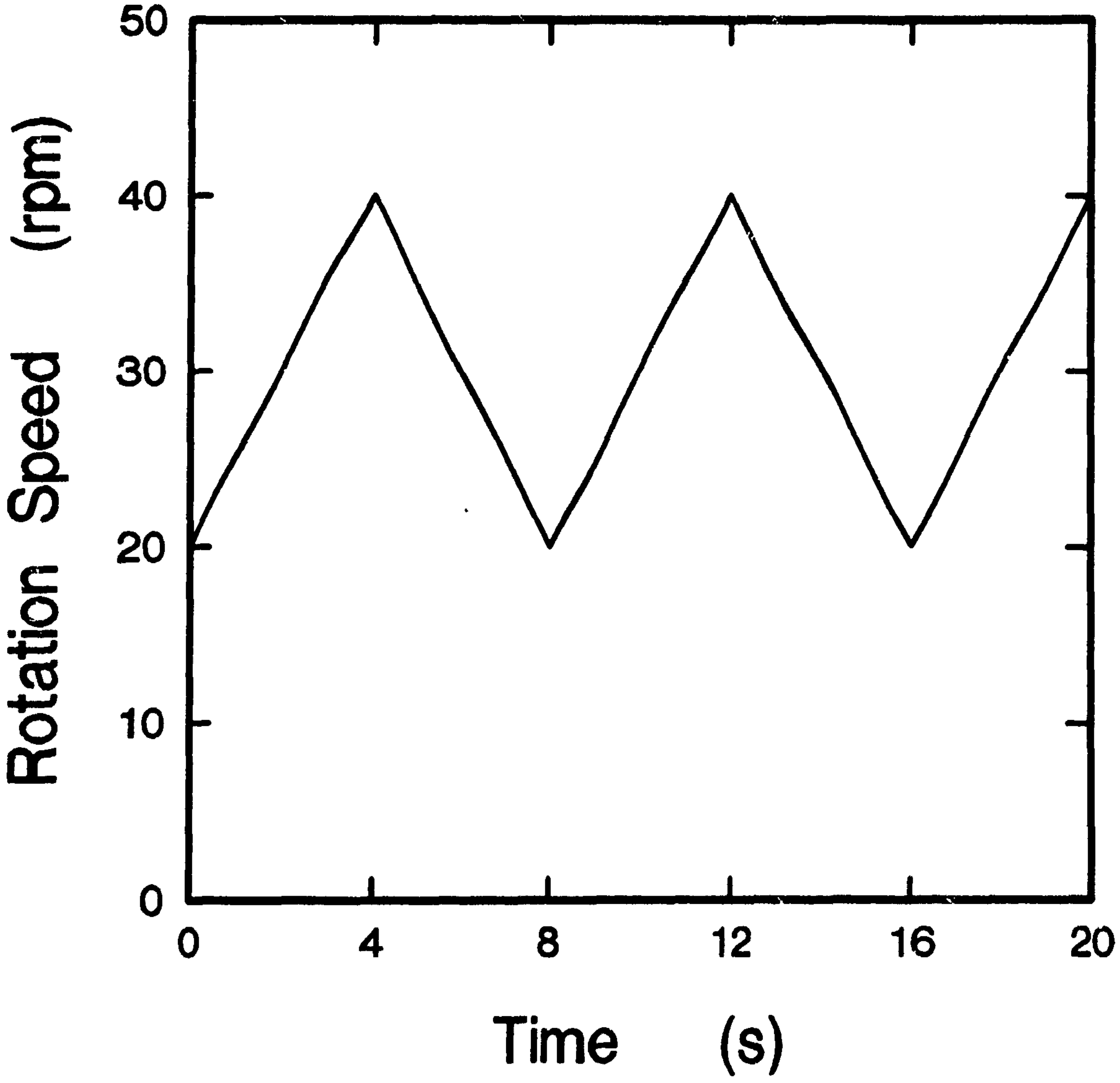

Fig. 2.6 A plot of the rotation speed against time for the accelerated crucible rotation technique (ACRT).

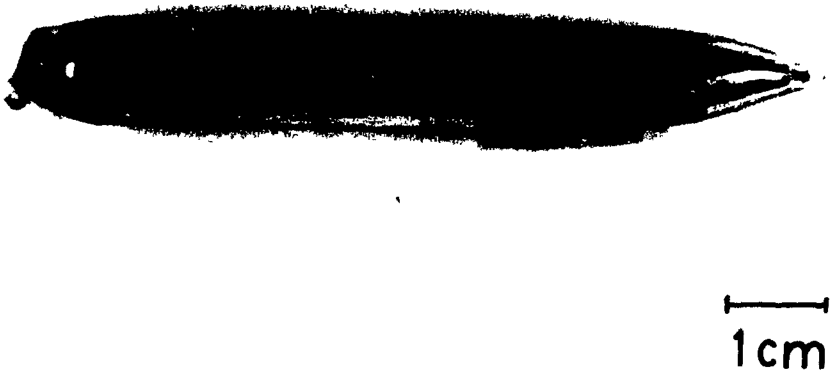

Fig. 2.7 A photograph of an as-grown ingot inside the ampoule.

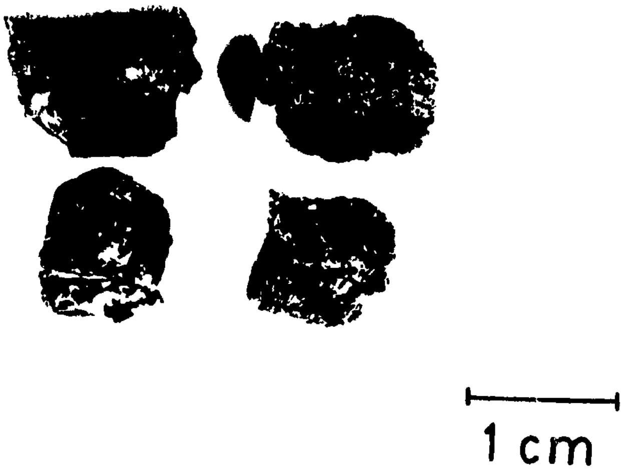

Fig. 2.8 Polycrystalline samples with a lot of voids.

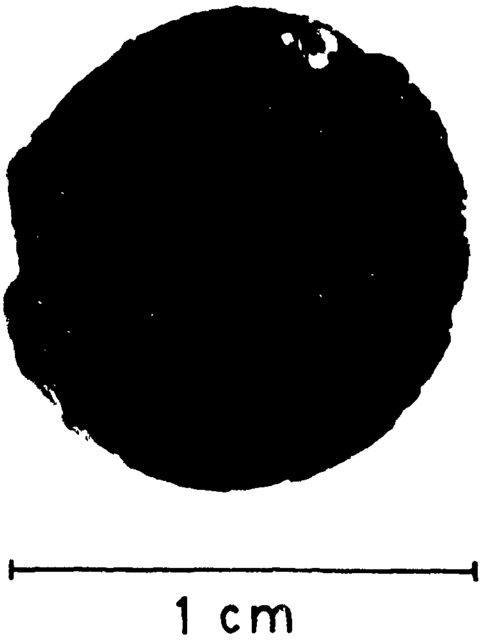

Fig. 2.9 (a) A sample cut perpendicularly to the growth direction. No void but one small crack can be seen.

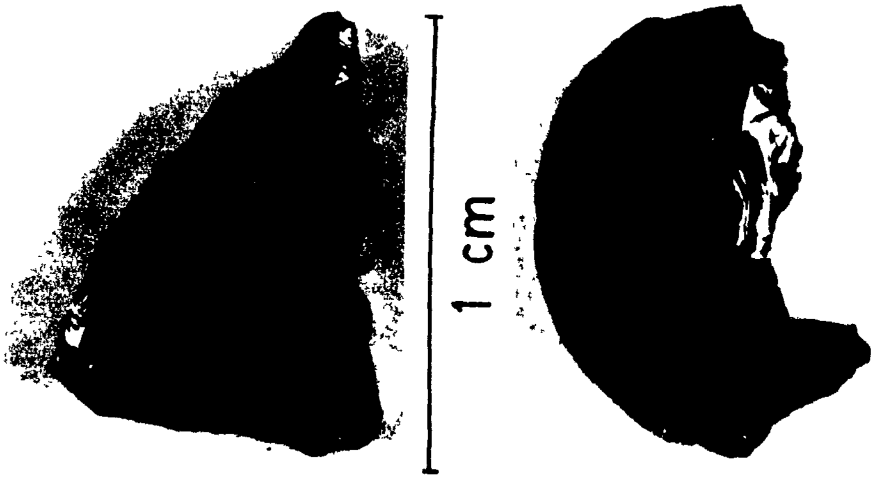

Fig. 2.9 (b) Two samples cut from the same ingot. The triangular sample was cut along and the other one perpendicular to the growth direction. No void or crack can be seen on the two samples.

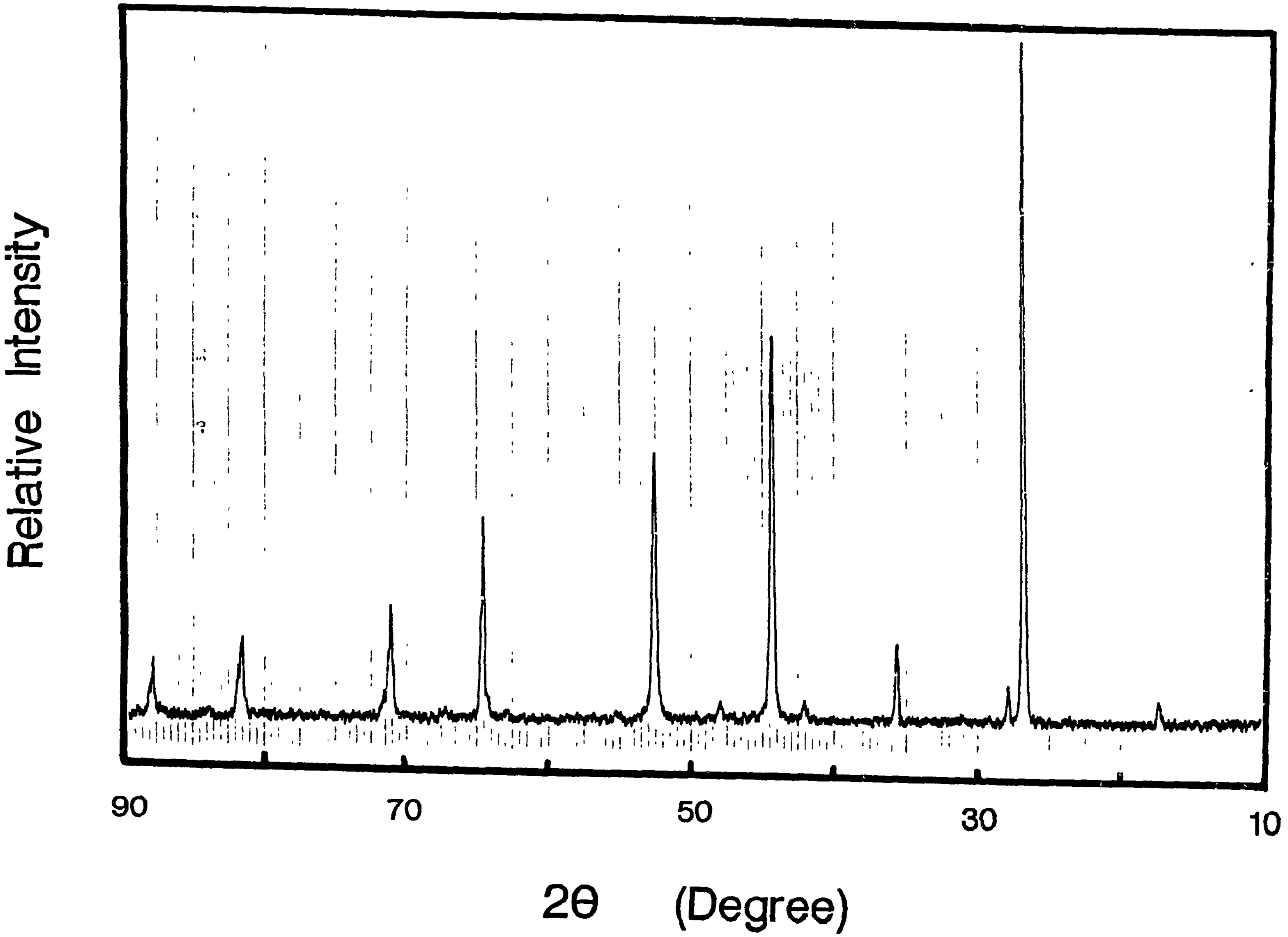

Fig. 2.10 X-ray powder pattern of a sample.

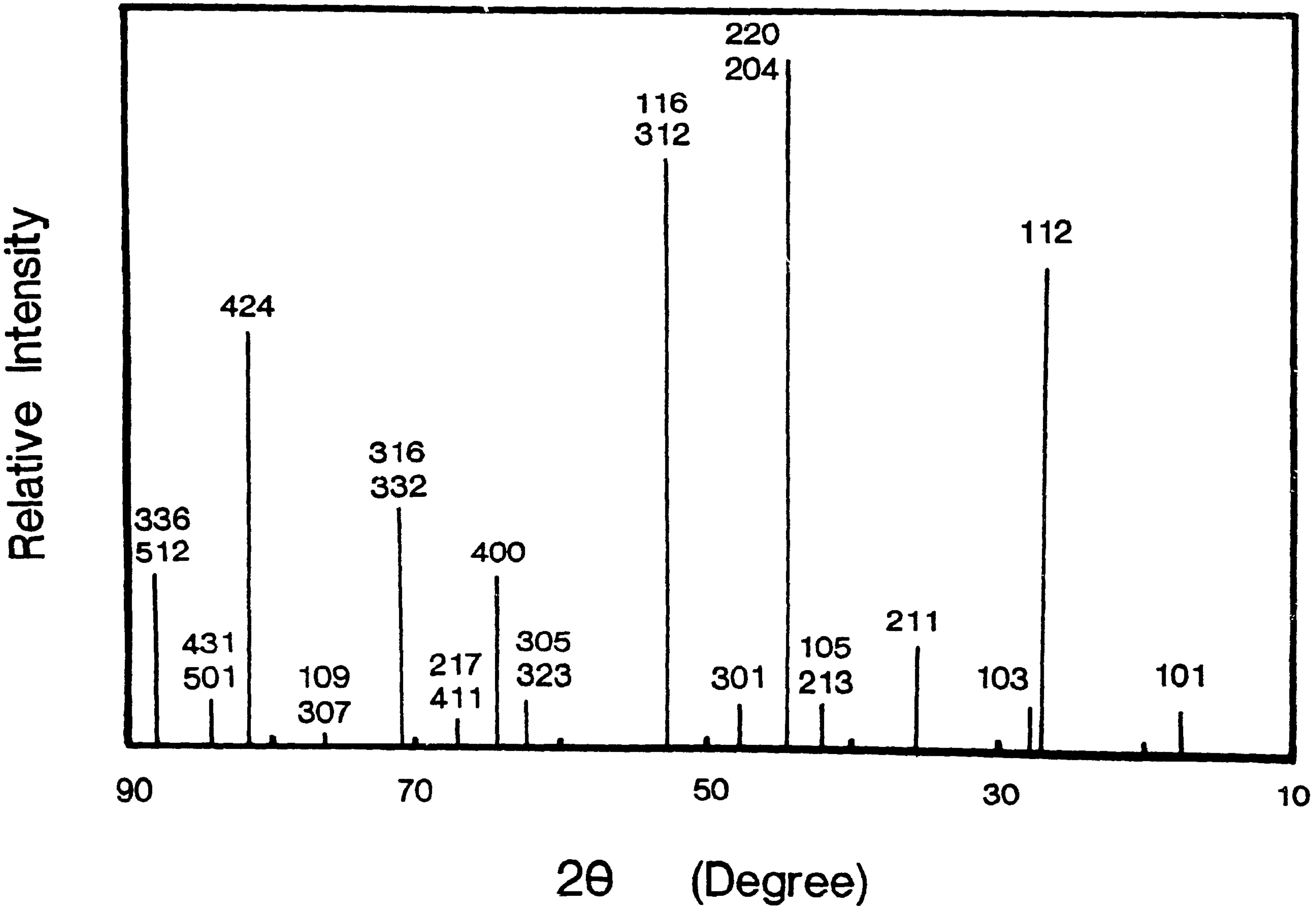

Fig. 2.11 X-ray powder pattern obtained from ASTM data for $CuInSe_2$ with the chalcopyrite phase.

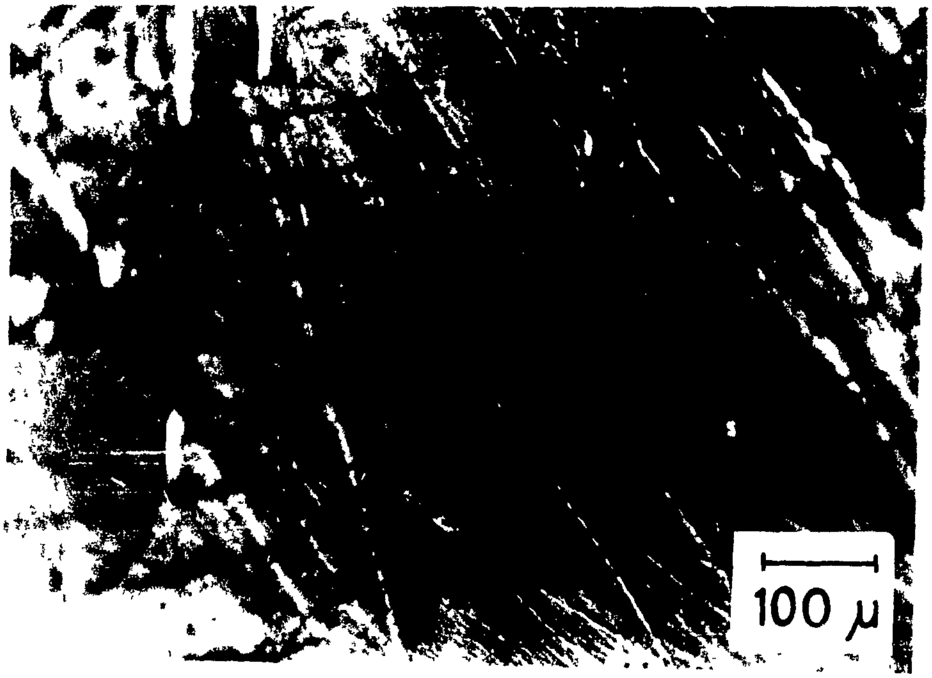

Fig. 2.12 A sample revealing microcracks after chemical etching.

Fig. 2.13 Grain boundary can be seen on this sample after chemical etching.

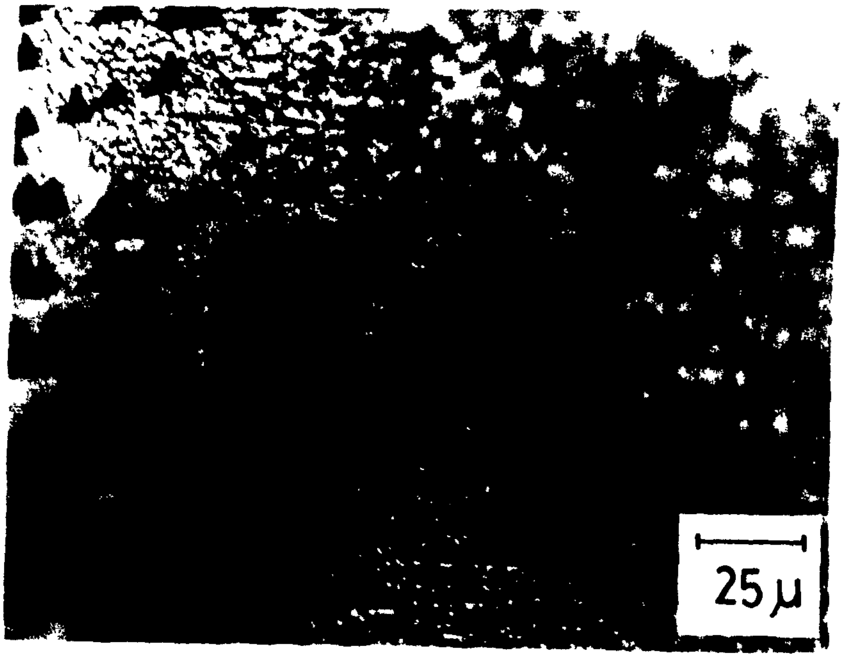

Fig. 2.14 Etch pits are apparent on a sample after chemical etching.

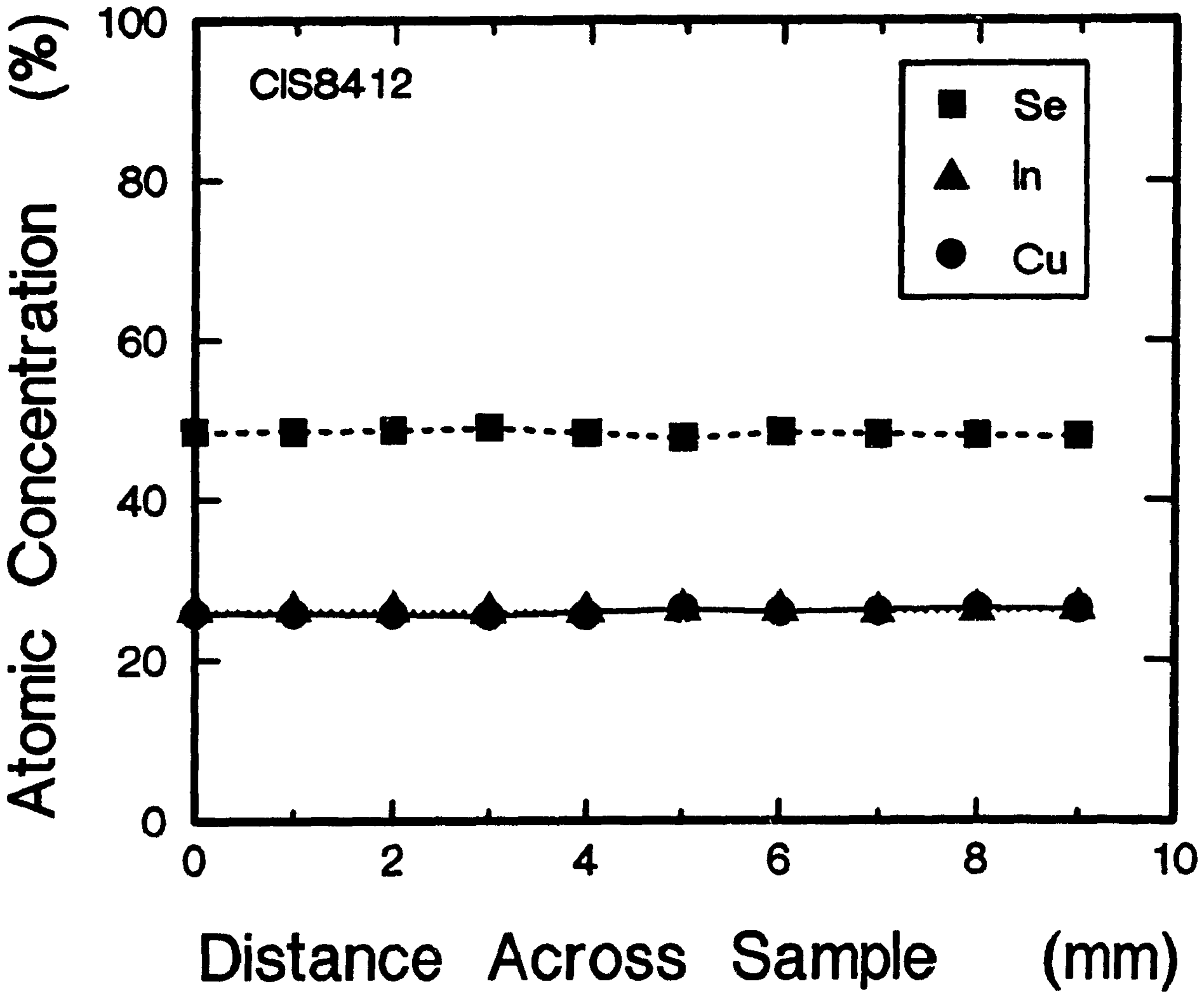

Fig. 2.15 A plot of the measured compositions against distance across a sample grown from stoichiometric starting compositions. Compositional uniformity was observed.

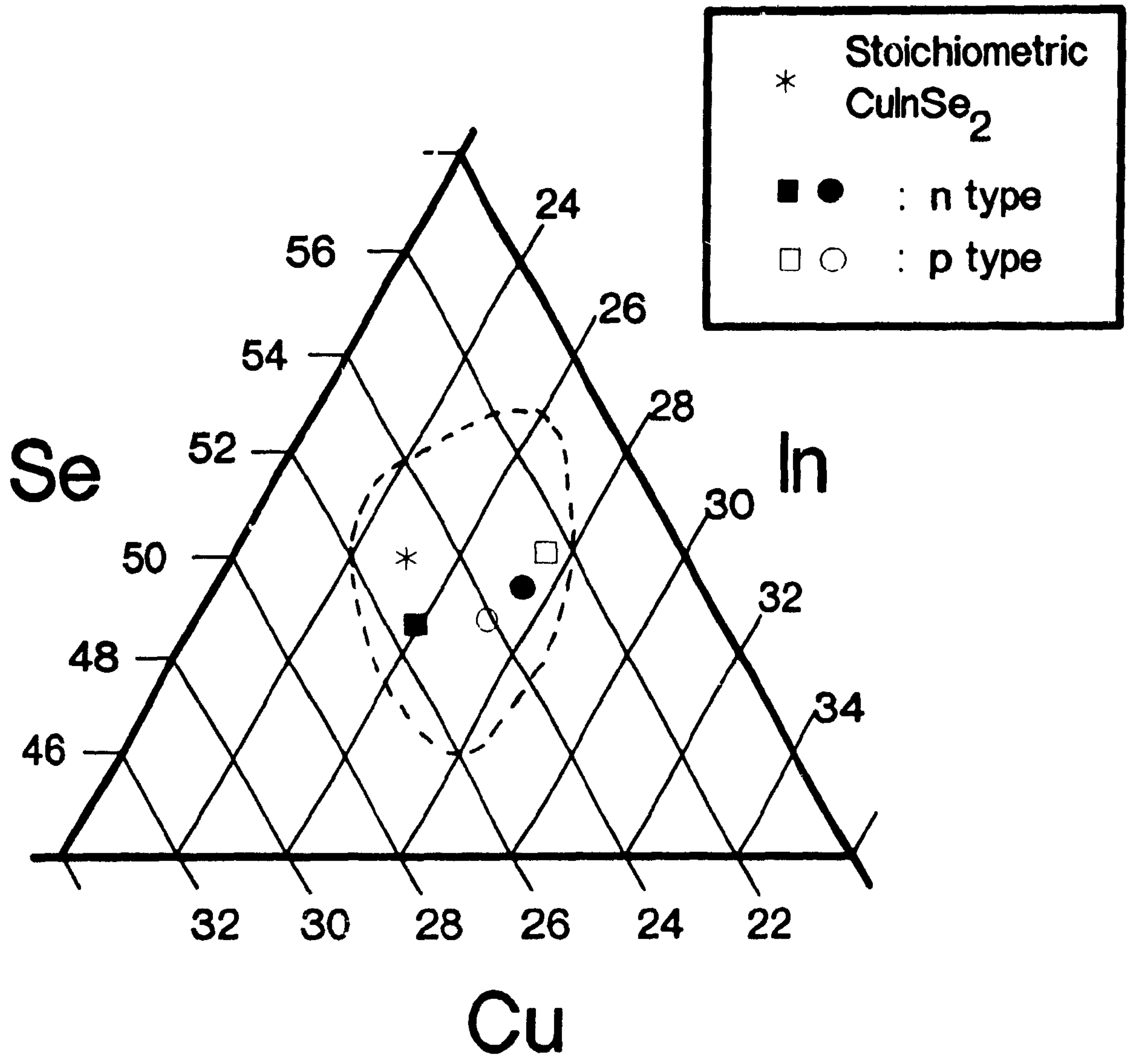

Fig. 2.16 A figure showing the measured compositions of the nonstoichiometric samples in the phase diagram. The area enclosed by the dotted line is the compositional range over which high efficient solar cells have been reported [2.23].

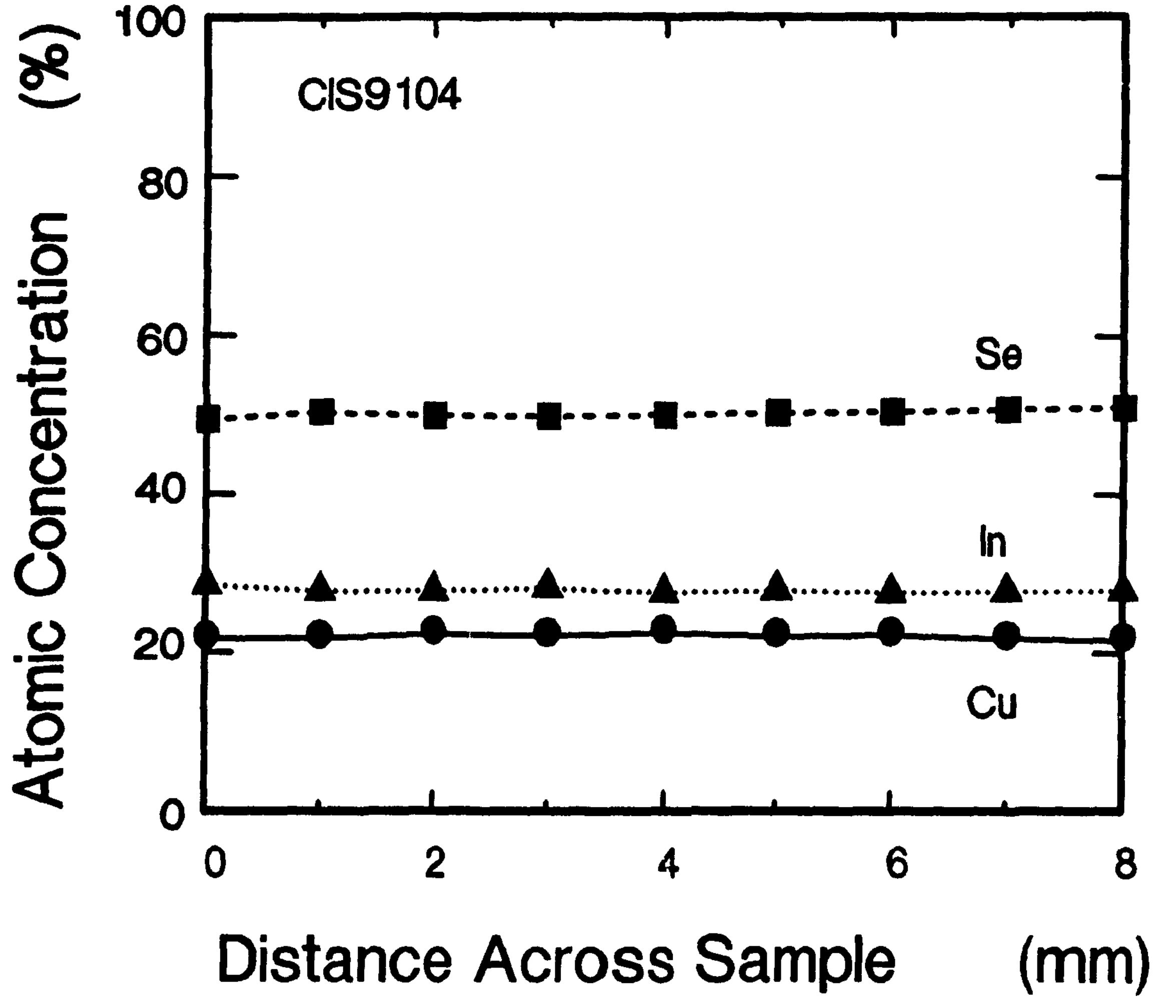

Fig. 2.17 A plot of measured compositions against distance across the growth plane of a nonstoichiometric sample. Compositions were uniform across the growth plane.

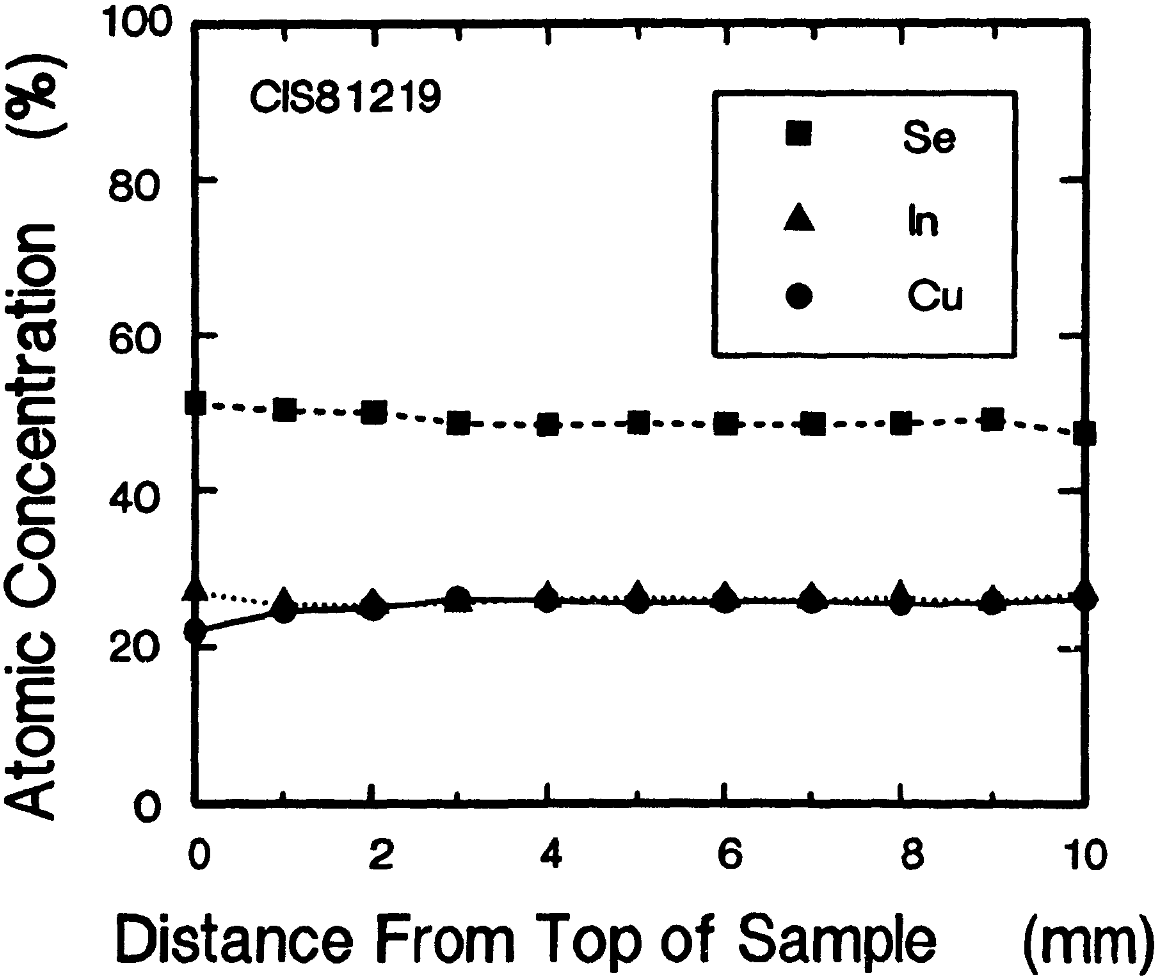

Fig. 2.18 A plot of measured compositions as a function of distance from the top of a sample. Deficiency of copper is apparent in the top region of this sample.

CHAPTER 3

PREPARATION BY RF MAGNETRON SPUTTERING AND CHARACTERIZATION OF YTTRIUM OXIDE FILMS

3.1 INTRODUCTION

To study the metal-insulator-semiconductor structure, an insulating film should be formed on the top of the semiconductor. Various methods have been reported on the formation of insulating films. Using Si as the substrates, the most commonly used method is the thermal oxidation of Si at elevated temperature. However, if the actual surface properties are to be studied on the Si surface, this method is not desirable because of the impurity redistribution near the SiO_2-Si surface during oxidation [3.1]. On the other hand, thermally grown oxide cannot be readily obtained on most compound semiconductors such as GaAs and $CuInSe_2$. Although thermal oxidation of GaAs has also been reported [3.2], the oxide consisted of both Ga_2O_3 and As_2O_5 and the properties were considered to be inferior than thermally grown SiO_2. Other film formation method such as anodic growth, thermal evaporation, chemical vapor deposition and sputtering have also been widely used [3.3]. Using $CuInSe_2$ as substrates of the MIS capacitors, a low-temperature film deposition method is preferred; otherwise, Se out-diffusion would occur. Although a variety of film-deposition techniques are available, rf sputtering has been demonstrated to be convenient and suitable in low-temperature deposition of insulating thin films [3.4, 3.5].

Among the many dielectrics studied, yttrium oxide (Y_2O_3) has been shown to have good dielectric properties. Thermally evaporated Y_2O_3 films with a 3000 Å thickness were prepared by Tsutsumi [1.15] and were reported to have a dielectric constant of 13 and a breakdown field of $3x10^6$ V/cm. Manchanda and Gurvitch [1.16] also reported that by thermally oxidizing sputtered yttrium films, they have prepared Y_2O_3 films (260 Å thick) with a very low leakage current density (less than 10^{-10} A/cm at a field of $1.9x10^6$ V/cm), a dielectric constant of 12, and a breakdown field of about $4.5x10^6$ V/cm. A comparison of the dielectric constant, breakdown field and resistivity of few commonly used insulating films along with Y_2O_3 is shown in Table 3.1. It can been seen that Y_2O_3 films have a comparably higher dielectric constant and a higher resistivity than several commonly-used insulating films. Thin films of Y_2O_3 may, therefore, be used as the insulator in the MIS structure. Manchanda and Gurvitch [1.16] even suggested the use of Y_2O_3 films as the high quality dielectric in circuit applications because of the high dielectric constant and low dielectric loss of Y_2O_3. In the present work, an rf planar magnetron sputtering method was used for the deposition of Y_2O_3 films. Characterization of the Y_2O_3 films has been carried out by examining the properties of the Y_2O_3 on Si and $CuInSe_2$ substrates.

In section 3.2, the principle of rf planar magnetron sputtering will be briefly explained. The sputtering system and the sputtering procedure will be described in section 3.3. In section 3.4, the results of the characterization of the Y_2O_3 films will be presented.

3.2 PRINCIPLES OF RF PLANAR MAGNETRON SPUTTERING

The sputtering technique has been widely used to deposit a variety of thin films of metals, semiconductors and insulators. In the present work, the rf planar magnetron sputtering technique has been employed for the deposition of Y_2O_3 films. The basic principles of this technique will be described in this section.

3.2.1 Basic Concepts of Sputtering

In sputtering deposition, a target consists of the material to be deposited is bombarded by gas ions as illustrated in Fig. 3.1. The atoms on the surface of the target material are then removed by the bombardment of the incident gas ions. The atoms removed from the target eventually hit and condense on the substrates to form a layer of film. The gas ions are created in a region between the target and the substrates by an avalanche breakdown, due to the high potential maintained between the substrates and the target, of the sputtering gas (usually argon). This region is usually referred as the glow discharge region or plasma glow region.

Two types of sputtering, the dc sputtering and the rf sputtering, are commonly used. In dc sputtering the target is constantly maintained at a high negative potential as the cathode; while in rf sputtering the rf field makes the target as a cathode only during half of the rf cycle. The positive gas ions are then accelerated toward the target and remove the target atoms by momentum transfer. Heat is also generated at the target because a large part of the impact energy of the gas ions is lost as heat. There are also other particles produced at the target when the gas ions hit the target. One of them which is worth to mention is the secondary electrons. They are emitted with a large potential and help to sustain the glow discharge by ionization of the sputtering gas. However, a lot of these energetic electrons will also hit the substrates. Most of the impact energy is dissipated as heat at the substrates and film quality may be affected by this uncontrolled heating. It is clearly that cooling (usually water-cooling) is, therefore, necessary for both the target and the substrates. However, most of the secondary electrons can be prevented from reaching the substrates using the magnetron method as described in next section.

3.2.2 Rf Planar Magnetron Sputtering

It is apparent that the dc sputtering can only be used for the deposition of conductor, which can be electrically maintained at a high negative potential. For the deposition of insulator, the rf sputtering should be used. Conductor can also be deposited by rf sputtering by capacitively coupled the conducting target to the cathode. In rf sputtering, electrons in the glow discharge region are oscillating with the rf signal and gaining sufficient energy to cause gas ionization. The ionization probability is, thus, substantially increased by these oscillating electrons. As a result, rf sputtering permits the use of lower sputtering gas pressures and thus generally purer films. Since the rf voltage makes both electrodes as a cathode alternately for half a cycle, one might expect sputtering on both electrodes (target and substrates). However, this is not the case. It is because the rf frequencies used for sputtering are in the range of MHz (typical frequency is 13.56 MHz), which are sufficiently high to cause most of the gas ions (but not the electrons) to be immobile. One might again expect negligible sputtering to occur on both electrodes. Fortunately, this is again not true. One should note that the target must be an insulator or capacitively coupled to the rf generator. Owing to the difference in mobility of the gas ions and electrons, more electrons hit the target during the half cycle when the target is positive than the positive gas ions when the target is negative. Eventually, a negative dc bias is built up in the insulating target. This negative self bias, then, provides the necessary potential for sputtering. The condition becomes similar to dc sputtering. On the other hand, the directly coupled electrode (substrate holder and anode), which is usually grounded and, therefore, without the self bias, is subjected to negligible ion bombardment. That is, only the target is sputtered.

In magnetron sputtering, a magnetic field is aligned perpendicularly to the electric field, i.e. parallel to the target surface, so as to confine the electrons to a region close to the target surface. The planar magnetron cathode is shown in Fig. 3.2. It consists of permanent magnets which are arranged to provide closed magnetic field lines on the target surface as in Fig. 3.2. These magnetic field lines form a closed tunnel on the target surface and confine the electrons within the boundaries of the field lines. The path of the electrons in this region is related to the **E** x **B** Lorentz force. Therefore, the electrons circulate in helical paths about the closed magnetic field lines, this helical motion gives an extended path length resulting in more ionization of gas atoms. Some of the electrons eventually reach the perimeter of the target where the field lines terminate. The target is usually surrounded by an additional anode ring, which collects most electrons from the perimeter of the target and prevents them from reaching the substrates. The number of electrons escaping from the target is usually very small, electron bombardment of the substrates is thus minimized. Since the electrons are confined within the magnetic field, ionization of the gas atoms is concentrated in this region. In this case, a higher sputtering yield is obtained.

The properties of the deposited films are usually affected by the sputtering parameters such as the sputtering gas pressure, gas composition, rf power and substrate temperature. To obtain films with very high quality, the optimum sputtering conditions are usually determined experimentally.

To conclude, using the rf planar magnetron sputtering, insulating films can be deposited efficiently with a relatively high deposition rate, a low gas pressure, and a minimal substrate heating.

3.3 EXPERIMENTAL

3.3.1 The Sputtering System

An rf planar magnetron sputtering system has been employed for the deposition of Y_2O_3 films in the present studies. The system consisted of a planar magnetron sputtering source (US' Gun II , US Inc.), a 500 W rf power supply (13.56 MHz, with auto tuning) and a Varian vacuum system with a high vacuum diffusion pump. A schematic of the sputtering system is shown in Fig. 3.3. A central and a ring permanent magnets were arranged in the target support in such a way to provide the toroidal magnetic field (see Fig. 3.2) as required in planar magnetron sputtering. An anode ring surrounding the target was also furnished. The high vacuum system also contained an orific to control the gas pressure for sputtering.

3.3.2 Preparation of the Substrates

MIS capacitors in the form of Al-Y_2O_3-Si and Al-Y_2O_3-$CuInSe_2$ have been fabricated and studied. From here on, the metal(Al)-Y_2O_3-Si capacitors will be denoted as MYS capacitors while the metal(Al)-Y_2O_3-$CuInSe_2$ capcitors will be referred as MYC capacitors.

(i) Si Substrates

The Si substrates used for the MYS capacitors were p-type and had a resistivity of 10 Ω-cm and an orientation of (100). The Si wafers were chemically cleaned with a standard cleaning procedure using trichloroethylene, aceton and $H_2SO_4+H_2O_2$. After the cleaning, the ohmic back contact of the p-Si's was formed by evaporating a layer of Al at the back of the Si wafers and then baking the wafers in a N_2 environment at 450 °C for 20 minutes. The front surface of the Si wafers was then etched by a clean buffer HF solution to removed any SiO_2 on the Si surface. The Si wafers were then ready for the Y_2O_3 deposition.

(ii) $CuInSe_2$ Substrates

Monocrystalline $CuInSe_2$ pieces were selected from the ingots grown by the vertical Bridgman method described in chapter 2 as the substrates for the MYC capacitors. Each $CuInSe_2$ crystal was bonded to an Al plate using silver paste. The silver paste hardened when baked at 160 °C for about 10 minutes. Silver paste was reported to form an ohmic contact with p-type $CuInSe_2$ [2.17]. The $CuInSe_2$ substrates were then mechanically polished with 0.5 μm alumina powder, cleaned with aceton and rinsed with deionized water before being loaded into the sputtering system. In several cases the $CuInSe_2$ substrates were also etched with a mixture of $H_2SO_4+K_2Cr_2O_7$ (9:1 by weight).

3.3.3 The Sputtering Procedure

Powder of Y_2O_3 with 99.9% purity was pressed into a metal holder to form the target. The target was then fixed tightly onto the water-cooled target support. After the preparation of the substrates, the substrates were fixed onto the substrate holder. The substrate holder, with the substrates facing downward toward the target as in Fig. 3.3, was then placed about 4 cm over the target. The back of the substrate holder was connected to a water-cooled copper coil to provide the cooling for the substrates. Therefore, the substrates were presumably subjected to minimal heating during the sputtering process. The chamber was then evacuated first by the rotary pump and then by the diffusion pump to a pressure of 10^{-6} torr. After this, the chamber was refilled with the sputtering gas (50% Ar and 50% O_2) to a pressure of about 10 mtorr by adjusting the orifice. The plasma glow was then started. The pressure was then reduced to 1 mtorr and the rf power was increased to 60 watt to begin the sputtering. Presputtering of the target (without the present of substrates) was also carried out prior to every deposition in order to clean the target surface and to cover the interior of the chamber with a layer of film so that contamination from the background would be reduced. No attempt has been made in order to optimize the quality of the Y_2O_3 film by varying the deposition parameters such as gas pressure, gas composition, rf power and substrate temperature. However, preliminary experiments had been done to obtain the present conditions for the sputtering. Samples with different Y_2O_3 thicknesses were prepared by controlling the sputtering time.

3.3.4 Evaporation of Al

After the deposition of the Y_2O_3, aluminum was thermally evaporated through a metal mask onto the Y_2O_3 films using an

Edward E360A coating system. Aluminum dots with an area of 3.1×10^{-2}, 8.9×10^{-3} or 5.2×10^{-3} cm^2 and a thickness of about 1 μm were then formed as the metal gate of the MIS capacitors. Schematics of the MYS and MYC structure are shown in Fig. 3.4.

3.4 EXPERIMENTAL RESULTS

3.4.1 Determination of the Dielectric Constant of Y_2O_3 Films

The vacuum-evaporated Y_2O_3 films prepared by Tsutsumi [1.15] was reported to have a dielectric constant of about 13. Whereas the Y_2O_3 films prepared by Manchanda et al. [1.16] employing the thermal oxidation of yttrium had a dielectric constant of about 12. It appears that the dielectric constant depends on the film deposition method and should be determined experimentally.

In the present work the dielectric constant was determined by measuring the differential capacitance of several MIM (metal-insulator(Y_2O_3)-metal) capacitors. These MIM capacitors were fabricated by sputtering a layer of Y_2O_3, using the method described above, on Mo-coated glass substrates. Aluminum dots were then evaporated onto the Y_2O_3 to form the second electrode of the MIM structure. The capacitance of a MIM capacitor can be expressed as

$$C = \epsilon_o \epsilon_Y A/t, \tag{3.1}$$

where C is the capacitance of the MIM capacitor, ϵ_o is the permitivity of free space, ϵ_Y is the dielectric constant of the Y_2O_3 film, A is the area of the capacitor, and t is the thickness of the Y_2O_3 film. The thickness of the Y_2O_3 film was measured by a profilometer (Dektak Surface Profile Measuring system, Sloan Tech. Corp.) with a mechanical stylus. Having measured the capacitance and the film thickness, the dielectric constant of the Y_2O_3 film can be easily determined using equation (3.1).

The capacitance of a MIM capacitor is plotted against the dc bias in Fig. 3.5 for three different frequencies. The capacitance is clearly not bias-dependent as expected but is slightly frequency-dependent. The dielectric constant was determined using equation (3.1) to be 12.0, 11.7 and 11.6 at 1 kHz, 10 kHz and 100 kHz respectively. The dielectric constant determined using other MIM capacitors was also in the vicinity of 12. Therefore, the dielectric constant of the Y_2O_3 films prepared in the present work was taken to be 12 for most of the calculations.

3.4.2 Determination of Film Thickness

The thickness of the Y_2O_3 films and the oxide capacitance (accumulation capacitance) of several MYS capacitors were also measured. The dielectric constant was also confirmed to be about 12 using equation (3.1). In routine determination of the Y_2O_3 thickness of the MYS capacitors, the oxide capacitance (accumulation capacitance) was measured at 1 kHz. By taking the dielectric constant being equal to 12 and applying equation (3.1), the film thickness can be determined.

3.4.3 Al-Y_2O_3-Si Capacitors

(i) Direct-Current Conduction

The dc leakage current of the MIS capacitors was measured using an HP 4145A Semiconductor Parameter Analyzer. It is known that the dc leakage of a dielectric film is greatly affected by the present of impurities and local defects such as pin holes. Therefore, special care has been taken to minimize the contamination during the fabrication process. The leakage current of the capacitors was measured mainly with a negative gate voltage. The reason is that when a negative voltage is applied to the gate, an accumulation of holes (majority carriers) at the p-type Si surface makes it act as a semimetal. Therefore, the true dc leakage can be measured. On the other hand, in a positive gate bias a depletion layer is formed at the Si surface and this depletion region would impede the current flow and the intrinsic leakage of the insulator may not be measured.

Typical results of I-V measurements are shown in Fig 3.6 and Fig. 3.7 for two different MYS capacitors with 1200 Å and 500 Å thick Y_2O_3. In these two figures, the leakage current density was plotted as a function of the electric field across the Y_2O_3 films. In Fig. 3.6 an ohmic behavior of the film can be clearly seen and the corresponding resistivity is about 10^{13} Ω-cm. This value is comparable to resistivity of insulating films shown in Table 3.1. Only the capacitors with low leakage current were used for further experiments. In Fig. 3.7 an ohmic behavior can be seen at small electric field (below $3\text{x}10^5$ V/cm) with approximately the same resistivity as in Fig. 3.6; however, at larger field a nonlinear I-V relationship can be seen. As explained by Sze [3.8], this nonlinear behavior might be due to either field-enhanced thermal excitation of trapped electrons into the conduction band or tunnel emission of trapped electrons into the conduction band, or both.

The I-V characteristic of a capacitor with positive bias is also shown in Fig. 3.8. An ohmic behavior was also observed and the resisitivity was also about 10^{13} Ω-cm indicating the current mechanism was limited by the Y_2O_3 film rather than the depletion region formed at the Si surface at this range of electric field.

Since the resistivity values of the Y_2O_3 films obtained for different MYS capacitors were almost the same, it appears that the resistivity obtained was the intrinsic value of the Y_2O_3 films.

(ii) Breakdown Test

In characterizing insulating films the breakdown electric field is a very important parameter. A large current would pass through the insulator abruptly whenever the breakdown field of the insulator is exceeded. In the present work, the breakdown field was found by using a ramped voltage method. That is, a voltage ramp was applied to the gate electrode and the breakdown voltage or field was detected when a large current suddenly passed through the insulator. The result of a typical breakdown test with negative gate bias is shown in Fig. 3.9. It can be easily seen that the breakdown field is about 5×10^5 V/cm in this sample. The breakdown of the insulating films were irreversible as shown in Fig. 3.10. This figure depicts the I-V characteristic of the same sample in Fig. 3.9 but after the breakdown of the film. It can be seen that a large current flew through the insulator even at a low electric field after the breakdown. The largest breakdown field obtained so far was about 3×10^6 V/cm. The MIS capacitors were also tested for breakdown with positive gate voltage and the result is shown in Fig. 3.11. It was found that after the breakdown the current, instead of increasing sharply and continuously, saturated at a small value and increased slightly afterwards. This might be due to the depletion region formed at the Si surface, the current would then be limited by the depletion region after the breakdown.

It has been observed that the breakdown field varied from wafer to wafer exhibiting no association with the film thickness. This indicates that the breakdown field measured was not the intrinsic property of the Y_2O_3 films. However, the breakdown field of the capacitors on the same silicon wafer usually was found to be about the same with a few exceptions. This variation of the breakdown fields is believed to be due to defects or contamination in the Y_2O_3 films. Since the defect density and contamination condition should be similar on a wafer, the defect-related breakdown field of the MIS capacitors on the same Si substrate would then be the same as observed experimentally. Defect-related breakdown was also common for other insulating films [3.11, 3.12]. The breakdown voltages, with both negative and positive gate voltage, of the capacitors on the same substrate were measured on several capacitors. These breakdown voltages were then used as a guideline for other capacitors in further experiments. An individual capacitor would be tested for premature breakdown. If the capacitor passed the test, it would then be used for C-V measurements. The capacitors were normally operated below the breakdown voltages.

3.4.4 Al-Y_2O_3-$CuInSe_2$ Capacitors

The leakage current density against the electric field of a typical MYC capacitor with a 1200 Å-thick Y_2O_3 film is plotted in Fig. 3.12 for negative gate bias and in Fig. 3.13 for positive gate bias. The leakage current was large in this device as in the other MYC capacitors. Thicker Y_2O_3 films had also been deposited with the hope that smaller leakage could be obtained. However, Y_2O_3 films as thick as 0.4 μm also showed a large leakage. Breakdown test revealed that most MYC capacitors were unstable and exhibited a very small breakdown voltage, usually smaller than 1 V. Although the Y_2O_3 films deposited on Si substrates showed a good insulating properties, the Y_2O_3 films on $CuInSe_2$ did not reveal quite as good results. This is probably due to the difficulty in preparing clean and smooth surface on $CuInSe_2$, while the cleaning and etching procedures are standardized for Si. If Y_2O_3 is deposited onto a rough surface, the local spiky regions would make the effective thickness of the Y_2O_3 film in these regions smaller or even penetrate through the films. Furthermore, the spiky regions would have a much higher electric field than the flat regions. Therefore, even a small electric field would cause a premature breakdown of the Y_2O_3 film. Accordingly, etching of the $CuInSe_2$ crystals before Y_2O_3 deposition using a mixture of H_2SO_4 and $K_2Cr_2O_7$ (9:1 by weight) was carried out in several cases in order to smoothen the surface. However, no significant improvement has been obtained yet.

It is noted that the etching experiments have been little reported in the literature and no standard surface-preparation process has been commonly accepted for $CuInSe_2$. Recently, Yakushev et al. [3.13] observed near-surface deviations from stoichiometry in $CuInSe_2$ crystals following chemical etching by several commonly-used etches. However, no further results have been reported. It is, therefore, apparent that more work has to be done on the surface preparation of $CuInSe_2$ for device fabrication, especially for the fabrication of MIS capacitors.

3.5 CONCLUSIONS

Y_2O_3 films have been prepared by rf planar magnetron sputtering method in the present studies. The dielectric constant of the films prepared was found to be about 12. MIS capacitors in the forms of Al-Y_2O_3-Si and Al-Y_2O_3-$CuInSe_2$ were fabricated. The resistivity of the Y_2O_3 films on Si substrates was observed to be about 10^{13} Ω-cm at lower voltage. At higher voltage, the films exhibited a nonlinear I-V relationship. The breakdown field of the films was observed to be heavily dependent on the presence of defects in the films. The highest breakdown field obtained so far is about 3×10^6 V/cm. The Y_2O_3 films on $CuInSe_2$ substrates revealed a large dc leakage. Experimental results showed that the films had a very low breakdown field resulting in the large dc leakage. This might be due the difficulty in surface preparation of $CuInSe_2$.

It was found that Y_2O_3 with good insulating properties could be deposited by rf planar magnetron sputtering on monocrystalline

Si, indicating that rf planar magnetron sputtering provides a simple and convenient way to deposit good quality Y_2O_3 films. The sputtering process employed in this work was still far from optimization, and the quality of the sputtered films is yet to be improved. By closely monitoring the sputtering parameters (such as the rf power, sputtering gas composition and pressure, and substrate temperature) and employing a higher purity Y_2O_3 target, it is anticipated that higher quality Y_2O_3 films can be prepared.

Table 3.1 The properties of several commonly-used dielectric film

	dielectric constant	breakdown field (V/cm)	resistivity (Ω-cm)	preparation method
SiO_2	3.9	10^7	10^{14}-10^{16}	thermal oxidation [3.6]
SiO	4.1-8.0	1-5×10^6	10^{12}-10^{13}	evaporation [3.7]
Si_3N_4	4.8-5.8	10^7	5×10^{13}	silane-ammonia reaction [3.8]
Ta_2O_5	16-21	2×10^6	2×10^{11}	ion-beam evaporation [3.9]
Al_2O_3	8	2-4×10^6	10^{13}-10^{14}	electron-beam evaporation [3.10]
Y_2O_3	13	3×10^6	10^{15}	evaporation [1.15]

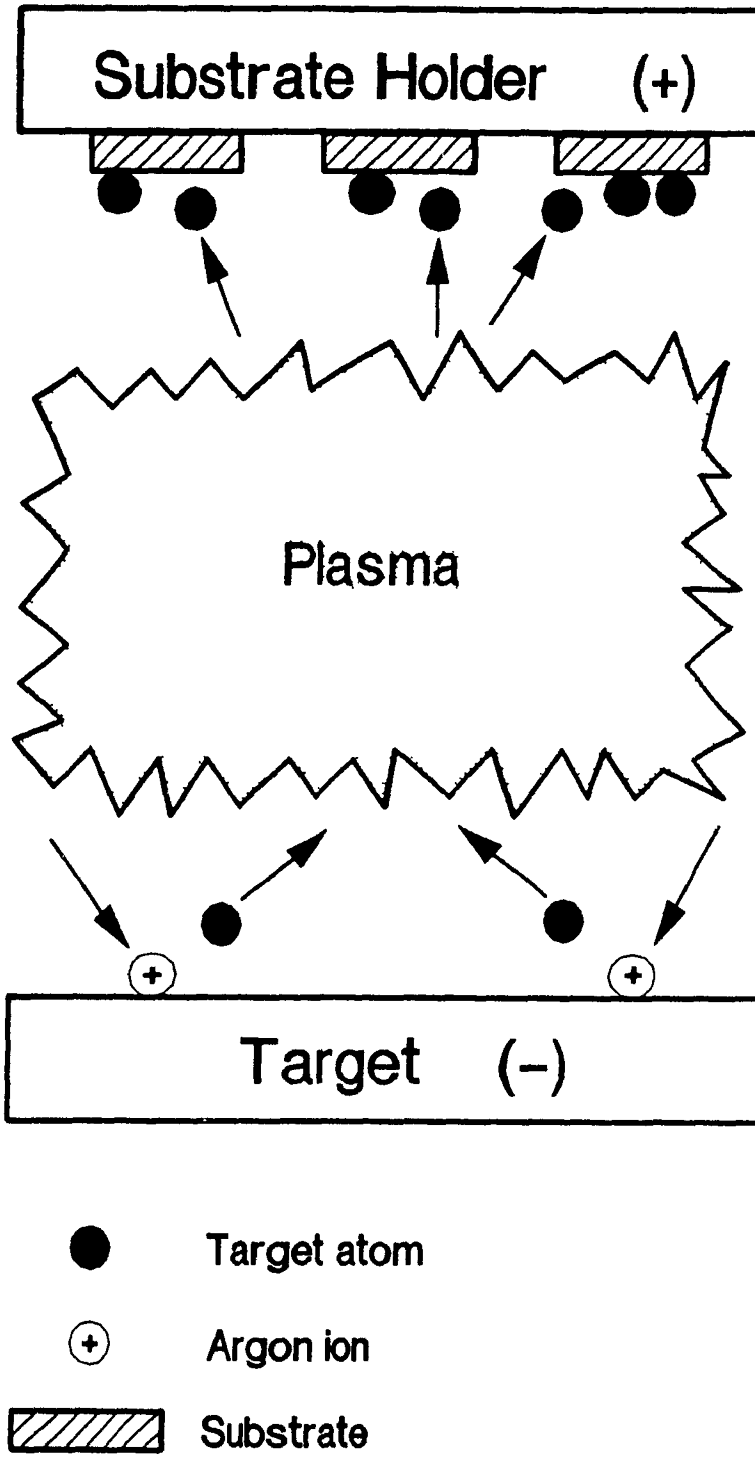

Fig. 3.1 Basic mechanism of sputtering.

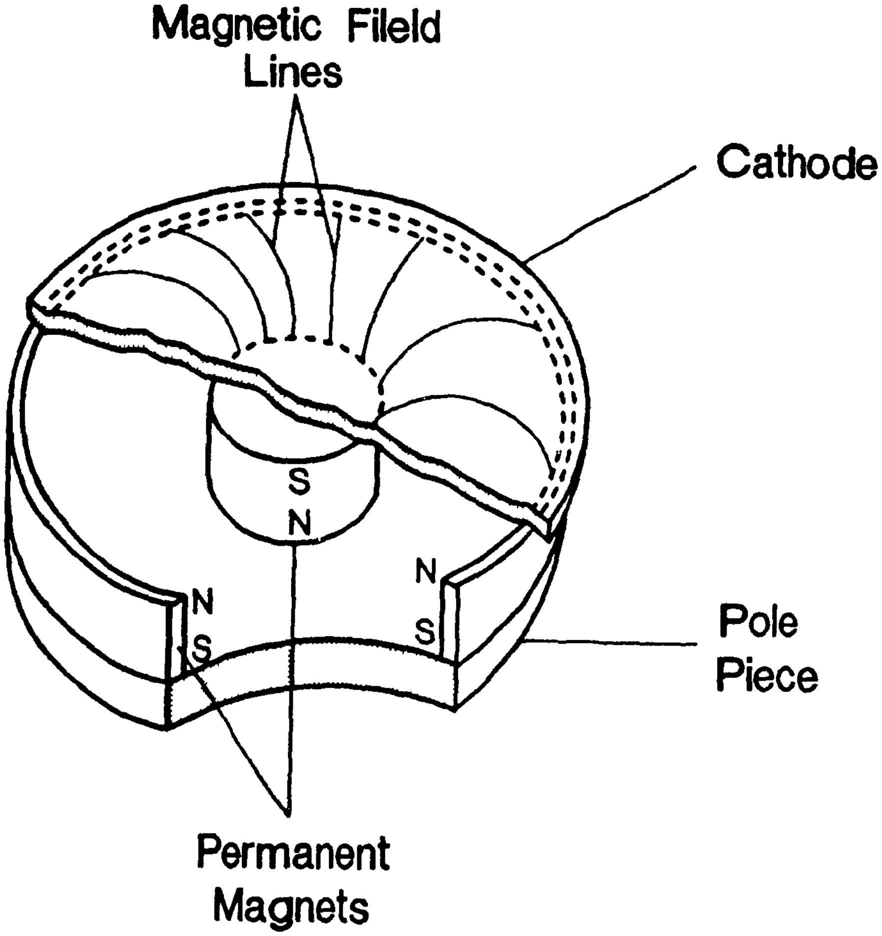

Fig. 3.2 A schematic of a planar magnetron cathode. The closed magnetic field lines can confine electrons near the target surface.

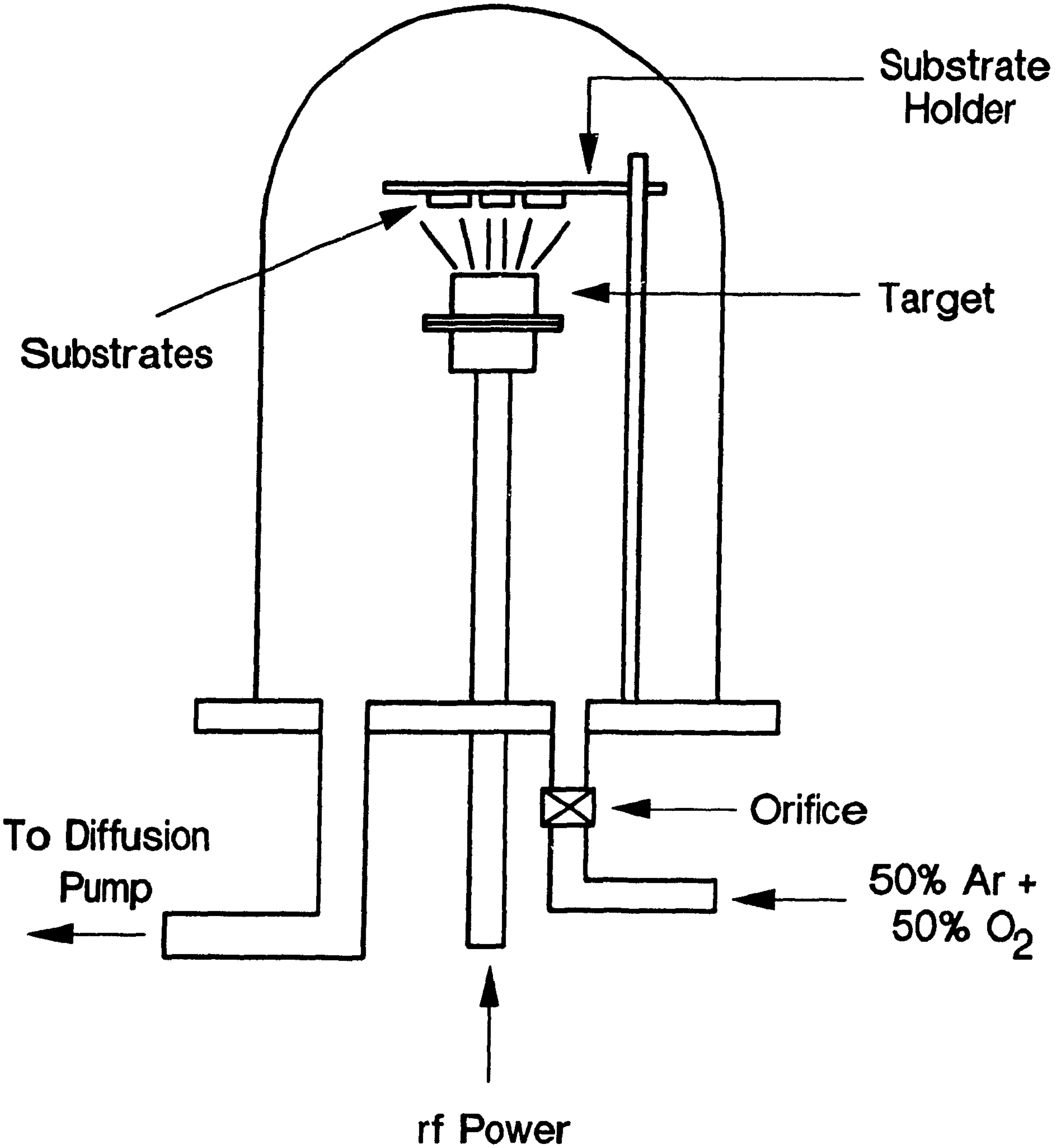

Fig. 3.3 A schematic of the rf sputtering system.

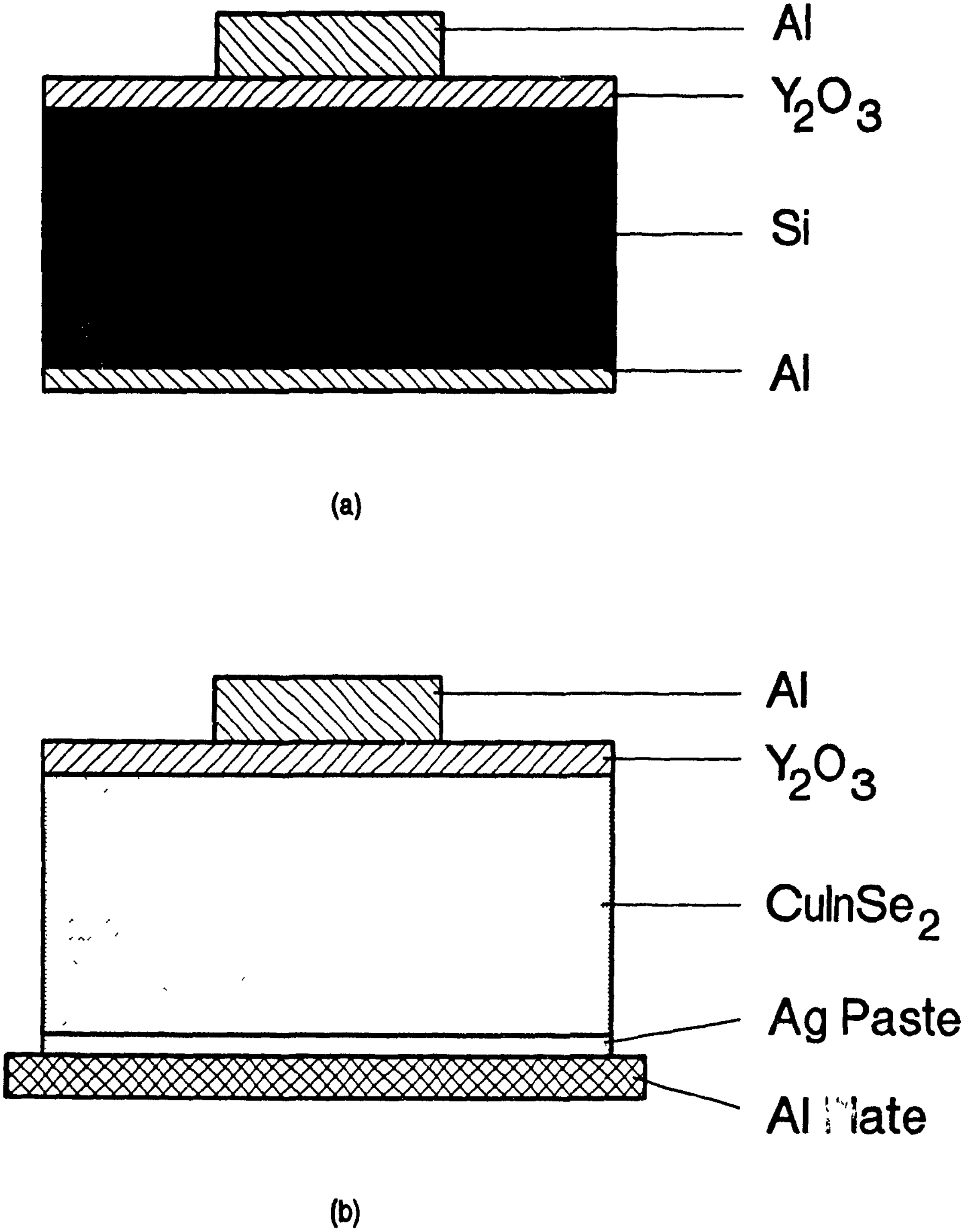

Fig. 3.4 Schematics of (a) an Al-Y_2O_3-Si capacitor and (b) an Al-Y_2O_3-$CuInSe_2$ capacitor.

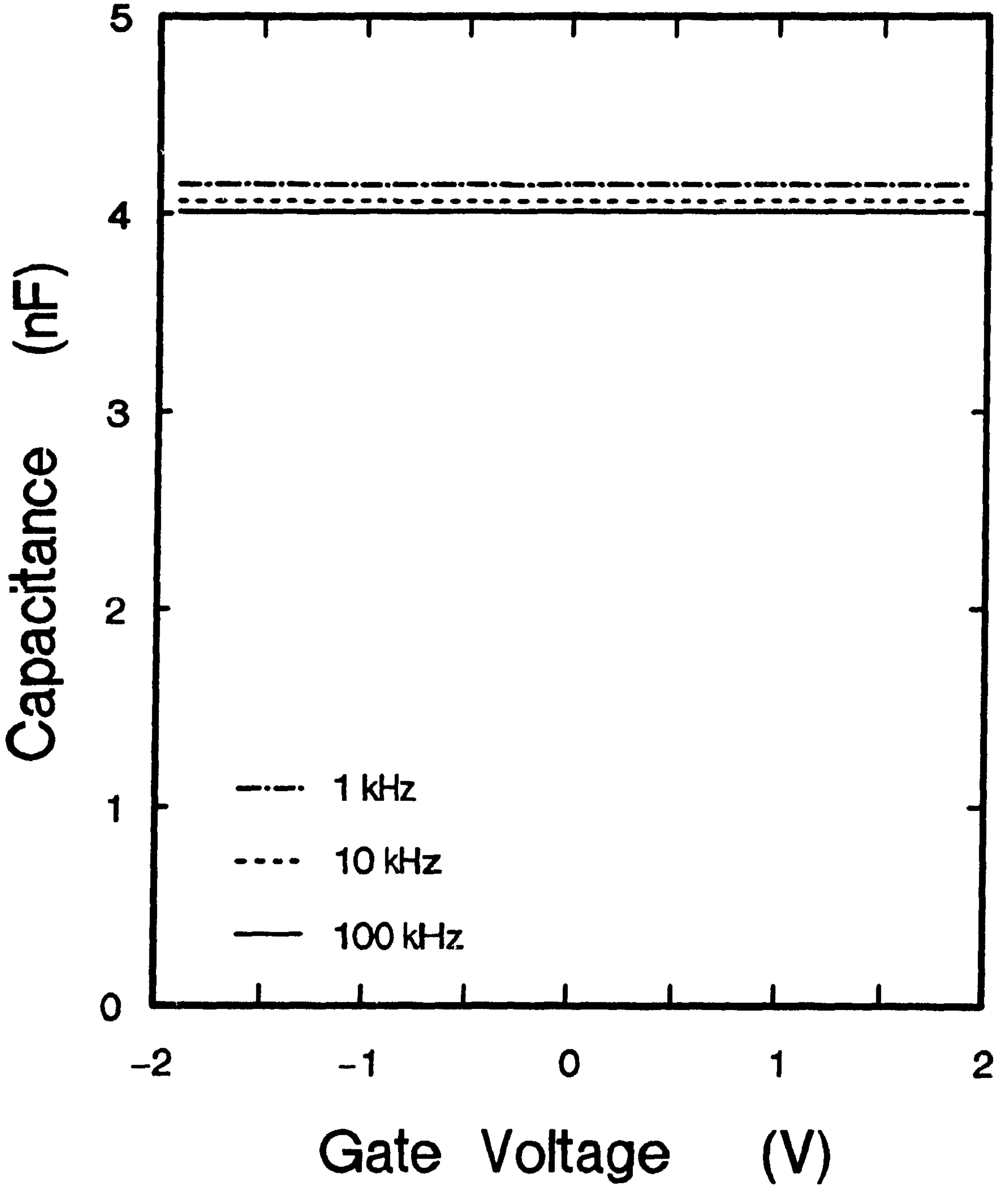

Fig. 3.5 A plot of the capacitance versus gate voltage for an $Al-Y_2O_3-Al$ capacitor at three different frequencies.

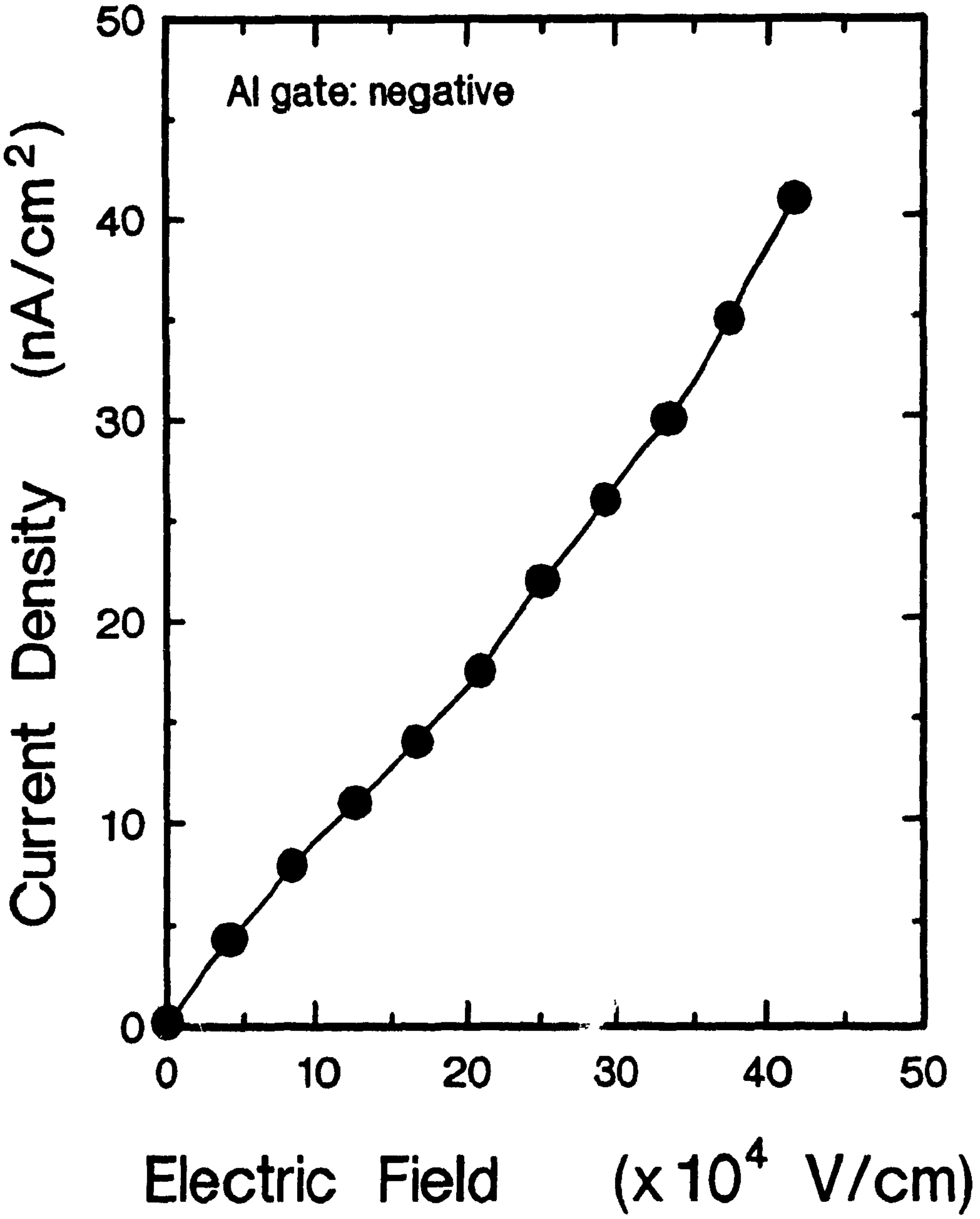

Fig 3.6 The leakage current density is plotted against the electric field across the Y_2O_3 film of an Al-Y_2O_3-Si capacitor. A negative gate voltage was used. The thickness of the Y_2O_3 film was about 1200 Å.

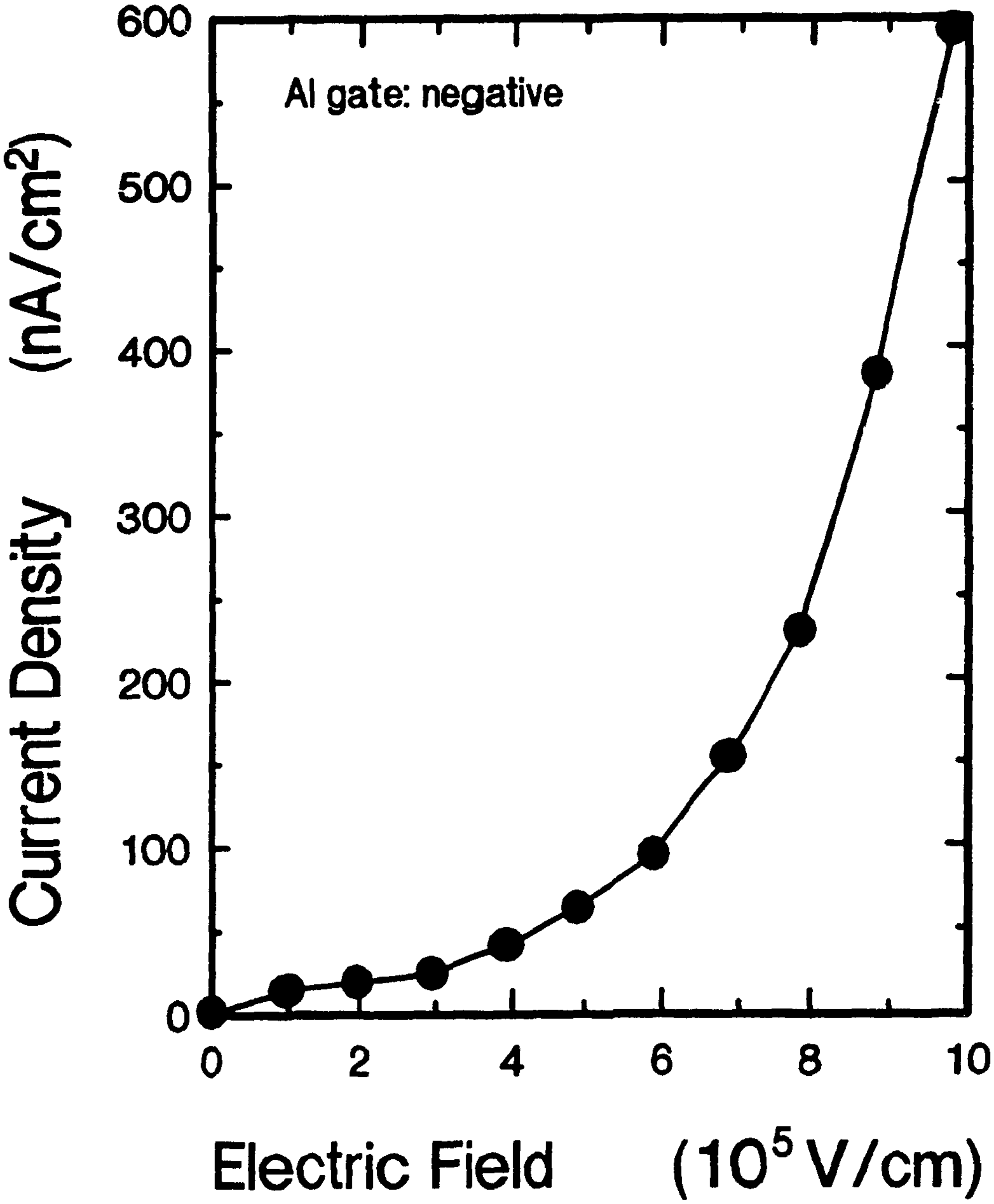

Fig. 3.7 A plot of the leakage current density as a function of electric field for another Al-Y_2O_3-Si capacitor with a Y_2O_3 film of 500 Å thick.

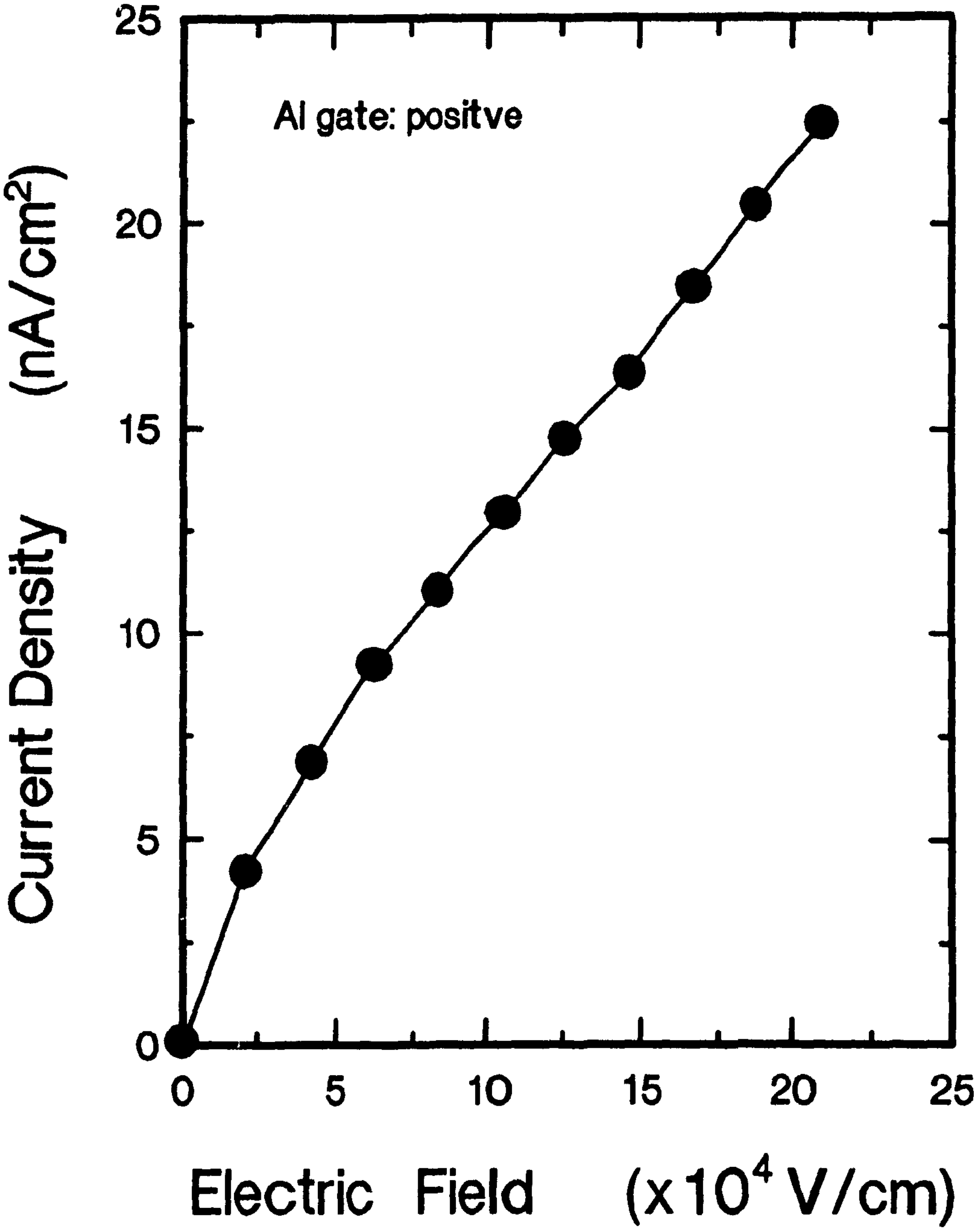

Fig. 3.8 The leakage current density is plotted as a function of electric field for a Al-Y_2O_3-Si capacitor with positive gate bias.

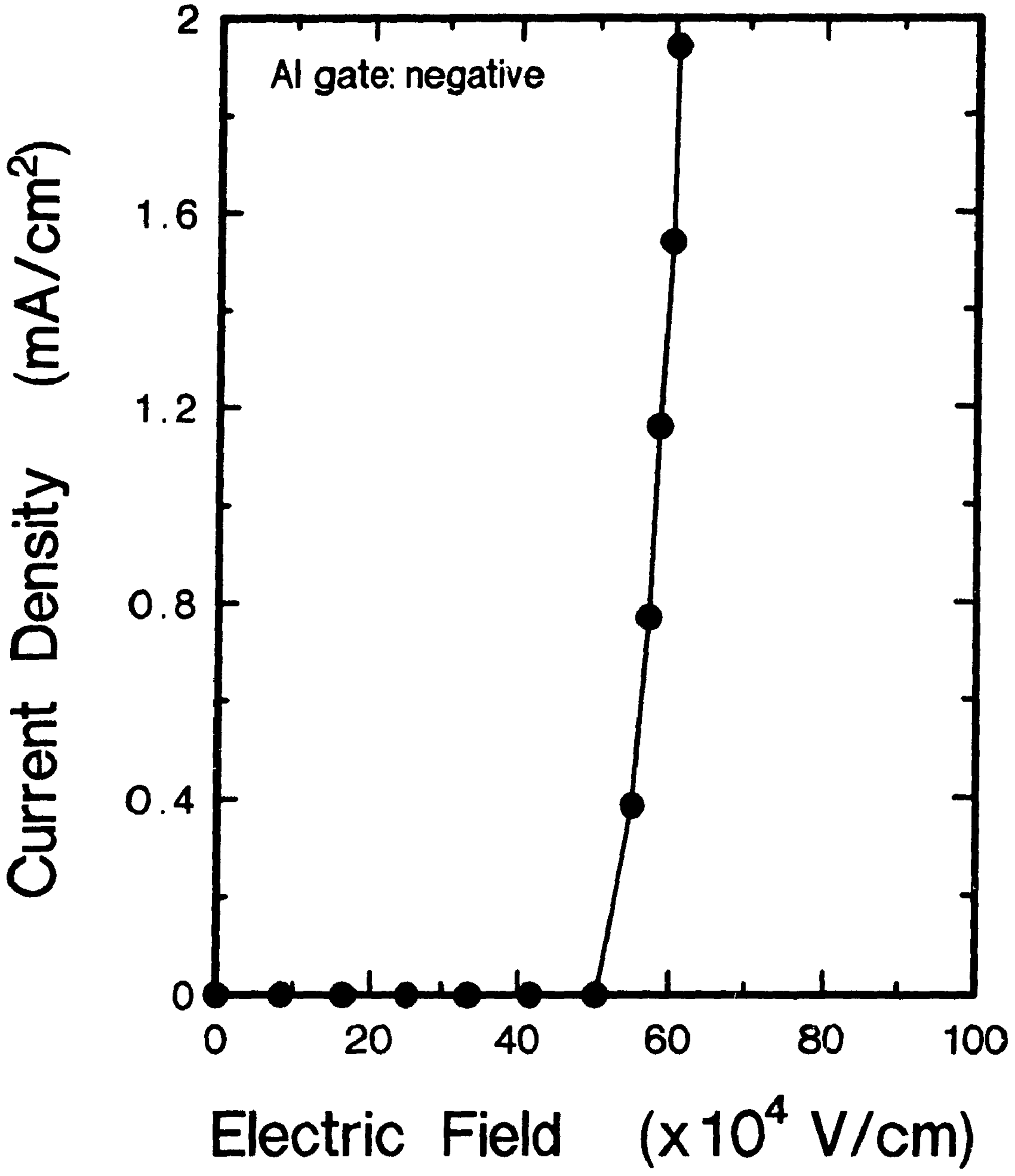

Fig. 3.9 A typical breakdown test of an Al-Y_2O_3-Si capacitor with negative gate bias. A large current passed through the insulator abruptly at a electric field of 5×10^5 V/cm.

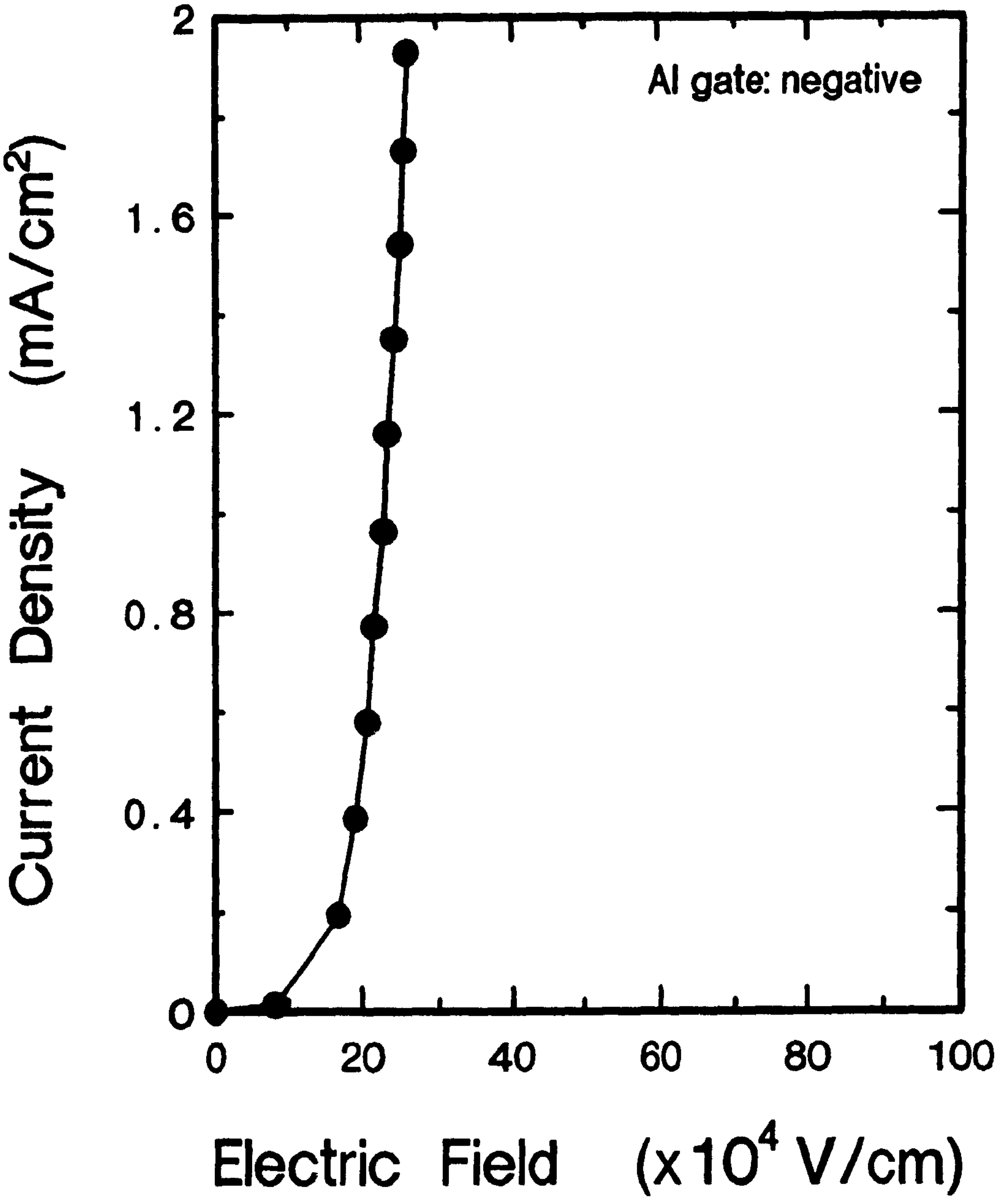

Fig. 3.10 The J-E characteristic of the capacitor shown in Fig. 3.9 after breakdown. A large current flew through the insulator even at electric field below $5x10^5$ V/cm, indicating irreversible breakdown.

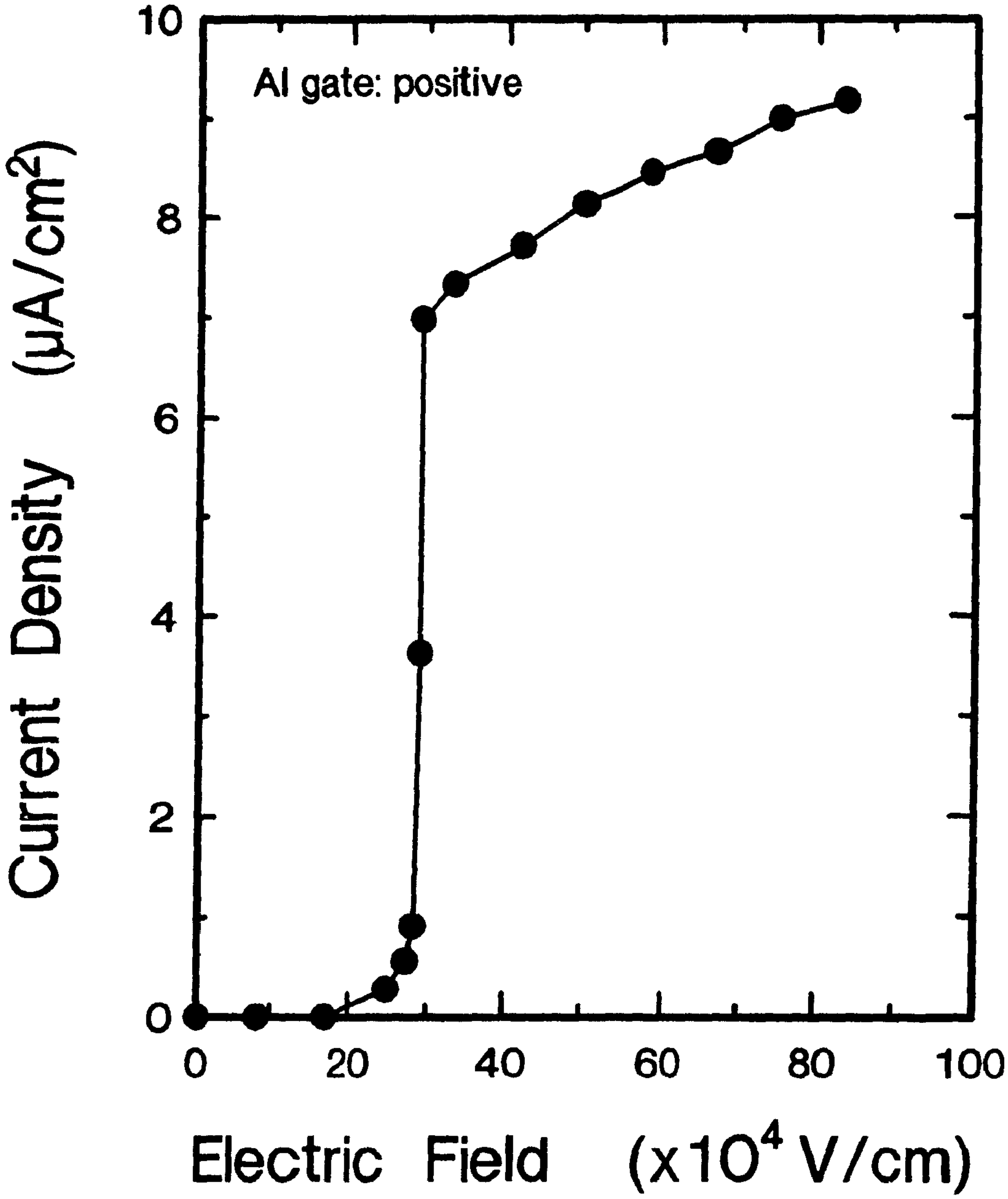

Fig. 3 11 A breakdown test of an Al-Y_2O_3-Si capacitor with positive gate bias. Current was limited by the depletion layer formed at the Si surface after breakdown.

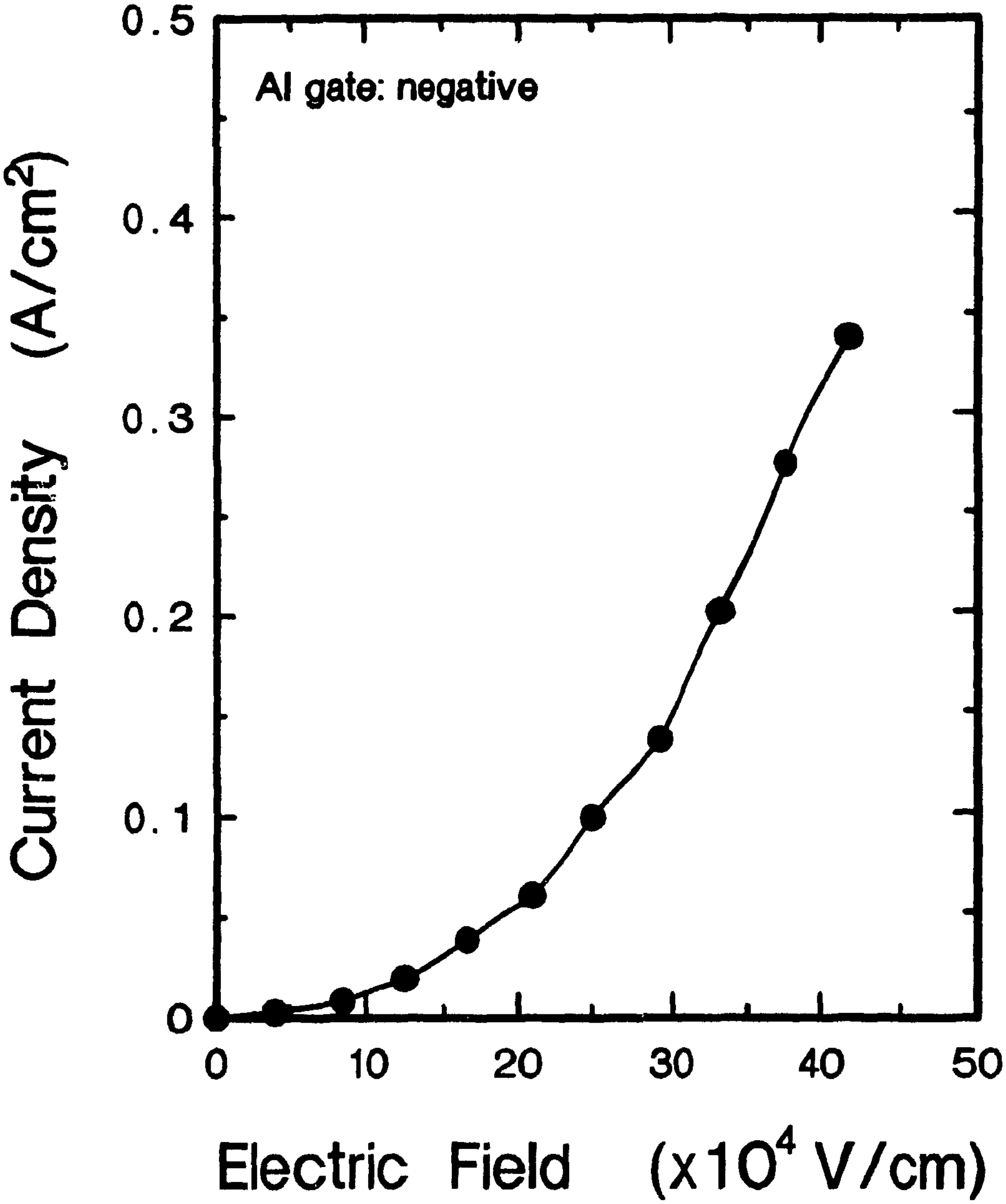

Fig. 3.12 The leakage current density is plotted against the electric field across the Y_2O_3 film in an Al-Y_2O_3-$CuInSe_2$ capacitor with negative gate bias.

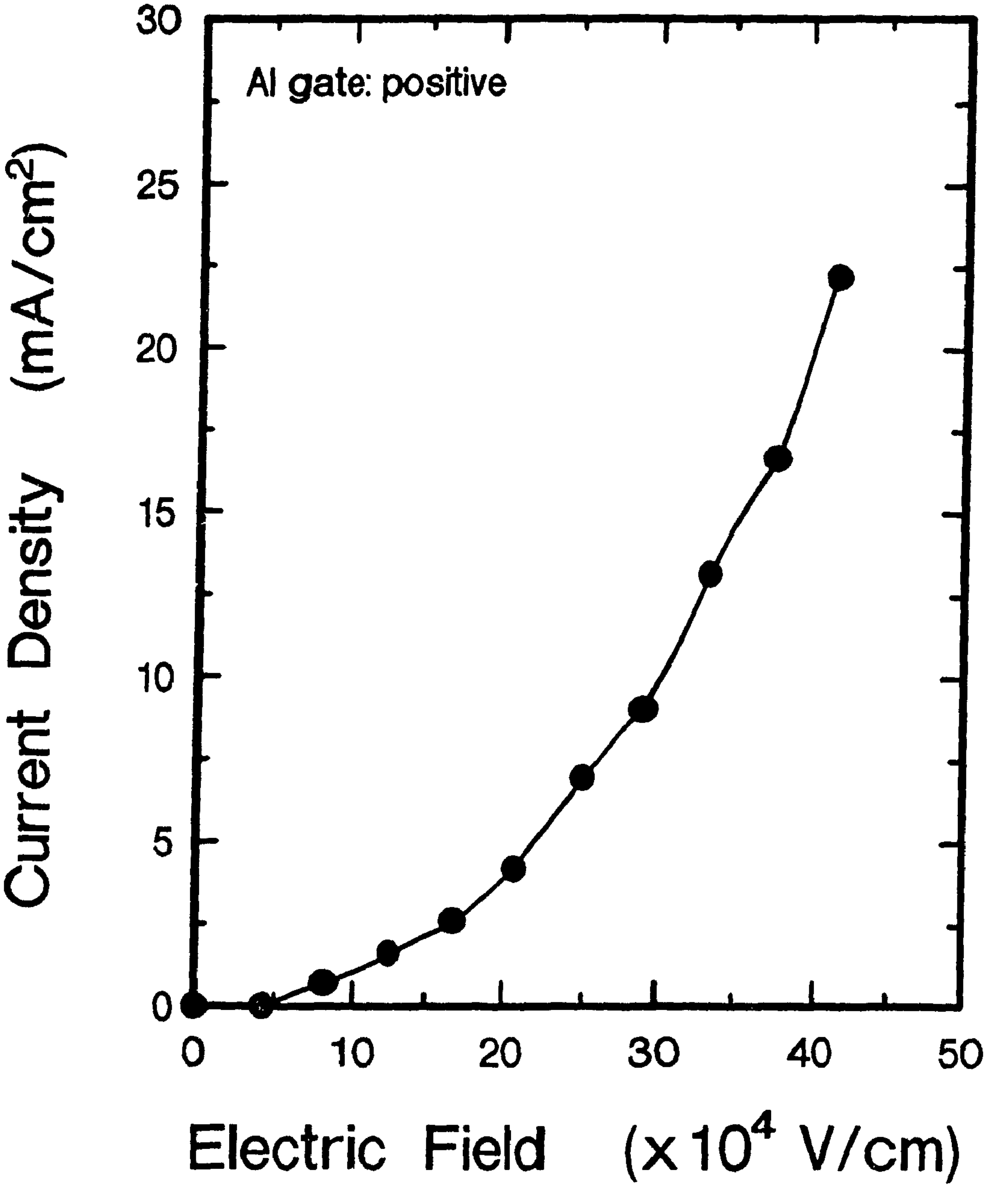

Fig. 3.13 A plot of the leakage current density versus the electric field for an Al-Y_2O_3-$CuInSe_2$ capacitor with positive gate bias.

CHAPTER 4

STUDIES OF THE C-V CHARACTERISTICS OF THE Al-Y_2O_3-Si AND Al-Y_2O_3-$CuInSe_2$ STRUCTURES

4.1 INTRODUCTION

The C-V technique has been considered as one of the most important analytical tools in the study of MIS structure. Information such as the doping profile in the semiconductor [4.1, 4.2], oxide thickness, oxide charges [4.3], and interface states [4.4, 4.5] can be derived from the C-V measurements.

The doping profile of a semiconductor can be measured by fabricating a MIS capacitor, a Schottky junction or a pn junction on the semiconductor. However, the MIS method is usually considered as a superior method than the other two because of several reasons. Firstly, it is a non-destructive method because insulating films can be deposited on semiconductors using low temperature deposition method, and the films can be removed after measurement without damaging the semiconductors. Secondly, the doping profile can be measured closer to the surface than the other two methods because of the inherent depletion layer present in the Schottky and pn junction. Thirdly, a higher doping concentration can be measured [4.6].

In the present work, the C-V characteristics of the Al-Y_2O_3-Si and Al-Y_2O_3-$CuInSe_2$ structures were examined and the feasibility of employing the C-V measurements of these structures to study the doping profile of the semiconductors was investigated. If promising results can be obtained from the C-V measurement on $CuInSe_2$ substrates, the thermal stability of the $CuInSe_2$ can be studied and the doping profile of the $CuInSe_2$ near the surface can also be determined under different annealing condition.

In this chapter, a brief theoretical background will be given for the C-V characteristics and the doping-profile determination in section 4.2. Section 4.3 will describe the C-V measurement system and technique. The results of the C-V measurements and doping-profile determinations for the Al-Y_2O_3-Si and Al-Y_2O_3-$CuInSe_2$ structures will then be presented in section 4.4.

4.2 THEORETICAL BACKGROUND

4.2.1 The MIS Capacitor

A brief background of the MIS capacitor will be given based on p-type semiconductors as to conform to the experiments. The discussion can be readily applied to n-type semiconductors with minor modifications. Fig. 4.1 illustrates a schematic of a MIS capacitor and the corresponding energy band diagram at equilibrium without any external biasing voltage. Several assumptions are made in this case. The metal work function is assumed to be the same as the work function of the semiconductor, i.e. the Fermi level, E_{FM}, of the metal is at the same energy level of the Fermi level, E_{FS}, of the semiconductor. It s also assumed that the MIS capacitor contains no oxide charges and interface states. The MIS capacitor is, therefore, in flat band condition.

Three distinct conditions can usually be distinguished for an MIS capacitor depending on the external bias. Fig. 4.2 shows the energy-band diagrams and the charge distributions of the three biasing conditions. In Fig. 4.2(a) a negative voltage (with respect to the semiconductor) is applied to the metal. A layer of electrons is then formed adjacent to the metal-insulator interface. Accordingly, holes are attracted to the vicinity of the insulator-semiconductor interface. This accumulation of holes at the semiconductor surface makes it to be heavily p-type and the MIS capacitor is considered to be biased into *accumulation.* When a small positive bias is applied to the MIS capacitor as in Fig. 4.2(b), holes are repelled from the semiconductor surface region. The surface is now depleted of holes and only the negative immobile acceptor ions are left behind in the surface region. The width of the depletion layer is dependent on the magnitude of the bias and the MIS capacitor is said to be in *depletion.* In Fig. 4.2(c) the MIS capacitor is biased into *inversion* with a large positive voltage, which exceeds the so called threshold voltage. A layer of electrons or an inversion layer is formed at the semiconductor surface in addition to the depletion layer. The depletion layer width is at its maximum value throughout the inversion region. It is because any additional charges due to an increase of the bias will be added to the inversion layer, i.e. the inversion layer shields the depletion layer from the bias in inversion. The three biasing conditions discussed above are the dc steady state conditions.

4.2.2 Capacitance-Voltage Characteristics

Depending on the dc biasing condition, an MIS capacitor will show a different capacitance-voltage characteristic. However, only the differential capacitance, but not the static capacitance, will yield useful information. In this thesis, the term capacitance always refers to the differential capacitance. To measure the differential capacitance a small ac voltage, dV_g, is superimposed on the dc gate bias. The ratio of the incremental charge, dQ_g, to dV_g gives the differential capacitance.

A plot of the capacitance as a function of gate bias is shown in Fig. 4.3 for an ideal MIS capacitor. Three distinct regions can be clearly seen. In accumulation, holes are being added to or withdrawn from the accumulation layer, which is formed due to the dc bias, at the semiconductor surface in response to the small ac signal. This is illustrated in the charge distribution diagram in Fig. 4.4(a). The response time of the holes is virtually the dielectric relaxation time (about 10^{-12} s for silicon) of the bulk semiconductor. Hence, for all the frequencies (of the ac signal) of practical concern, the accumulation capacitance is essentially frequency-independent. It is apparent that only the capacitance of the insulator, C_o, is being measured in this case. Therefore, the capacitance is essentially constant and equal to C_o in accumulation.

When the MIS capacitor is biased with a small positive dc voltage into depletion, holes are added or withdrawn at the end of the depletion layer (Fig. 4.4(b)) following the ac signal. As in the case of accumulation, the response time is the dielectric relaxation time and the capacitance should be practically frequency-independent. The measured capacitance is a series combination of the insulator capacitance, C_o, and the capacitance of the depletion layer, C_d. Since an increase of the dc bias results in an increase of the depletion width, C_d as well as the total capacitance will decrease as the dc bias increases.

With a large and positive dc bias, the MIS capacitor is biased into inversion. An inversion layer of electrons and a depletion layer with maximum width coexist at the insulator-semiconductor interface in this case. Depending on the frequency of the small ac signal, different C-V characteristics can be obtained. The response time of the inversion layer is determined by the thermal generation rate in the bulk semiconductor, i.e. by how fast the electrons can be generated. If the ac gate voltage has a frequency so high that the thermal generation rate cannot keep up with, only the widening and narrowing of the depletion layer is possible and the variation of the charge distribution is shown in Fig. 4.4(c). Since the depletion width has reached a maximum, the capacitance is at its minimum throughout inversion for a high-frequency ac small signal (see the solid line of Fig. 4.3). If the frequency is sufficiently low, usually below 100 Hz for silicon, the thermal generation is capable of producing electrons fast enough to follow the ac gate signal directly. The situation can be considered as in equilibrium so that a charge fluctuation due to the small ac gate voltage takes place only in the inversion layer (Fig. 4.4(d)). Therefore, the differential capacitance measured would again be the capacitance of the insulator, i.e. the capacitance would increase back to C_o. The dotted line in Fig. 4.3 is the C-V characteristic of the ideal MIS capacitor at low frequency.

It is worth to mention that work function difference and oxide charge would contribute to a parallel shift of the entire C-V curve. However, the shape of the curve would not be altered. On the other hand, interface states would alter the shape of the C-V curve or the slope of the C-V curve in the depletion region due to the charging and discharging of the interface states. That is, the measured capacitance would also include the interface-state capacitance.

4.2.3 Determination of the Doping Profile

Using the capacitance method,the doping profile of the semiconductor near the insulator-semiconductor interface can be determined. It is clear that the capacitance in accumulation and inversion is not strongly dependent on the doping concentration of the semiconductor. However, the capacitance in the depletion should be pertinent to the doping concentration because charges are added or removed at the edge of the depletion layer in response to the ac gate voltage. Assuming the interface states have negligible influence and using the depletion approximation, an explicit expression can be derived for the doping profile under the depletion condition. The derivation shown in the following paragraphs follows the one given by Nicollian and Brews [4.7].

Suppose an incremental charge dQ_g is added to the gate electrode of the MIS capacitor, same amount of charge would also be induced in the semiconductor by widening the depletion layer as shown in Fig. 4.4 (b). The incremental charge can be expressed as,

$$dQ_g = -qN(w)dw, \tag{4.1}$$

where N(w) is the doping concentration at w and w is the width of the depletion layer. dQ_g can also be expressed as,

$$dQ_g = C_m dV_g/A, \tag{4.2}$$

where V_g is the gate voltage, C_m is the measured capacitance and A is the area of the MIS capacitor. It is known that the capacitance of a depletion layer, C_d, is,

$$C_d = \epsilon_s \epsilon_o A/w, \tag{4.3}$$

where ϵ_s is the relative dielectric constant of the semiconductor and ϵ_o is the free space permittivity. By rearranging and differentiating equation (4.3), dw can be expressed as,

$$dw = \epsilon_s \epsilon_o A d(1/C_d). \tag{4.4}$$

Moreover, it was shown in the previous section that the measured capacitance, C_m, is a series combination of the insulator capacitance and the depletion layer capacitance in depletion whereas the insulator capacitance can be measured in accumulation. That is,

$$1/C_m = 1/C_o + 1/C_d, \tag{4.5}$$

and since C_o is not a function of gate voltage, then

$$d(1/C_m) = d(1/C_d). \tag{4.6}$$

Substitute (4.6) into (4.4), one can get

$$dw = \epsilon_s \epsilon_o A d(1/C_m). \tag{4.7}$$

Substitute (4.2) and (4.7) into (4.1), (4.1) becomes

$$C_m dV_g/A = -qN(w)\epsilon_s \epsilon_o A d(1/C_m). \tag{4.8}$$

Solving N(w) from (4.8),

$$N(w) = -\{qA^2 \epsilon_s \epsilon_o [d(1/C_m)/dV_g]/C_m\}^{-1}. \tag{4.9}$$

Equation (4.9) can be further simplified to

$$N(w) = -2\{qA^2 \epsilon_s \epsilon_o [d(1/C_m^2)/dV_g]\}^{-1}. \tag{4.10}$$

From equation (4.10), it can be seen that the doping concentration at a distance w from the insulator-semiconductor interface is proportional to the reciprocal of the slope of the curve $1/C_m^2$ against V_g, i.e. the square of the reciprocal of the measured capacitance against the applied gate voltage. The distance w can be obtained from (4.3) and (4.5) as

$$w = \epsilon_s \epsilon_o A(1/C_m - 1/C_o). \tag{4.11}$$

Using (4.10) and (4.11) the doping concentration can be determined as a function of the distance from the insulator-semiconductor interface. Since this method can only be applied in depletion, the doping profile can only be determined in a certain range of distance. It should be noted that interface states can give rise to an error in determining the doping profile because the trapping and releasing of charges by the interface states can contribute a capacitance which was ignored in the derivation of equation (4.10). In order to avoid this a high frequency, with which the interface states cannot follow, small signal should be used. The work function difference and the oxide charge, however, would not contribute an error to the doping-profile determination because they would not affect the slope of the C-V or $1/C^2$-V curve.

4.3 C-V MEASUREMENT SYSTEM AND TECHNIQUE

In determining the dielectric constant and obtaining the C-V characteristics, the differential capacitance were measured. A schematic of the C-V measurement system is shown in Fig. 4.5. The differential capacitance was measured on an HP 4274A LCR meter. The voltage across the MIS capacitor was measured on an HP 3468A multimeter. The LCR meter and the multimeter were connected to an IBM PC XT personal computer through an IEEE 488 bus. A computer program written in BASIC controlled the operation of the equipments and the data acquisition and storage.

During the measurements, the LCR meter supplied a dc bias across the two terminals connected to the device under test. This dc bias was then measured by the multimeter. The LCR meter superimposed an ac small signal voltage on top of the dc bias and the resulting displacement current was then measured to give the capacitance of the MIS capacitor at that particular dc bias. The capacitances and the dc biases were then recorded and stored in a floppy diskette in the specified voltage range.

The oscillation level or the small signal voltage used for the differential capacitance measurements was usually determined experimentally by varying the oscillation level until a certain range, in which the capacitance did not vary with a small change of the oscillation level. The oscillation level required might differ for different devices; however, the values used for the present studies were usually between 0.01-0.1 V, i.e. a few kT/q. The capacitance was measured in a parallel mode, in which a capacitance was given in parallel of a conductance. A small voltage sweep rate and a long waiting time were usually used to allow the MIS capacitor under test to come into equilibrium before measurements.

4.4 EXPERIMENTAL RESULTS

4.4.1 C-V Characteristics of Al-Y_2O_3-Si Capacitors

The C-V characteristics of a typical MYS capacitor with a Y_2O_3 film of 600 Å thick at 1 kHz, 10 kHz and 100 kHz are shown in Fig. 4.6. It can be seen that the accumulation or the oxide capacitance, which should be constant for an ideal MIS capacitor, varied with frequency. One of the possible causes of the frequency dispersion of the accumulation capacitance is a large series resistance [4.8]. However, only a series resistance of at least hundreds of ohms would have significant effect on the frequency response of the accumulation capacitance. Since Si substrates with a resistivity of 10 Ω-cm and a thickness of 360 μm were used and special care was taken to prepare the ohmic back contact, the series resistance was believed to be not more than tens of ohms. Therefore, the series resistance was believed to be not the major cause of the large frequency dispersion of the accumulation capacitance. The second possible cause is the penumbra effect [4.9]. The penumber effect arises if the metal mask is placed closely to the evaporation source during the gate metal evaporation. The heat from the source may cause the metal mask to buckle and lift off the sample. This causes a tapered edge for the gate as illustrated in Fig. 4.7. The tapered edge gives rise to a capacitance and a distributed resistance. This capacitance-resistance combination has a frequency response that does not concern the MIS capacitor. The penumbra effect can be avoided by simply placing the metal mask sufficiently far from the evaporation source. Preliminary experimental results indicated that by increasing the distance between the evaporation source or boat and the sample, the frequency dispersion of the accumulation capacitance can be reduced as shown in Fig. 4.8.

A frequency dispersion (a parallel shift of the C-V curves along the voltage axis) of the depletion capacitance can also be seen in Fig. 4.6. This may be due to the present of interface states with various time constants [4.10]. Preliminary experiments showed that the parallel shifts could be largely reduced by a heat treatment prior to the aluminum deposition at 600 ^{o}C in O_2 of the samples after the sputtering. The C-V characteristics of a heat-treated sample is shown in Fig. 4.9. This indicates that the heat treatment reduced the number of states at the Y_2O_3/Si interface. The C-V characteristics of another MIS capacitor with a thickness of 1300 Å are shown in

Fig. 4.10. These C-V curves exhibited a similar frequency dispersion as the ones shown in Fig. 4.6. However, the C-V curve measured at 1 kHz revealed a different slope in depletion indicating a large number of interface states can response to the 1-kHz ac signal in this capacitor.

It has been found that the low frequency C-V characteristic was difficult to obtain. It was because the LCR meter could not work well at frequencies below 100 Hz but the low frequency C-V characteristic is usually obtained at frequency much below 100 Hz for Si. At such a low frequency the displacement current, from which the differential capacitance is determined, is so small that a very large noise/signal ratio was obtained. The LCR meter, therefore, cannot perform accurate measurement. In order to measure low-frequency C-V characteristics, alternative methods should be used [4.11]. In Fig. 4.11 the C-V curves of a MIS capacitor at 100 Hz and 1 kHz are shown. It can be seen that the 100-Hz curve appeared to be in a transition between high-frequency and low-frequency characteristics. Another observation from this figure is that the 100-Hz curve was not smooth indicating the capacitance measurement was affected by noise.

4.4.2 Determination of Doping Profile of Si

The Si substrates were p-type and had a resistivity of 10 Ω-cm. The impurity concentration was , in this case, about 1.5-1.8x10^{15} cm^{-3}. By measuring C-V characteristics of the Al-Y_2O_3-Si structure, the doping profile of the Si near close to the Y_2O_3-Si interface were determined using equation (4.10) and (4.11). Since the slope of the $1/C^2$ vs. V_g curve should be determined in equation (4.10), numerical differentiation was carried out for this purpose. A simple computer program written in BASIC was employed for the numerical differentiation. Most of the calculation were performed in a 0.05 V voltage interval, which yielded satisfactory results in most cases in the present studies.

The doping profiles calculated for the three C-V curves in Fig. 4.10 are shown in Fig. 4.12. It can be seen that the determined doping profile consisted of three regions as marked in the diagram. However, only the middle region, from about 0.35 to 0.65 μm, contains correct information of the doping profile because this is the region corresponds to the depletion region in the C-V curves. Brews [4.1] also reported an approximate range using a similar method for determination of doping profile. The two end regions corresponds to the accumulation and the inversion and the results obtained do not correlate the doping profile of the Si substrate as can be apparently seen in the diagram. The doping concentration was calculated to be about $2x10^{15}$ /cm^3 in this range, which is a little bit higher than but close to the actual doping concentration (1.5-$1.8x10^{15}$ /cm^3) of the Si substrate. It was reported [4.1] that with the presence of interface states, even the interface states cannot response to the high-frequency C-V measurements, they will still contribute to a voltage stretch-out of the C-V curves. This will cause a higher apparent doping profile, although this effect is not large in this case. The doping concentrations obtained from the 1-kHz curve were much higher than the actual value because a large number of interface states are able to follow the ac signal at this frequency. However, most of the interface states cannot follow the ac signal at 10 kHz and 100 kHz resulting in more accurate results for doping-profile determination.

The doping profile determined from the 1-kHz C-V curve shown in Fig. 4.11 is depicted in Fig. 4.13. The impurity profile obtained was uniform in the region measured and has a value of about $1.6\text{x}10^{15}$ cm^{-3}, which is very much in agreement with the actual value. This indicates that most of the interface states have a response time longer that a period of the 1-kHz ac signal in this capacitor. The interface states have also a negligible stretch out effect, indicating a low density of interface states. The doping profiles determined were uniform in the present cases, it should be noted that this method is capable of measuring point-by-point impurity concentration, i.e. a nonuniform impurity profile can also be determined.

From the preceding results, it is apparent that the doping profile can be determined quite accurately by the simple method described above. Further improvements on the method have been reported. Brews [4.1] reported a method to correct the stretch-out effect of the interface states. Lin et al. [4.12] demonstrated the possibility of the determination of doping profile right from the insulator-semiconductor interface to deeper into the semiconductor than the present method. However, these methods require more complicated techniques such as quasi-static C-V measurements [4.5] and Pulsed C-V measurements [4.6], which were not readily available for the present studies. However, more work will be done using these techniques in our laboratory.

If the doping profile of $CuInSe_2$ can also be determined by this simple technique, information on the thermal stability of $CuInSe_2$ and annealing effect can then be obtained by studying the point-by-point variation of the doping concentration near the $CuInSe_2$ surfaces.

4.4.3 C-V Characteristics of Al-Y_2O_3-$CuInSe_2$ Capacitors

The capacitance-voltage characteristics of the MYC capacitors were also obtained. As mentioned in the previous chapter, all the MYC capacitors exhibited a large leakage current, which would probably affect the accuracy of the C-V measurements. Fig. 4.14 shows a plot of the capacitance as a function of the gate voltage for a typical MYC capacitor with a thickness of about 1200 Å at four different frequencies. The curves have the general shape of an ideal MIS C-V curve. However, several differences are also apparent. It can be seen that the capacitance in the accumulation is strongly frequency dependent and is skewed. This is due to the large leakage of the capacitor. Furthermore, the accumulation capacitance values are much higher than the ideal value (the oxide capacitance), which is about 0.4 nF, except the 1-MHz curve. Since the dc leakage can be considered as a resistance in parallel to the oxide capacitance, this parallel resistance would have a smaller effect at higher frequency as can be seen from the figure. In fact a leakage current that is not too large usually has a negligible effect on high-frequency C-V measurements. Therefore, it is not surprising to find out that the 1-MHz curve agrees more closely to the theoretical values.

This is further illustrated by the C-V curves shown in Fig. 4.15 for another MYC capacitor measured at 1 MHz and 100 kHz. The dc leakage has a less apparent effect on the C-V measurements at 1 MHz than at 100 kHz. The oxide capacitance is about 0.5 nF in this capacitor. In fact the C-V measurements at higher frequencies were more stable than at lower frequencies.

The slope of the curves in depletion was also dependent on the frequency. A steeper slope was obtained for a lower frequency. The large leakage current appeared to increase the slope of the capacitors especially at lower frequencies. This is also true for those Al-Y_2O_3-Si capacitors with a large leakage current.

The capacitances measured in inversion were also higher at lower frequencies as in the case in accumulation. In fact this is true whenever a capacitor is connected in parallel to a small resistance.

4.4.4 Determination of Doping Profile of $CuInSe_2$

It was shown in the previous section that at higher frequencies, more accurate C-V measurements can be obtained for the MYC capacitors. Therefore, doping profile was determined for the MYC capacitors mostly from the high-frequency (1 MHz or 100 kHz) C-V curves. Fig. 4.16 depicts a plot of the doping profiles determined from the 1-MHz and 100-kHz C-V curves shown in Fig. 4.14. The doping concentration obtained from the 1-MHz curve was about 2×10^{15} cm^{-3}, which is lower than the actual doping concentration (about 4.5×10^{16} cm^{-3} as determined by Hall effect measurements), in the range between 0.4 μm to 0.5 μm. This is due to a steeper slope caused by the large leakage of the MYC capacitor. Accurate doping profile can neither be deduced from the 100-kHz curve as can be seen from the diagram. It is apparent that the large leakage current restricted an accurate determination of doping profile from the C-V measurements even at such high frequencies.

As mentioned in the previous chapter, the large leakage was due to the difficulty in preparing clean and smooth $CuInSe_2$ surface for the fabrication of MYC capacitors. Therefore, it is important to carry out more work on the surface preparation of $CuInSe_2$ in order to study $CuInSe_2$ with the MIS structure.

4.5 CONCLUSIONS

The C-V characteristics of the MYS and MYC capacitors have been measured. The accumulation capacitance of the MYS capacitors exhibited a frequency dispersion which can be attributed to the penumbra effect. A frequency dispersion was also observed for the depletion capacitances. This was probably caused by the interface states with different time constants. The doping profiles determined for the Si substrates of the MYC capacitors agreed quite well to the actual doping profile. It is, therefore, feasible to use the sputtered Y_2O_3 films in MIS structure for the determination of the doping profile of a semiconductor.

The large leakage current of the MYC capacitors restricted the accuracy of measurements of C-V characteristics. However, at 1 MHz the C-V measurements agreed better with the theoretical values. At lower frequencies, the accumulation capacitances were much larger than the oxide capacitance and the C-V curves were skewed. The large leakage also caused the C-V curves to have steeper slopes in depletion resulting in smaller doping concentrations determined from the C-V curves. The doping concentrations obtained in this case were about an order of magnitude lower than the actual values. Since it was found that the Y_2O_3 films exhibited good insulating properties on Si substrates, the large leakages of the MYC capacitors were believed to be due to the difficulty in the surface preparation of $CuInSe_2$. It is, therefore, necessary to carry out more work on the surface preparation of $CuInSe_2$.

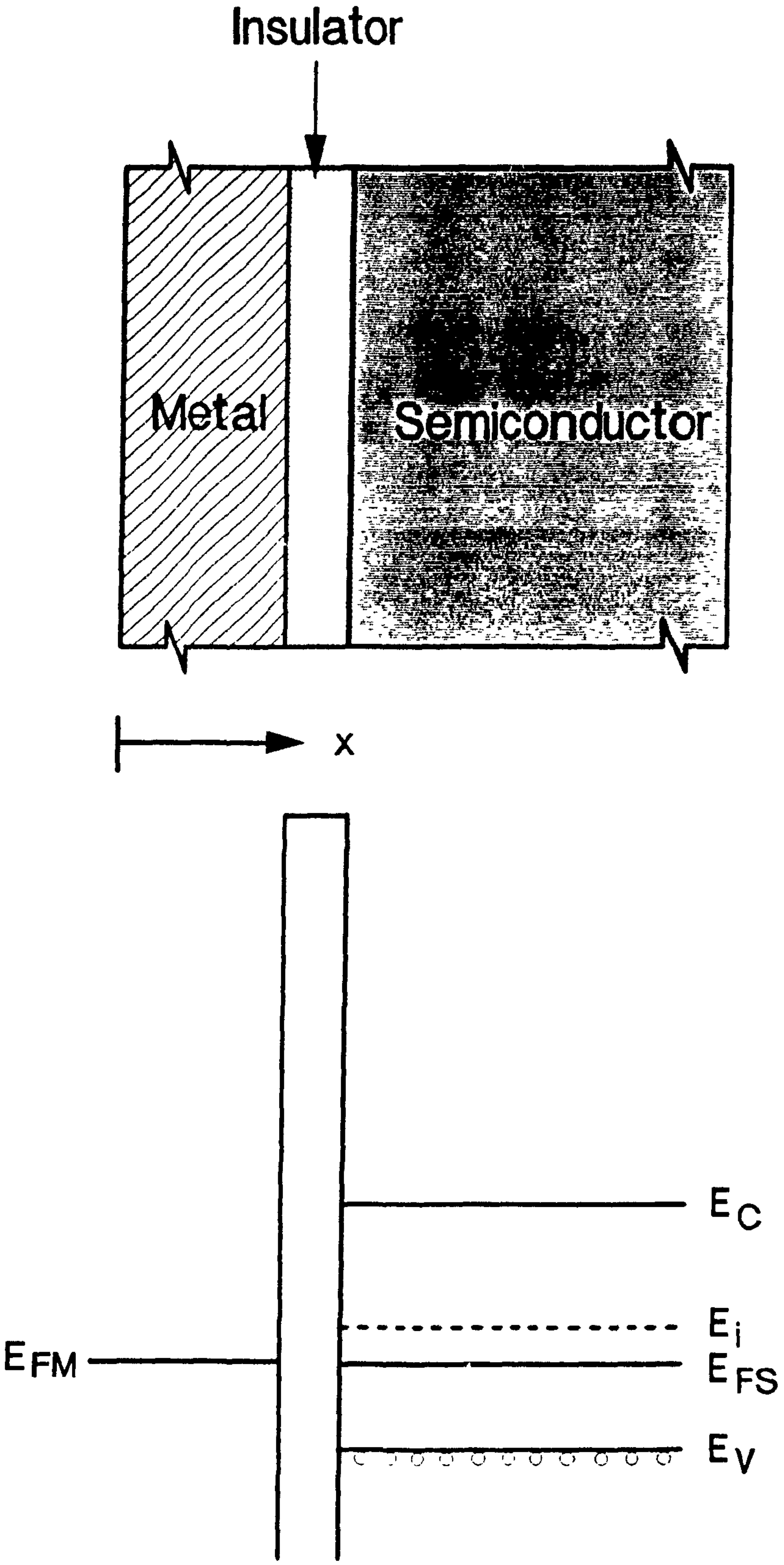

Fig. 4.1 A schematic of a MIS capacitor and the corresponding energy band diagram.

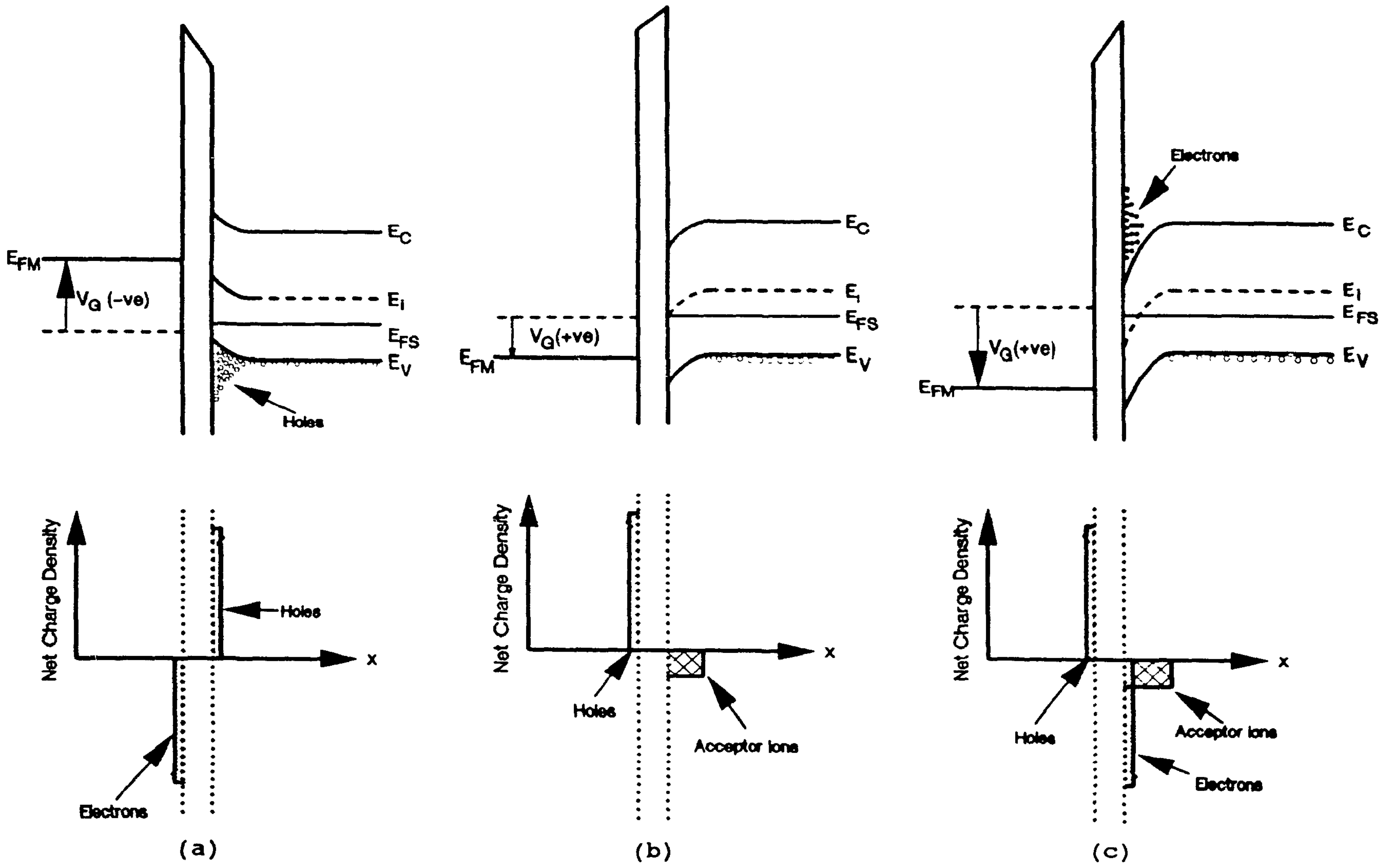

Fig. 4.2 The energy-band diagrams and the charge distribution for (a) accumulation, (b) depletion and (c) inversion.

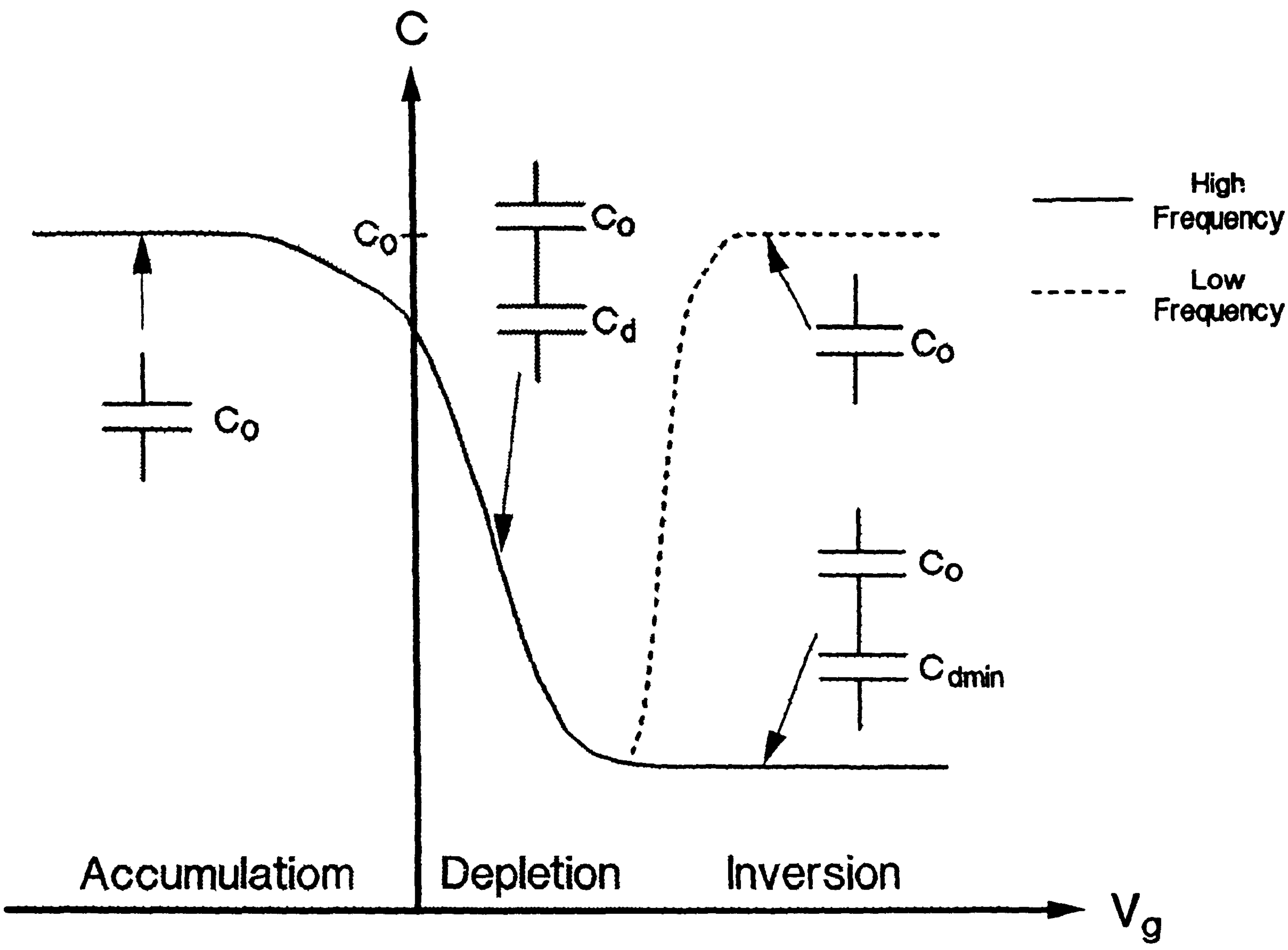

Fig. 4.3 The C-V characteristic of an ideal MIS capacitor.

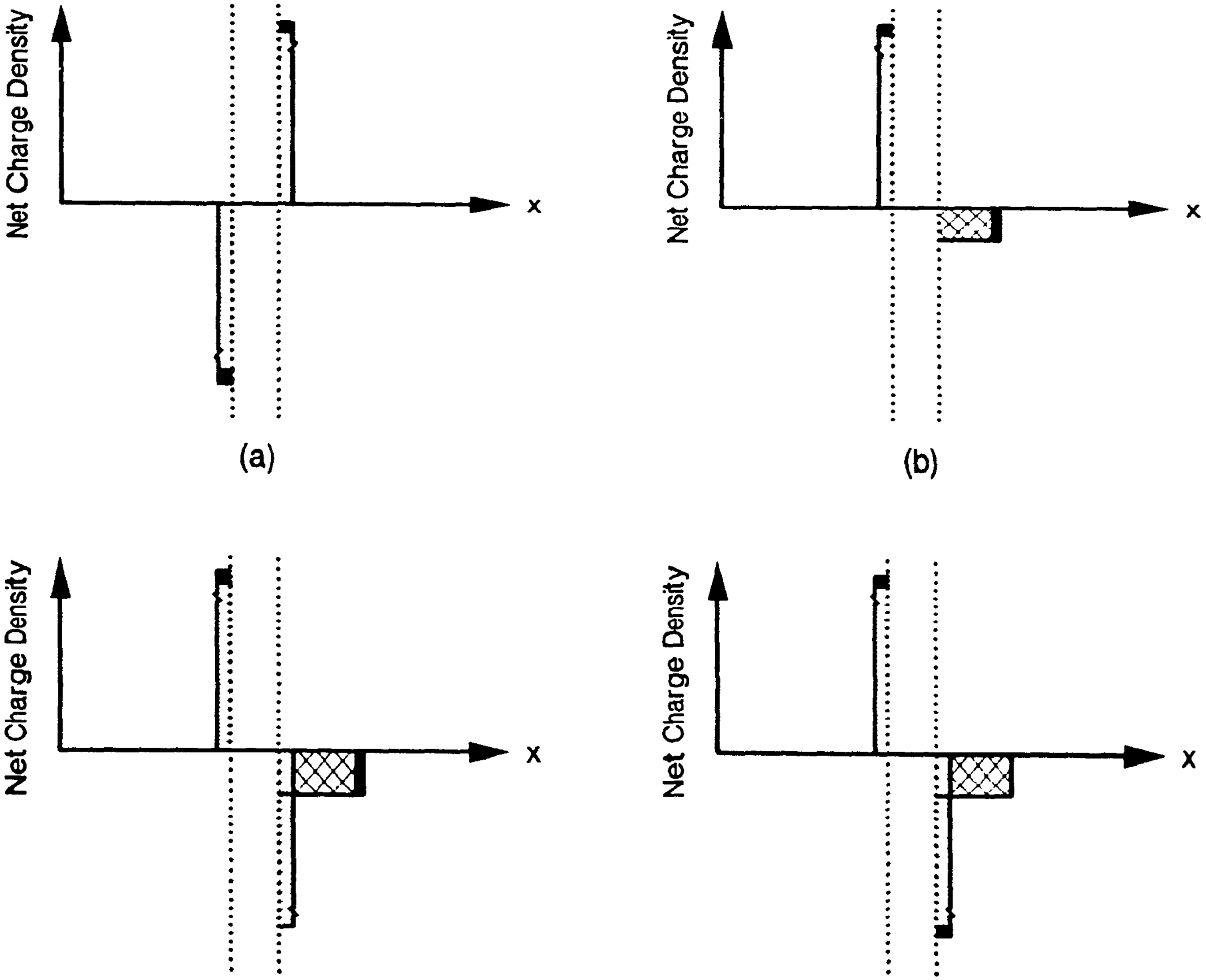

(a) (b)

(c) (d)

Fig. 4.4 Diagrams showing the charge fluctuations in response to the ac gate voltage in (a) accumulation, (b) depletion, (c) inversion at high frequency and (d) inversion at low frequency. The shaded areas are the charge fluctuations.

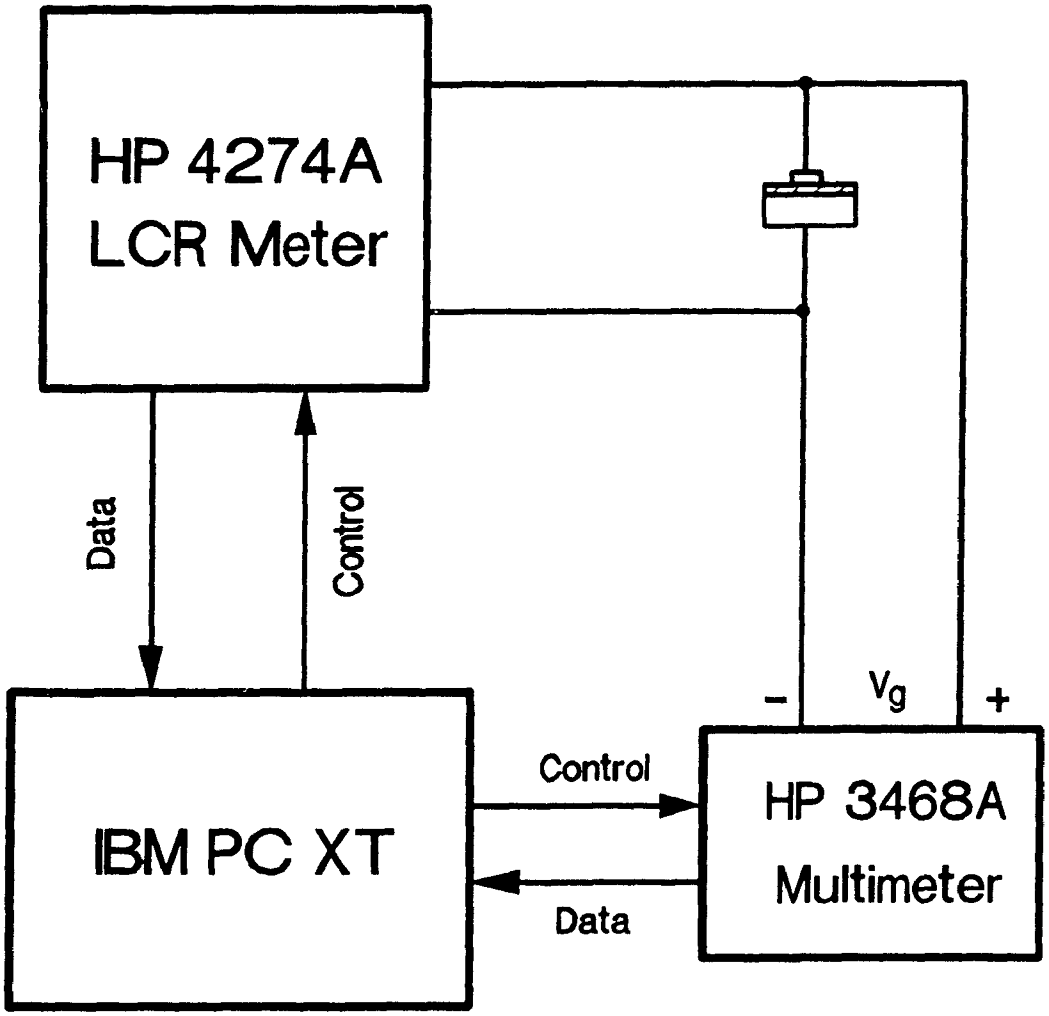

Fig. 4.5 The C-V measurement system.

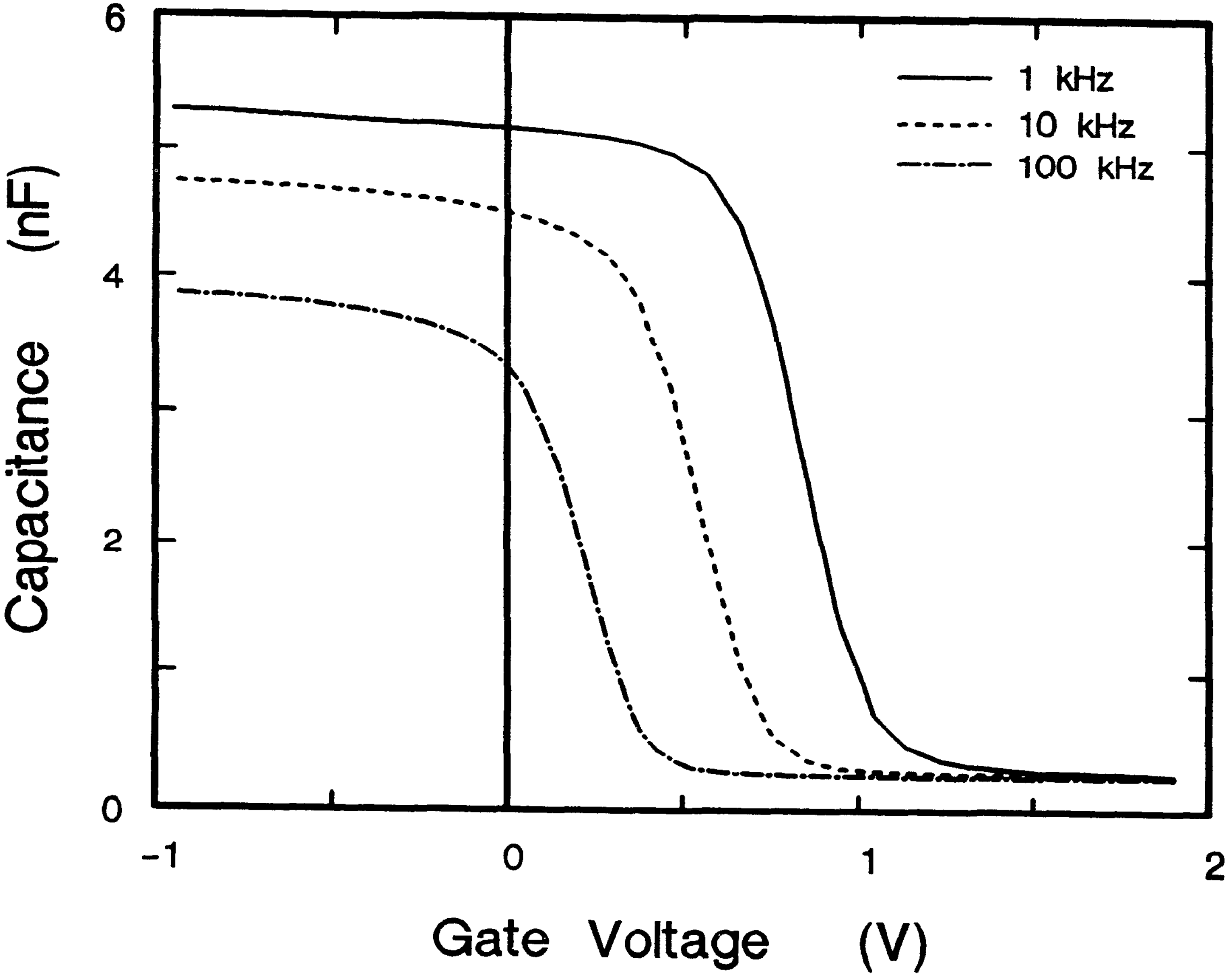

Fig. 4.6 The C-V characteristics of a typical Al-Y_2O_3-Si capacitor. The Y_2O_3 film was about 600 Å thick.

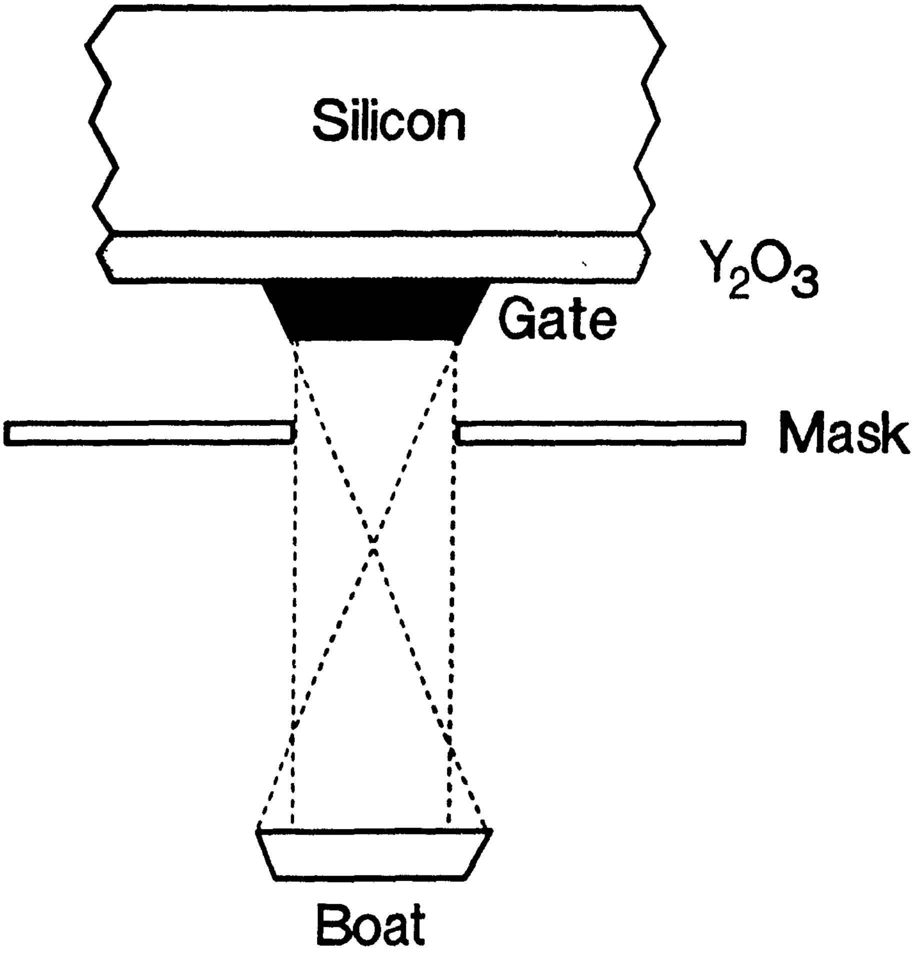

Fig. 4.7 A figure showing the formation of a metal gate with tapered edge due to the lift-off of the mask.

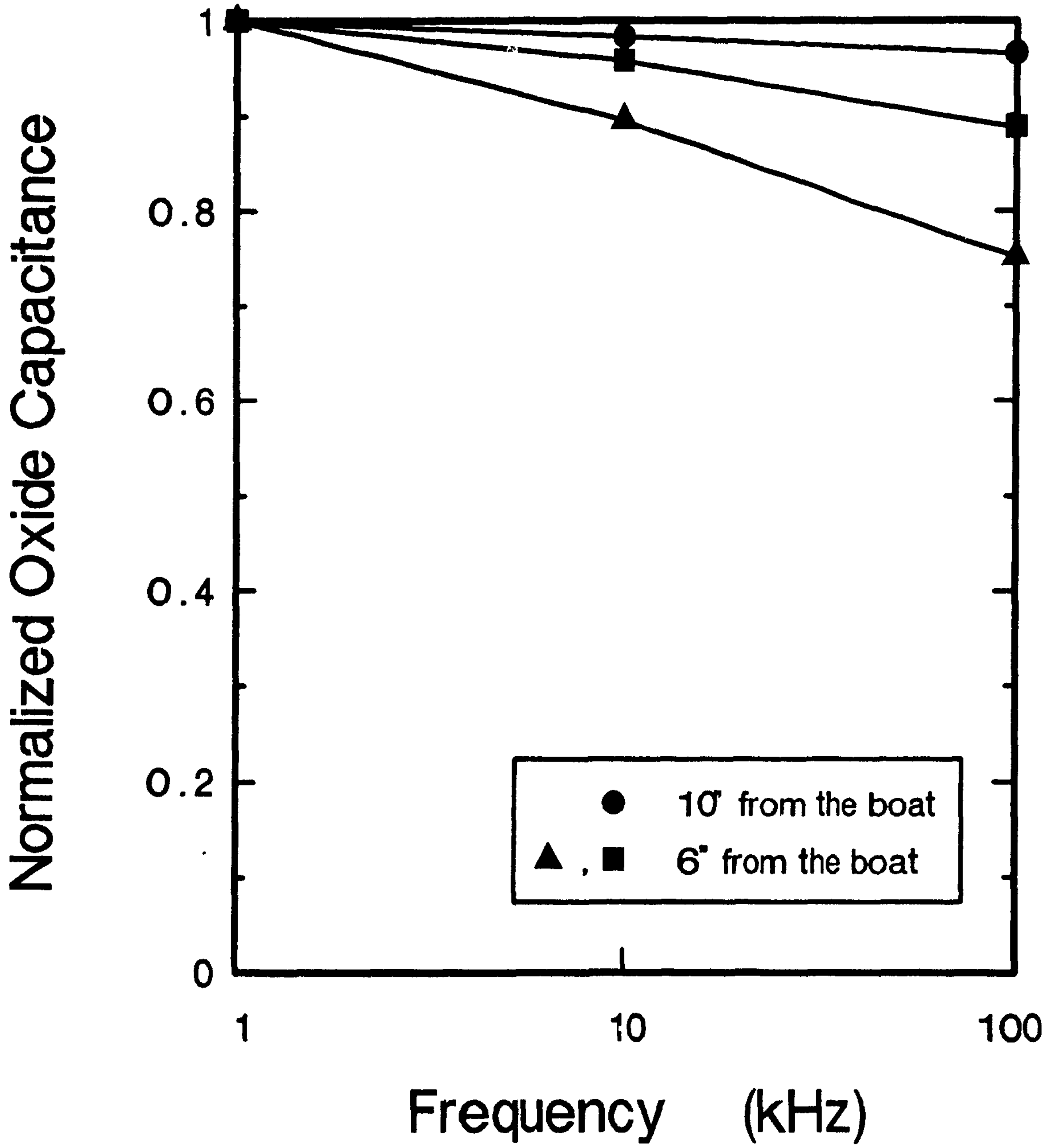

Fig. 4.8 A figure showing a reduction of the frequency dispersion of the accumulation capacitance by increasing the distance between the evaporation source and the sample from 6" to 10".

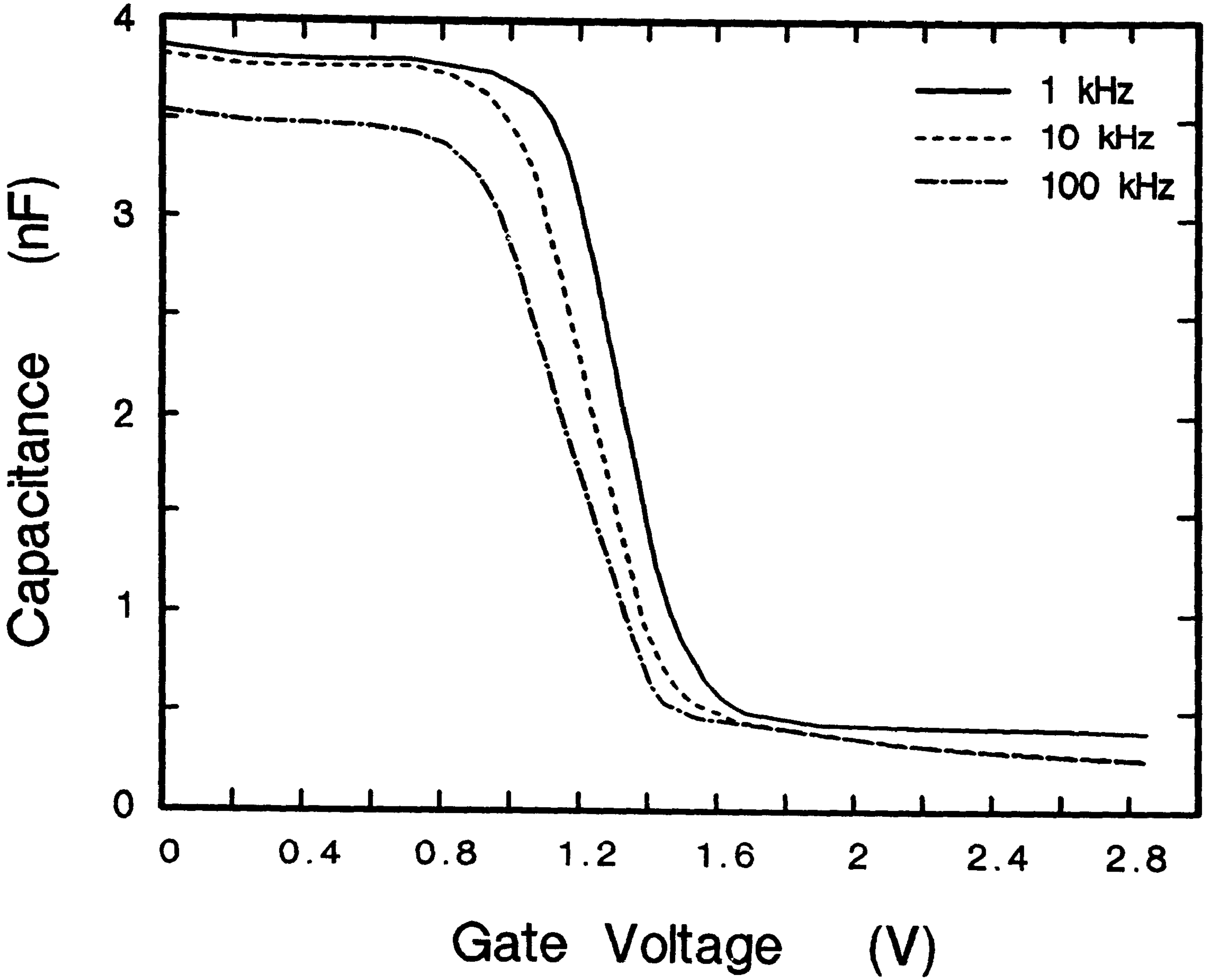

Fig. 4.9 The C-V characteristics of a heat-treated Al-Y_2O_3-Si capacitor. A smaller frequency dispersion in depletion can be seen.

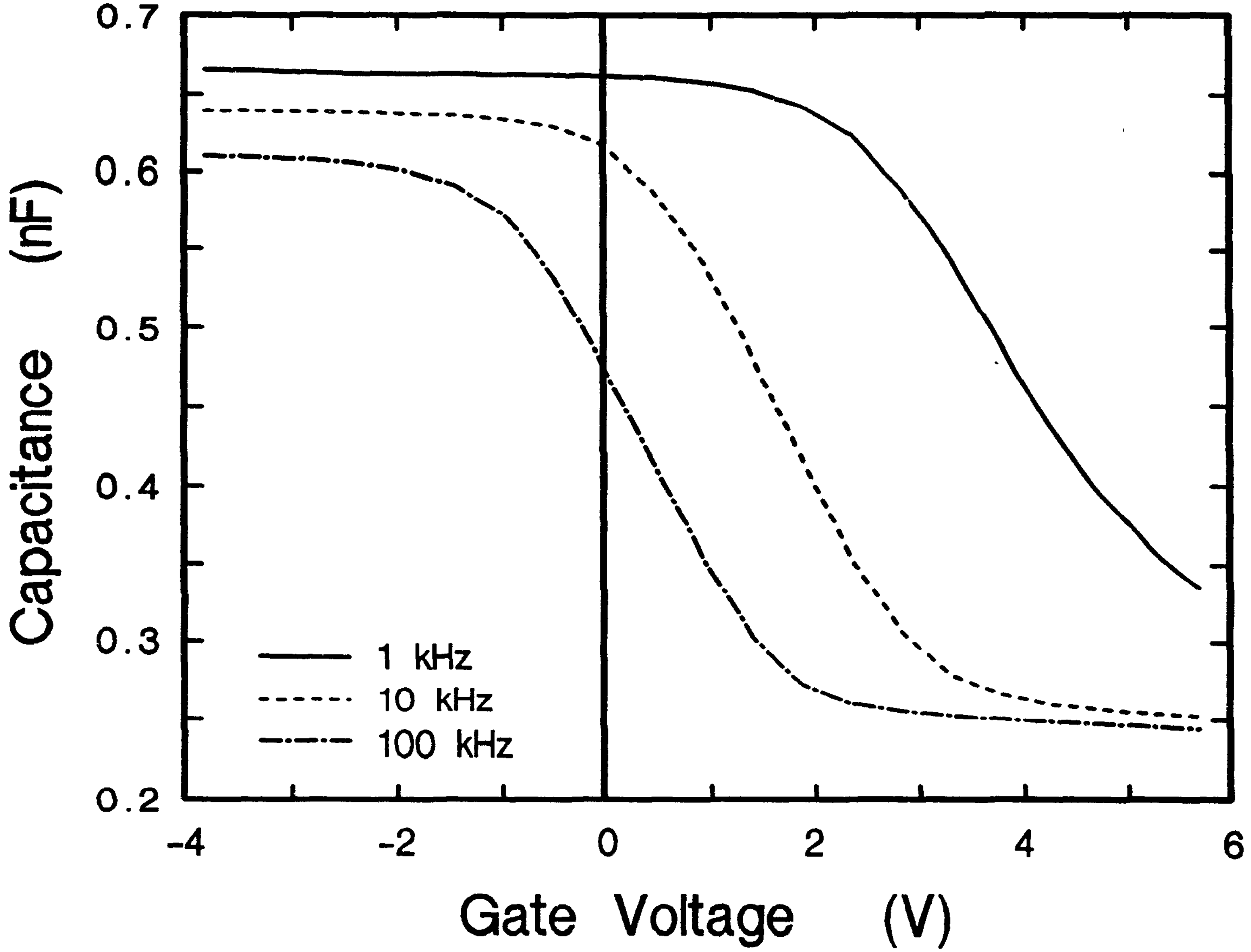

Fig. 4.10 The C-V characteristics of another Al-Y_2O_3-Si capacitor with a Y_2O_3 thickness of about 1300 Å.

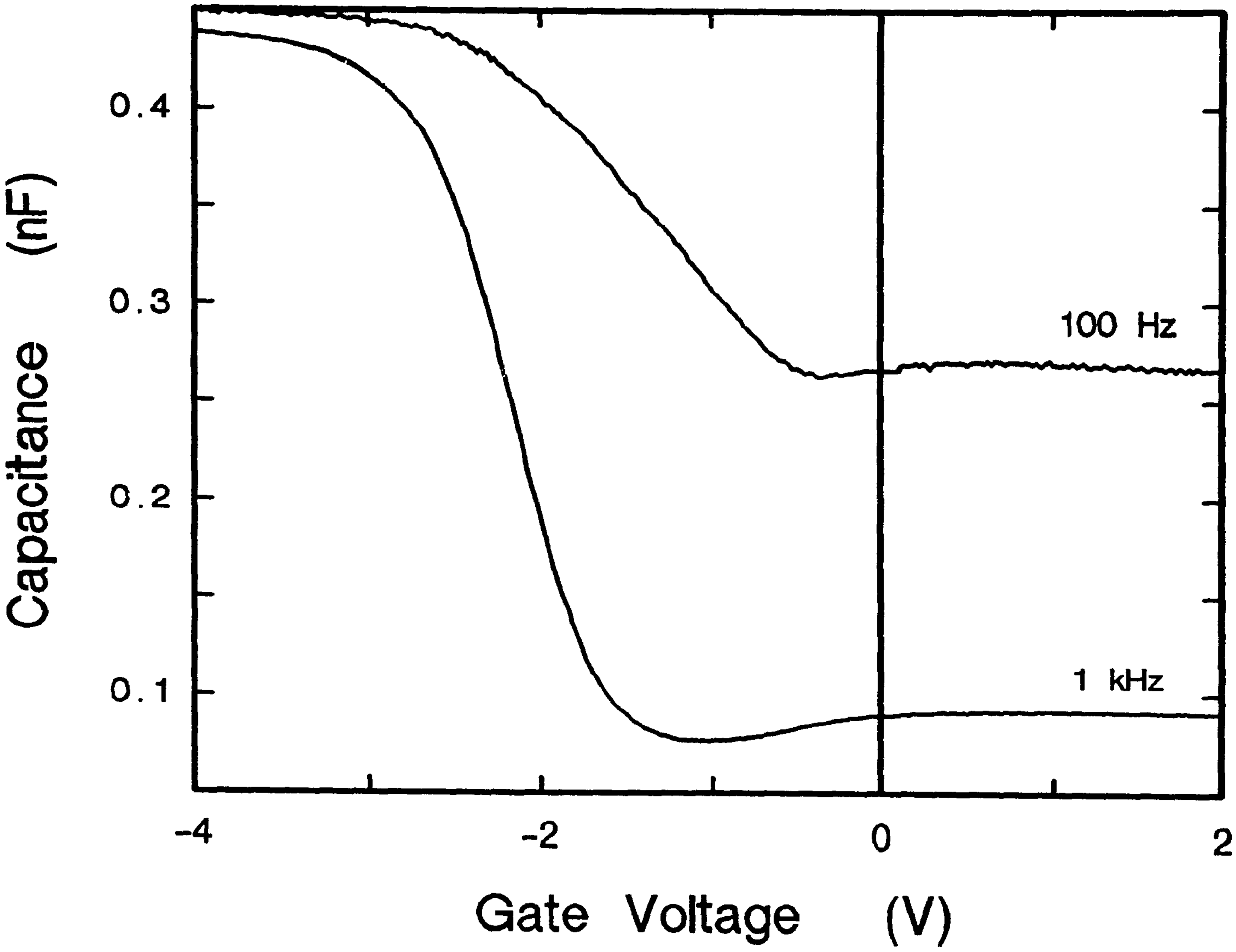

Fig. 4.11 An Al-Y_2O_3-Si capacitor showing a transition between high-frequency and low-frequency characteristic at 100 kHz. It can be seen that the C-V measurements were affected by noise at 100 kHz.

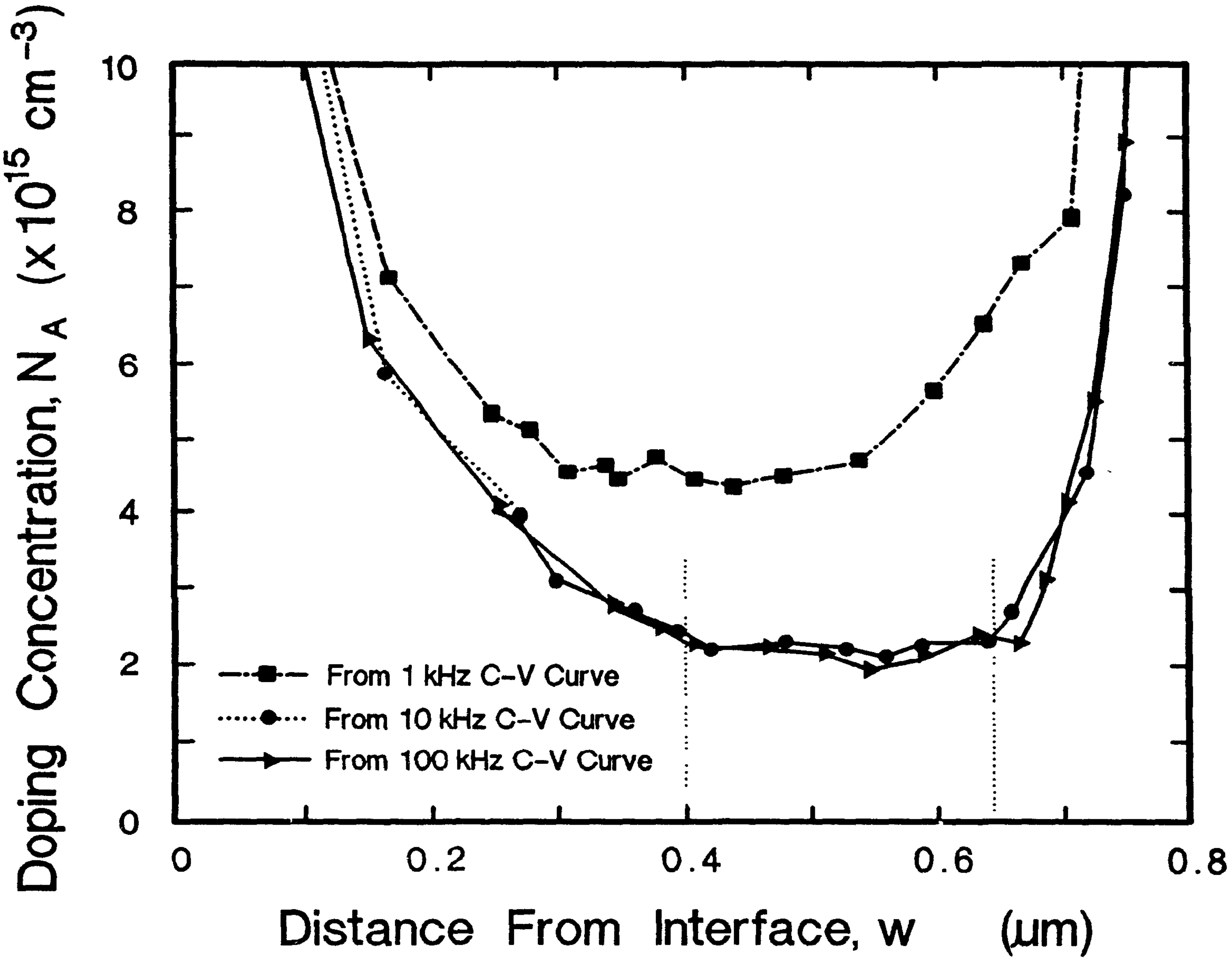

Fig. 4.12 Doping profile of the Si determined from the C-V curves shown in Fig. 4.10.

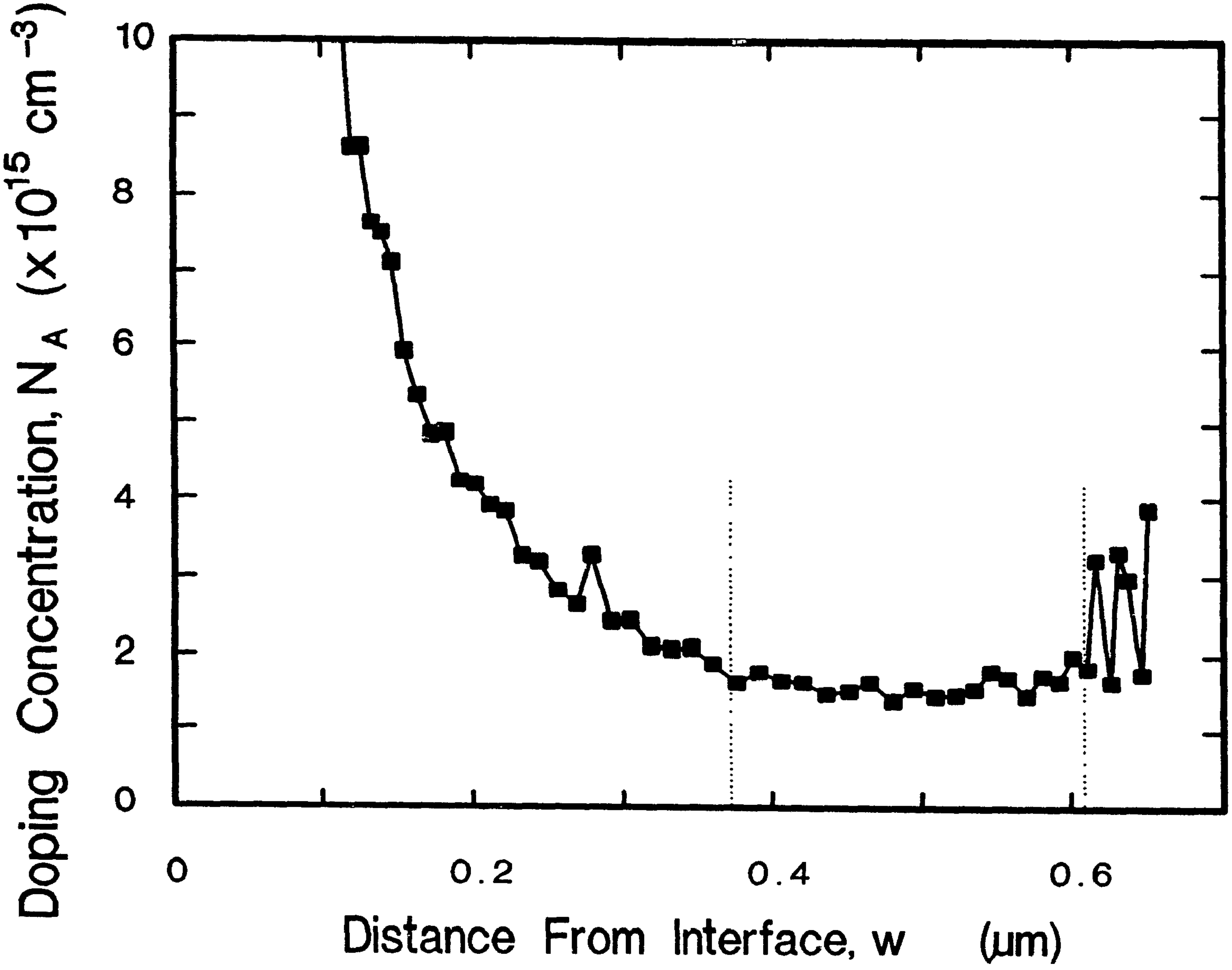

Fig. 4.13 Doping profile of the Si determined from the 1-kHz C-V curve shown in Fig. 4.11.

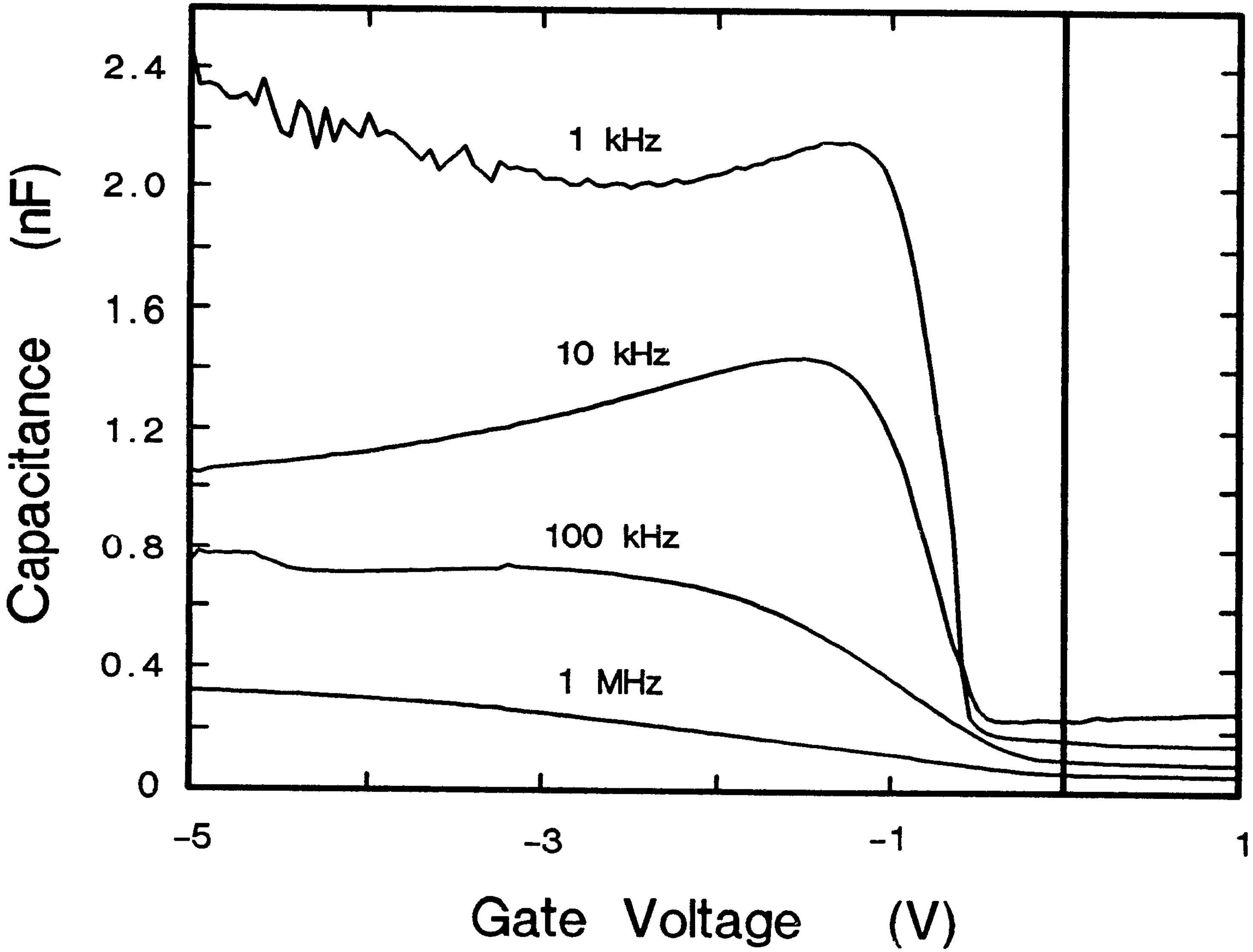

Fig. 4.14 The C-V characteristics of an Al-Y_2O_3-$CuInSe_2$ capacitor at four different frequencies. The thickness of the Y_2O_3 film was about 1200 Å.

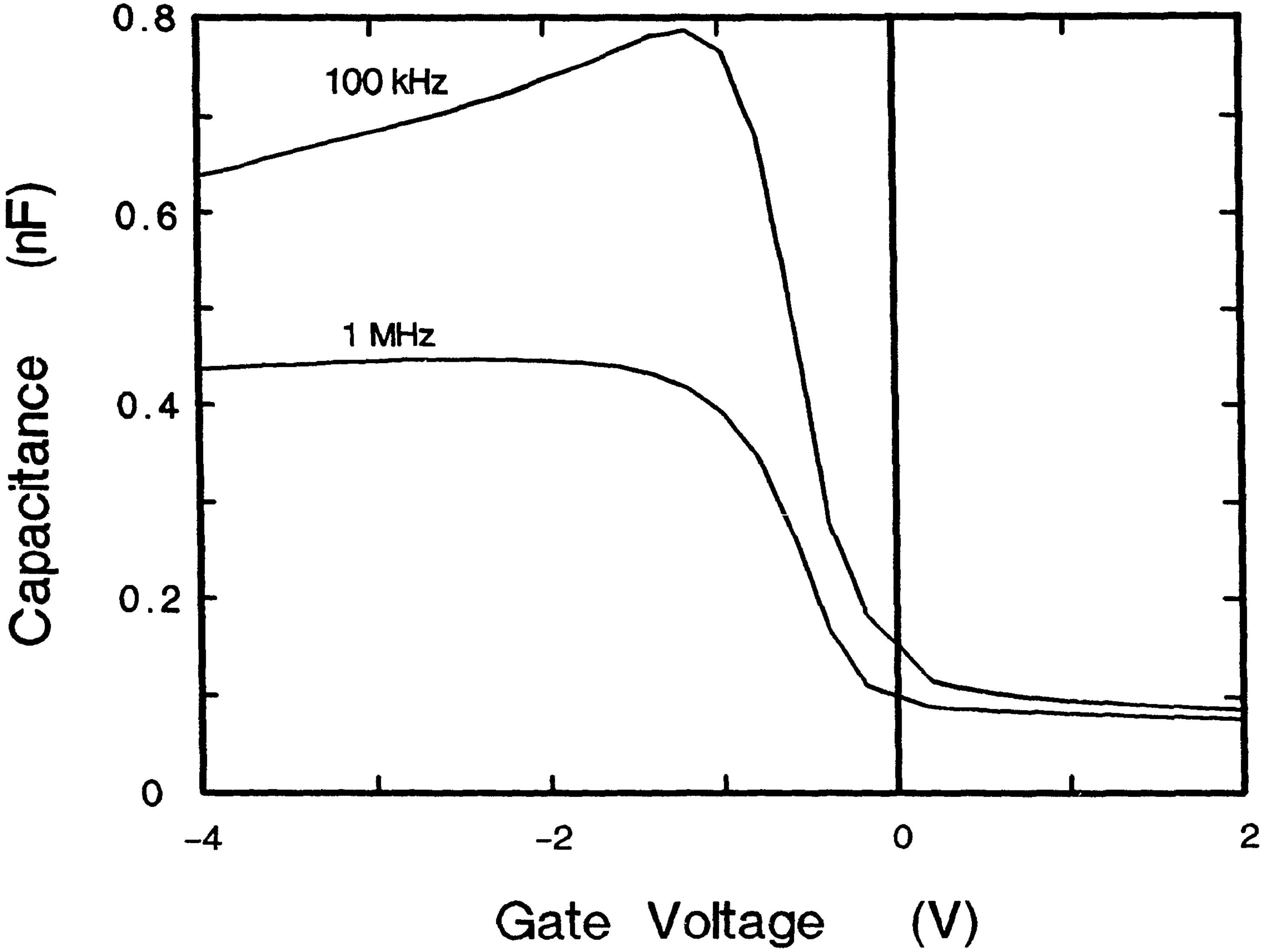

Fig. 4.15 The C-V characteristics of another Al-Y_2O_3-$CuInSe_2$ capacitor at 1 MHz and 100 kHz. The accumulation capacitance of the 1-MHz curve showed a better agreement with the theoretical value, 0.5 nF.

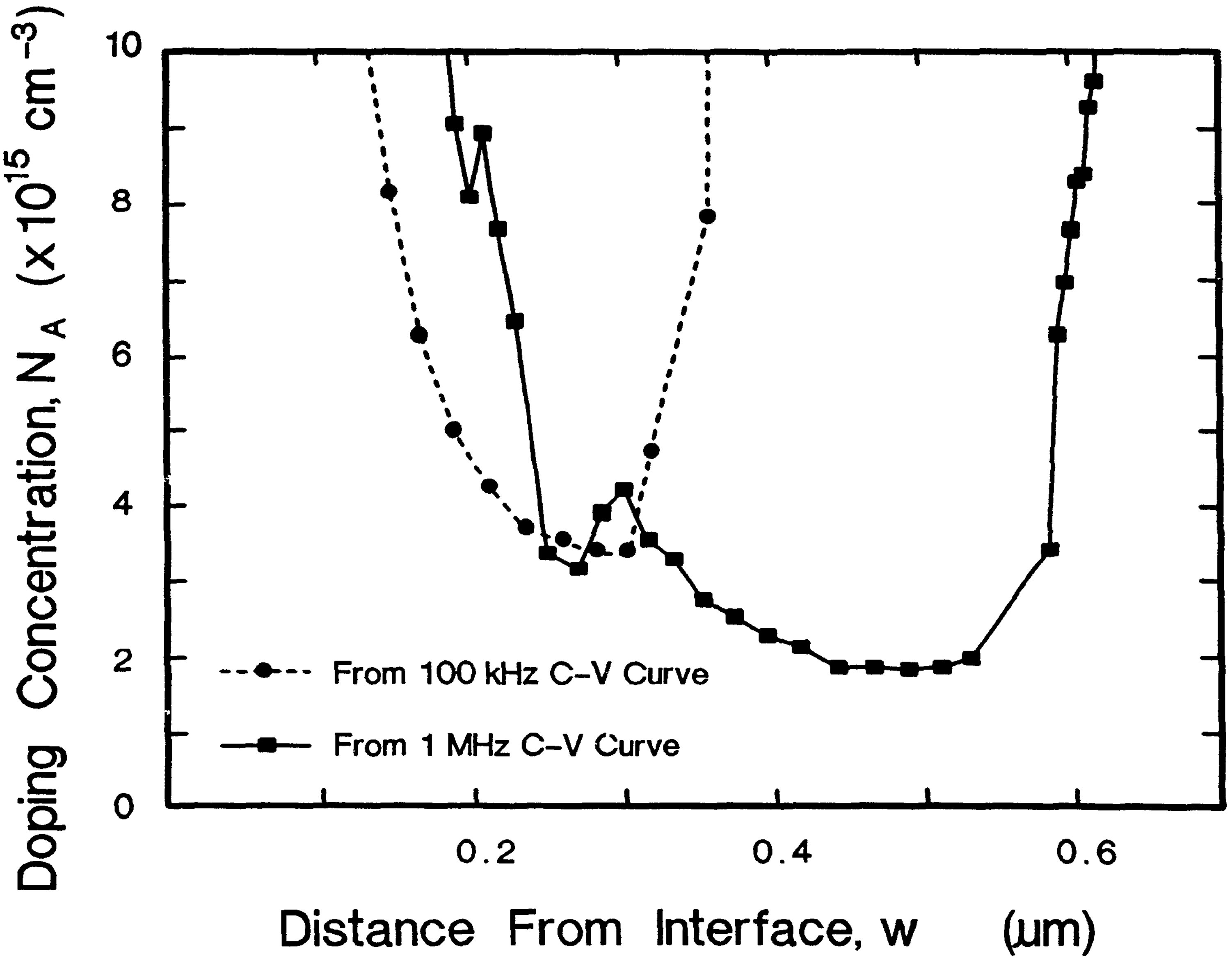

Fig. 4.16 Doping profile of the $CuInSe_2$ determined from the 1-MHz and 100-kHz curves shown in Fig. 4.15.

CHAPTER 5

CONCLUSIONS

Experiments on the preparation of bulk $CuInSe_2$ have been carried out in the present work. Using stoichiometric starting proportions, voids- and crack-free single crystals of $CuInSe_2$ with grain size as large as 50 mm^2 in area and 5 mm in thickness have been obtained. Difficulties were encountered in the early stage of the growth experiments. Particular serious problems were cracking or even explosion of the ampoules and presence of voids and cracks in the ingots. The cracking of ampoules was avoided by allowing the elements to react for a long time at about 200 ^oC, which is below the melting point of Se, and also employing a slow heating rate afterwards. An accelerated crucible rotation technique (ACRT) was found to be effective in mixing the melt and was particular helpful in avoiding bulk voids. Cracks in the ingots could also be minimized by using a slow cooling rate. The properties of the crystals were examined by several techniques. X-ray powder diffraction method showed that the crystals obtained had the stable chalcopyrite structure. Chemical etching experiments were also carried out with a mixture of H_2SO_4 and $K_2Cr_2O_7$ (9:1 by weight). Triangular etch-pits were revealed on a sample cut parallelly to the growth plane after chemical etching, indicating the possibility of an (112)-oriented growth plane. All as-grown samples were uniformly p-type. Room-temperature Hall-effect measurements were also performed to obtain the mobility, carrier concentration and resistivity. The highest mobility value obtained was about 73 cm^2/V-s. The chemical compositions of several samples were determined by electron probe microanalysis. A Cu/In ratio in the vicinity of 1 was obtained for the samples but a small deficiency of Se was observed due to a loss of Se during the growth. Compositional uniformity was observed for the as-grown sample across the growth plane.

Crystals grown from nonstoichiometric starting proportions have also been obtained. The conductivity type of the samples was dependent on the deviation from stoichiometry, although a clear relationship has not been found yet. The mobility of the n-type samples was comparatively lower than the values obtained by diffusion [2.17] possibly due to more defects in these samples grown from nonstoichiometric starting compositions. Results from electron probe microanalysis indicated that the nonstoichiometric samples generally had a higher concentration of Cu but a lower concentration of Se than the starting compositions, and the chemical compositions were uniform across the growth plane and along the growth direction except the last freeze-out regions.

Y_2O_3 films have also been deposited by rf planar magnetron sputtering. The dielectric constant of the Y_2O_3 films was about 12. MIS capacitors in the forms of Metal(Al)-Y_2O_3-Si (MYS) and metal(Al)-Y_2O_3-$CuInSe_2$ (MYC) were fabricated with sputtered Y_2O_3 films as the insulator. For the MYS capacitors, the dc leakage was small, and the resistivity was about 10^{13} Ω-cm, which is comparable to most of the commonly-used insulating films. The breakdown field of the Y_2O_3 films showed no clear correlation to the film thickness and this could be attributed to defects and impurities present in the films. The highest breakdown field obtained so far was about $3x10^6$ V/cm. The MYC capacitors exhibited large dc leakage which was resulted from premature breakdown of the Y_2O_3 films on the $CuInSe_2$ substrates. The premature breakdown of the Y_2O_3 films was believed to be caused by the roughness of the $CuInSe_2$ surface.

The C-V characteristics of the MYS and MYC capacitors were also measured. The accumulation capacitance of the C-V curves of the MYS capacitors exhibited a frequency dispersion, which can be attributed to the penumbra effect. The capacitances measured in depletion also showed a frequency dispersion, which was a parallel shift of the C-V curves along the voltage axis. This frequency dispersion was probably resulted from interface states with different time constants as reported by several workers. Most of the C-V curves obtained exhibited high-frequency characteristic except several curves measured at a frequency of 100 Hz, at which a transition between high- and low-frequency characteristics was observed. Measurements below this frequency were impossible using the present system because of the drastic effect of noise at such low frequencies. The doping profiles determined form these C-V curves were in good agreement with the actual values. The frequency dispersions did not seem to affect the accuracy by much although in some cases the "stretch-out" effect of the interface states caused a little bit higher doping concentrations to be obtained. Although the method used for the determination of doping profile involved no complex measurement technique and calculation, the results obtained were satisfactory. It is, therefore, feasible to determine the doping profile of Si in the MIS structure with sputtered Y_2O_3 films as the insulator. The results obtained from the MYC capacitors did not seem to be as good as the MYS capacitors mainly due to the large dc leakage of the MYC capacitors. The large leakage caused the C-V curves to have much larger values and skew in accumulation, to have a larger slope in depletion and to have larger values in inversion. These effects were more apparent at low frequencies and at high frequency (1 MHz) the C-V measurements approached the theoretical values. Therefore, the high-frequency C-V curves were used for the determination of the doping profile of the $CuInSe_2$. Unfortunately, the doping concentrations obtained were usually much smaller than the actual values due to steeper slopes of the C-V curves in depletion. It is apparent that the leakage current of the MYC capacitors should be reduced before accurate doping profile can be determined.

To summarize the thesis, possible further work is suggested here. For the crystal growth experiments, a lot of work can still be done on the preparation of bulk $CuInSe_2$ from nonstoichiometric starting compositions or with extrinsic doping. Investigation on how the deviations from stoichiometry of the crystals can affect or improve the performance of devices such as solar cells is definitely important for both academic and practical purposes. Work on the preparation of larger and higher-quality stoichiometric samples is, of course, also desirable for device fabrication and property-analysis. For the studies of MIS structure with sputtered Y_2O_3 films, more work can be done to improve further the quality of the films to reduce defects or increase the breakdown field. Care should also be taken to avoid the penumbra effect. Improved methods using quasi-static C-V measurement or pulsed C-V measurements should and will be used to obtain a larger accuracy and range for the doping profile. In order to study $CuInSe_2$ with the MIS structure, the most important work that should be done is the surface preparation of $CuInSe_2$. If a clean and smooth surface of $CuInSe_2$ can be prepared, high-quality metal-Y_2O_3-$CuInSe_2$ can then be fabricated. The thermal stability and annealing effect under different annealing conditions can then be studied by the C-V technique.

REFERENCES

[1.1] H. Hahn, G. Frank, W. Klinger, A. Meyer, and G. Storger, Z. Anorg. Allg. Chem. **271**, 153 (1953).

[1.2] R.A. Mickelsen, W.S. Chen, Y.R. Hsiao, and V.E. Lowe, IEEE Trans. Electron Dev. **31**, 542 (1984).

[1.3] J.L. Shay, S. Wagner, and H.M. Kasper, Appl. Phys. Lett. **27**, 89 (1975).

[1.4] R.R. Arya, T. Warminski, R. Beaulieu, M. Kwietniak, J.J Loferski, and W. Giriat, Sol. Energy Mater. **8**, 471 (1983).

[1.5] K. Mitchell, 4th Int. Photovolt. Sci. and Eng. Conf., Sydney, NSW Australia, Feb. 14-17, 1989.

[1.6] W. Horig, H. Neumann, H. Sobotta, B. Schumann, and G. Kuhn, Thin Solid Films **48**, 67 (1978).

[1.7] L.Y. Sun, L.L. Kazmerski, A.H. Clark, P.J. Ireland, and D.W. Morton, J. Vac. Sci. Technol. **15**, 265 (1978).

[1.8] L.L. Kazmerski, F.R. White, and G.K. Morgan, Appl. Phys. Lett. **29**, 268 (1976).

[1.9] R.A. Mickelsen and W.S. Chen, Appl. Phys. Lett. **36**, 371

(1980).

[1.10] C.X. Qiu and I. Shih, Can. J. Phys. **65**, 1011 (1987).

[1.11] Y. Hamakawa, Scientific American **257**, no. 4, 86 (1987).

[1.12] R.A. Mickelsen, W.S. Chen, B.J. Stanbery, H. Dursch, J.M. Stewart, Y.R. Hsiao, and W. Devaney, Proc. of 18th IEEE Photovoltaic Specialists Conf., 1069 (1985).

[1.13] R.D. Tomlinson, Solar Cells **16**, 17 (1986).

[1.14] E.H. Nicollian and J.R. Brews, MOS (Metal Oxide Semiconductor) Physics and Technology, Wiley, New York, 1982.

[1.15] T. Tsutsumi, Jpn. J. Appl. Phys. **9**, 745 (1970).

[1.16] L. Manchanda and M. Gurvitch, IEEE Trans. Electron Dev. Lett. **9**, 180 (1988).

[1.17] K.H. Zaininger and F.P. Heiman, Solid State Technol. **13**, no. 5,6, (1970).

[2.1] I. Shih, A. Vahid Shahidi, and Champness, J. Cryst. Growth **70**, 411 (1984).

[2.2] H. Haupt and K. Hess, Inst. Phys. Conf. Ser. **35**, 5 (1977).

[2.3] H. Sobotta, H. Neumann, W. Kissinger, G. Kuhn, and V. Riede, Phys. Status Solidi B **103**, K125 (1981).

[2.4] K.J. Bachmann, M. Fearheiley, Y.H. Shing, and N. Tran, Appl. Phys. Lett. **44**, 407 (1984).

[2.5] J.L. Shay, B. Tell, H.M. Kasper, and L.M. Schiavone, Phys. Rev. B **7**, 4485 (1973).

[2.6] I.G. Austin, C.H.L. Goodman, and A.E. Pengelly, J. Electrochem. Soc. **103**, 609 (1956).

[2.7] J. Parkes, R.D. Tomlinson, and M.J. Hampshire, J. Cryst. Growth **20**, 315 (1973).

[2.8] B. Tell and P.M. Bridenbaugh, J. Appl. Phys. **48**, 2477 (1977).

[2.9] T.F. Ciszek, J. Cryst. Growth **70**, 405 (1984).

[2.10] J.L. Hurd and T.F. Ciszek, J. Cryst. Growth **70**, 415 (1984).

[2.11] T.F. Ciszek, J. Electron. Mat. **14**, 451 (1985).

[2.12] A. Vahid Shahidi, I. Shih, and C.H. Champness, Canadian J. of Phys **63**, 811 (1985).

[2.13] Y.H. Shing, N.T. Tran, and K.J. Bachmann, Proc. 17th IEEE Photovolt. Spec. Conf. , 774 (1984).

[2.14] P.W. Yu, Y.S. Park, and J.T. Grant, Appl. Phys. Lett. **28**, 214 (1976).

[2.15] R.A. Laudise, The Growth of Single Crystal, p. 104, Prentice Hall, N.J., (1970).

[2.16] W.A. Tiller, K.A. Jackson, J.W. Rutter, and B. Chalmers, Acta Met. **1**, 428 (1953).

[2.17] A. Vahid Shahidi, "Preparation, Structure, Diffusion and Opto-electronic Studies of Crystalline $CuInSe_2$ for Solar Cell Applications", McGill Unversity Thesis (1984).

[2.18] H.J. Scheel and H. Muller-Krumbhaar, J. Cryst. Growth **49**, 291 (1980).

[2.19] K.D. Becker and S. Wagner, Phys. Rev. B **27**, 5240 (1983).

[2.20] H. Neumann, V.N. Nguyen, H.J. Hobler, and G. Kuhn, Solid State Communications **25**, 899 (1978).

[2.21] J. Parkes, R.D. Tomlinson, and M.J. Hampshire, Solid-State Electronics **16**, 773 (1973).

[2.22] T. Irie, S. Endo, and S. Kimura, Jpn. J. Appl. Phys. **18**, 1303 (1979).

[2.23] R.E. Rocheleau, J.D. Meakin, and R.W. Birkmire, Proc. 19th IEEE Photovolt. Spec. Conf., 972 (1987).

[3.1] B.E. Deal, A.S. Grove, E.H. Snow, and C.T. Sah, J. Electrochem. Soc. **112**, 308 (1965).

[3.2] C.W. Wilmsen, Thin Solid Films **39**, 105 (1976).

[3.3] S.K. Ghandi, VLSI Fabrication Principles, Wiley, New York, 1982.

[3.4] S. Suyama, A. Okamoto, and T. Serikawa, J. Electrochem. Soc. **134**, 2260 (1987).

[3.5] C.A.T. Salama, J. Electrochem. Soc. **117**, 913 (1970).

[3.6] S.M. Sze, Physics of Semiconductor Devices, p.852, Wiley, New York, 1981.

[3.7] H.F. Wolf, Silicon Semiconductor Data, p. 602, Pergamon Press, Oxford, 1969.

[3.8] S.M. Sze, J. Appl. Phys. **38**, 2951 (1967).

[3.9] L.G. Meiners, R.P. Pan, and J.R. Sites, J. Vac. Sci. Technol. **14**, 961 (1977).

[3.10] C.C. Cheng, T.W. Kim, V.D. Deokar, and W.W. Granneman, Bull. Am. Phys. Soc. Series II **18**, 555 (1973).

[3.11] J.F. Verwey and D.R. Wolters, Insulating Films on Semiconductors, ed. JJ. Simonne and J. Buxo, p. 125, North-Holland, Amsterdam, 1986.

[3.12] G.S. Oehrlein and A. Reisman, J. Appl. Phys. **54**, 6502 (1983).

[3.13] M.V. Yakushev, G. Constantinidis, M. Imanieh, and R.D. Tomlinson, Solid State Communications, **65**, 1079 (1988).

[4.1] J.R. Brews, J. Appl. Phys. **44**, 3228 (1973).

[4.2] J.M. Blacksin, IEEE Trans. Electron Dev. **33**, 1387 (1986).

[4.3] E.H. Snow, A.S. Grove, B.E. Deal, and C.T. Sah, J. Appl. Phys. **36**, 1664 (1965).

[4.4] L.M. Terman, Solid State Electron. **5**, 285 (1962).

[4.5] M. Kuhn, Solid State Electron. **13**, 873 (1970).

[4.6] W. van Gelder and E.H. Nicollian, J. Electrochem. Soc.

118, 138 (1971).

[4.7] E.H. Nicollian and J.R. Brews, MOS (Metal Oxide Semiconductor Physics and Technology, p. 384, Wiley, New York, 1982.

[4.8] E.H. Nicollian and J.R. Brews, MOS (Metal Oxide Semiconductor Physics and Technology, p. 222, Wiley, New York, 1982.

[4.9] K.H. Zaininger and G. Warfield, IEEE Trans. Electron Dev. **12**, 179 (1965).

[4.10] S. Seki, T. Unagami, and B. Tsujiyama, J. Electrochem. Soc. **131**, 2621 (1984).

[4.11] T.J. Mego, Rev. Sci. Instrum. **57**, 2798 (1986).

[4.12] S.T. Lin and J. Reuter, Solid State Electron. **26**, 343 (1983).